MULTIPHASIC MODEL DEVELOPMENT AND MESHLESS SIMULATIONS OF ELECTRIC-SENSITIVE HYDROGELS

CHEN JUN

(B. Eng., Huazhong University of Science and Technology, P. R. China)

A THESIS SUBMITTED

FOR THE DEGREE OF MASTER OF ENGINEERING

DEPARTMENT OF MECHANICAL ENGINEERING

NATIONAL UNIVERSITY OF SINGAPORE

2004

Acknowledgement

I would like to express my sincere thanks and appreciations to my supervisor, Prof. Lam Khin Yong, for his invaluable suggestions and guidance in my master research work.

I am deeply indebted to my co-supervisor, Dr. Li Hua, who helped me a lot in my master study of past two years and also provided me very important and useful advice and comments on this dissertation.

I extend my gratitude to the colleagues of our research group, Dr. Yuan Zhen, Dr. Wang Xiao Gui, Dr. Cheng Jin Quan, Mr. Yew Yong Kin, Mr. Wang Zi Jie and Mr. Luo Rong Mo. They gave me many precious suggestions in my research work and daily life.

Lastly, I would like to give my special thanks to my family for their love and supports.

Table of Contents

Summary

Based on the multiphasic mixture theories, a multiphysical mathematical model, called the multi-effect-coupling electric-stimulus (MECe) model, has been developed in this dissertation to simulate the responsive behaviors of electric-sensitive hydrogels when they are immersed into a bath solution subjected to an externally applied electric field. With consideration of chemo-electro-mechanical coupling effects, the MECe model consists of a set of nonlinear partial differential governing equations, including the Nernst-Plank equations for the diffusive ionic species, Poisson equation for the electric potential and continuum equations for the mechanical deformations of hydrogels. In order to solve the complicated MECe model, a novel meshless technique, termed Hermite-Cloud method, is employed in the present numerical simulations. The developed MECe model is examined by comparisons of numerically computed results with experimental data extracted from open literature, in which very good agreements are achieved. Then one-dimensional steady-state and transient simulations are carried out for analyses of equilibrium and kinetics of the electric-stimulus responsive hydrogels, respectively. Simulations are also conducted for the distributions of ionic concentrations, electric potential and hydrogel displacement. The influences of key physical parameters on the responsive behaviors of electric-sensitive hydrogels are discussed in details, including the externally applied electric field, fixed-charge density and bath

solution concentration. According to the present studies and discussions, several significant conclusions are drawn and they provide useful information for researchers and designers in the bio-micro-electro-mechanical systems (BioMEMS) field.

Nomenclature

A cross section area

$\boldsymbol{B}_w$ coupling coefficient

c^f fixed-charge density

c_0^f fixed-charge density at reference configuration

c^k concentration of ion k

c^* initial ion concentration of bath solution

D_k diffusive coefficient of ion k

E elasticity modulus

$\boldsymbol{E}$ elastic strain vector of the solid phase

$\mathbf{f}^\alpha$ body force per unit mass of phase α

$f_{\alpha\beta}$ diffusive drag coefficient between α and β phases

F Helmholtz energy function

$\mathscr{F}^\alpha$ density of Helmholtz energy of phase α

$\boldsymbol{F}^s$ deformation gradient tensor

F_c Faraday constant

G shear modulus

I inertia moment

k_s shear correction coefficient

K kinetic energy

M^k molar weight of ion k

p pressure

q^{α} heat flux vector of phase α

Q heat transferring into the system

R universal gas constant

S entropy

$\boldsymbol{t}^{\alpha}$ drag force applied on the surface of phase α

T absolute temperature

T_C chemical-expansion stress

U internal energy

$\boldsymbol{v}^{\alpha}$ velocity of phase α

$\mathbf{v}$ external normal on the surface

V mixture volume

V_0 mixture volume at reference configuration

V_e externally applied voltage

V^{α} true volume of phase α

w deflection

W total work

W_e work done by external force

W_p work done by pressure

z^f valence of fixed-charge groups

z^k valance of ion k

θ rotation

γ^{α} rate of heat generation per unit mass of phase α

γ_k activity coefficient of ion k

ε dielectric constant

ε_0 permittivity of free space

η^{α} entropy per unit mass of phase α

λ_s , μ_s Lame coefficients of solid matrix

μ_0^{α} chemical potentials of phase α at reference configuration

μ^{α} chemical potential of phase α

ϕ_0^s volume fraction of solid phase at reference configuration

ϕ_0^w volume fraction of water phase at reference configuration

ϕ^{α} volume fraction of phase α

Φ^k osmotic coefficient of ion k

Π^{α} diffusive momentum exchange among different phases

ρ^{α} apparent mass density of phase α

ρ_T^{α} true mass density of phase α

$\boldsymbol{\sigma}^{\alpha}$ stress tensor of phase α

$\boldsymbol{\sigma}$ total stress tensor of hydrogel mixture

σ_E^s Cauchy stress tensor

τ_E^s Piola-Kirchhoff stress tensor

ψ electric potential

List of Figures

List of Tables

Chapter 1

Introduction

In this chapter, a concise introduction is given for the dissertation. The definition of hydrogels and their application for this research area are presented. Then the working objective and scope and a literature survey are described. Lastly, the layout of the dissertation is provided.

1.1 Background

Hydrogels are defined as the three-dimensional hydrophilic polymer-based network that is capable of assimilating abundant interstitial water or biological fluid. Generally, the cross-linked polymer chains attach some positive or negative charged groups, which are called fixed-charges because their mobility is much less than that of the freely mobile ions in the interstitial water. Therefore, as shown in Figure 1.1 for the microscopic structure of the charged hydrogel, the hydrogels are the multiphasic mixture, consisting of solid phase (polymeric-network matrix with fixed-charges), water phase (interstitial fluid) and ion phase (mobile ionic species).

As well known, there is a large variety of hydrogels, depending on the preparations. Some of them are able to be sensitive to different environmental stimuli, including the electric field (Tanaka et al., 1982; Kwon et al., 1991; Osada

et al., 1992), pH (Tanaka, 1978, 1980; Siegel, 1988), temperature (Chen and Hoffman, 1995; Yoshida, 1995), and chemicals (Kokufuta et al., 1991; Kataoka et al., 1998). They make fast changes from a hydrophilic state to a hydrophobic one with the small variation of environment, and usually the volume changes of hydrogels are also reversible when the external stimuli disappear. With good biostability and biocompatibility, high ionic conductivity and sensitivity similar to biopolymers, hydrogels have considerable promise in biological and medicine applications (Jeong and Gutowska, 2002; Galaev and Mattiasson 1999), such as artificial muscle, drug delivery and biomimetic actuators/sensors in BioMEMS (Beebe et al., 2000).

1.2 Objective and scope

It is noted that although big progresses have been made in the study of hydrogels, most studies done are experimental-based. Few theoretical analyses and numerically modeling work on the responsive mechanism of hydrogels were done in the past decades due to their complicated multiphasic structures. As such, the main objective of this dissertation is to formulate a mathematical model to provide more accurate simulations of the responsive behaviors of hydrogels, including the mechanical deformation and the distributions of diffusive ions and electric potential.

As mentioned above, since the hydrogels can be responsive to many environmental triggers, it is difficult to develop a single theoretical model to

include all these external stimuli. As a result, this dissertation focuses on the stimulus of electric field only. Based on the classical multiphasic mixture theory (Lai et al., 1991), a novel mathematical model, termed multi-effect-coupling electric-stimulus (MECe) model (Li et al., 2004), is developed to simulate the equilibrium and kinetic responsive behaviors of electric-sensitive hydrogels immersed into a bath solution under an externally applied electric field.

With consideration of chemo-electro-mechanical coupling effects and the multiphasic interactions between the interstitial fluid, ionic species and polymeric matrix, the developed MECe model is a set of nonlinear coupling partial differential governing equations, consisting of the Nernst-Plank equations to describe the diffusive ionic species, Poisson equation for the electric potential and the continuum equations for the mechanical deformation of hydrogel mixture. In addition, for development of the MECe model, several assumptions are made as follows,

- the fixed-charge groups remain unchanged;
- incompressibility for all three phases;
- infinitesimal deformation;
- material isotropy;
- ideal bath solution.

There are two main contributions of the dissertation. One contribution is the formulation of the MECe model. The other one is the employment of a novel meshless technique, called Hermite-Cloud method (HCM), in the numerical

simulations.

Compared with previous published work, the present MECe model holds several advantages: (a) the computational domain of the MECe model covers both the hydrogels and surrounding solution, and the model is able to provide the full responses of geometric deformation and distributions of ionic concentrations and electric potential in both the domains; (b) the model can directly simulate the responsive distributions of electric potential, instead of the use of electro-neutrality condition; and (c) the MECe model presents an explicit expression for the hydrogel transient displacement.

In this dissertation, the Hermite-Cloud method (HCM) (Li et al., 2003), a recently developed meshless technique, is used for all simulations to solve the complicated coupled nonlinear partial differential equations of the MECe model. In comparison with other classical reproducing kernel particle methods (RKPM), the HCM constructs the approximate solutions of both the unknown functions and their first-order derivatives. Thus the HCM gives a high computational accuracy not only for the approximate solutions, but for their first-order derivatives. It is very useful for the numerical simulations of the MECe model since the first-order derivatives of the main physical variables here, such as the ion concentrations, electrical potential and hydrogel displacement, have significant influence on the computational accuracy due to the localized high gradient of distributions of ionic concentrations and electric potential.

1.3 Literature survey

In order to understand deeply the electric-responsive hydrogels and the relevant research work, it is necessary to do a literature survey on this research area and give a brief review on previous modeling work.

Over the past decades, numerous efforts were made to develop the model for simulations of the responsive behaviors of hydrogels and hydrogel-like biological tissues with the effect of external stimuli. The early work includes the biphasic model for articular cartilage by Mow and co-workers (1980), in which the tissue is defined as a mixture of two phases based on the mixture theory, i.e. a solid phase for the charged polymeric matrix and a fluid phase for the interstitial fluid. In their work, several experimental parameters were obtained and used to simulate numerically the material properties of the tissues.

However, it should be noted that the charged nature of hydrogel-like tissues was not considered in the biphasic theory, which took into account the mechanical property only. Thus it is difficult for the biphasic model to simulate the physiochemical and electrochemical phenomena in the tissues, such as the diffusive ions, chemical expansion of solid matrix and the fixed-charge effect on ion distributions. In order to incorporate such behaviors in the models, several constitutive models were developed. They include the swelling thermo-analog theory by Myers et al. (1984), the bicomponent theory by Lanir (1987) and the electromechanical theory by Eisenberg and Grodzinsky (1987). Although physiochemical and electrochemical effects were considered in these theories to

some extent, some important variables, such as the fixed-charge density and diffusive ionic concentrations, were not expressed explicitly in the constitutive equations.

To overcome the drawbacks mentioned above, Lai et al. (1991) proposed a triphasic mechano-electrochemical theory for the responsive behavior of hydrogel-like tissues. In comparison with the biphasic theory, an additional ionic phase was included in the triphasic theory besides the solid and fluid phases. As a result, the triphasic model employs the continuum theory for the mixture of solid and fluid phases, and the physico-chemical theory deriving from the laws of thermodynamics for the ionic phase. By introducing the chemical potential, whose gradients were the driving force for the movement of fluid and ions, Lai and his co-workers built theoretically a bridge between physico-chemical and continuum mixture theories. It represented a significant progression in the modeling development for the hydrogel and hydrogel-like tissues.

Many other investigators also made their contributions in the theoretical development. Siegel (1990) and Chu et al. (1995) tried to use the thermodynamic models to describe the equilibrium deformation of hydrogels, in which it was hard to obtain accurately some parameters required as the input of models due to special assumptions made in the models. Based on the classical Flory's theory and Donnan assumption, Doi et al. (1992) developed a semiquntitative model to investigate the deformation of hydrogels subject to an applied electric field. However, this model was incomplete because the motions of water and hydrogel

were not considered. In addition, Grimshaw et al. (1990) and Shahinpoor (1994, 1995) employed a macroscopic theory to explain the dynamic response of hydrogels with chemical/electrical triggers.

Recently, more attentions were paid on the analysis of hydrogels by theories and these modeling works include: an extension of Lai's triphasic model done by Gu et al. (1998, 1999) and the numerical models developed by Wallmersperger et al. (2001) and Zhou et al. (2002), respectively. In Gu's mixture model, the hydrogel-like tissues are placed in the multi-electrolyte solution so that the mixture is composed of (n+2) constituents. Compared with triphasic model in which the simple 1:1 salt solution is considered only, the new mixture model is more complete and takes into account the effect of other quantitatively minor ions on the responsive behaviors of tissues. Moreover, Wallmersperger et al. (2001) and Zhou et al. (2002) proposed their models respectively to simulate the deformation of hydrogels under the external electric field, and they achieved good agreement between the experimental data and simulation results.

However, it is found that most works are based on experiments in the study of responsive hydrogels. They have significant influences on the theoretical development, in which most notable experiments include the work done by Kim and Shin (1999), Homma et al. (2000, 2001), Sun et al. (2001), Wallmersperger et al. (2001) and Fei et al. (2002) for the swelling, shrinking and bending behaviors of the hydrogels under externally applied electric field.

Despite the progress achieved in the modeling development of the hydrogels,

they still have limited applications. For example, the Gu's model is unable to simulate the effect of external electric field. It is difficult to do transient analysis of hydrogel deformation by Wallmerperger's model. In Zhou's model, the computational domain covers the hydrogel only. Therefore, it is evidently necessary to develop a more robust mathematical model for better understanding of the response mechanism of hydrogels to the external stimuli. By developing the present MECe model, this dissertation simulates the responsive behaviors of the hydrogels with the chemo-electro-mechanical coupling effect when the hydrogels are immersed into a bath solution under an externally applied electric field.

1.4 Layout of dissertation

This dissertation is divided into six chapters, and each of them consists of several subsections respectively to make the dissertation more systematic.

Chapter 1, Introduction, is divided into four sections. The first section, Background, gives a concise definition of hydrogels and their wide range applications in the biotechnology and bioengineering. The second section, Objective and scope, describes the purpose of this dissertation and its application scope. The third section, Literature survey, presents a complete review on the publication in the hydrogels area. The forth section, Layout of dissertation, describes the layout of this dissertation.

Chapter 2, Development of Multi-Effect-Coupling Electric-Stimulus (MECe) Model for Electric-Sensitive Hydrogels, is divided into four sections. In

the first section, a brief survey on the existing mathematical models for the hydrogels is given. In the second section, the governing equations of the developed MECe model are formulated in detail. The third section summarizes the boundary and initial conditions applied in the governing equations. In the fourth section, the non-dimensional implementation is introduced.

Chapter 3, Meshless Hermite-Cloud Numerical Method, is divided into three sections. The first section gives a short review for the meshless methods. The second section presents the full development of the Hermite-Cloud method, including the theoretical formulation, computational implementation as well as numerical validations. The third section applies Hermite-Cloud method for the nonlinear fluid-structure analysis of submarine pipelines.

Chapter 4, One-Dimensional Steady-State Simulations for Equilibrium of Electric-Sensitive Hydrogels, is divided into four sections. In the first section, the studied problem, a hydrogel strip immersed into a bath solution subject to an applied electric field, is described. In the second section, the discretization of reduced 1-D governing equations for the steady-state analysis is conducted. In the third section, a comparison is made between the simulated results and experimental data. In the fourth section, the influences of several parameters are studied on the responsive behaviors of the hydrogels, including the external electric field, fixed-charge density, concentrations of bath solution and ionic valences.

Chapter 5, One-dimensional Transient Simulations for Kinetics of

Electric-Sensitive Hydrogels, is divided into three sections. The first section proposes the discretization of reduced 1-D governing equations for the transient simulations. The second section gives an experimental comparison to validate numerically the model. The third section presents the transient studies on distributions of several important parameters, i.e. ionic concentrations, electric potential, hydrogel displacement and average curvature.

Chapter 6, Conclusions and Future Works, is divided into two sections. In the first section, conclusions are drawn based on the present simulations and discussions. In the second section, several further research topics are recommended for the future.

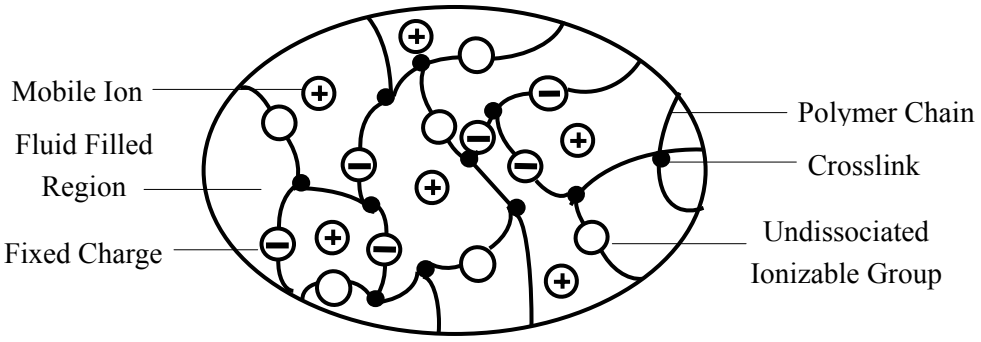

Figure 1.1 Microscopic structure of the charged hydrogel.

Chapter 2

Development of Multi-Effect-Coupling Electric-Stimulus (MECe) Model for Electric-Sensitive Hydrogels

In this chapter, two previously developed mathematical models are summarized for the responsive hydrogels. This is followed by full development of the present MECe model, in which four main governing equations are formulated to describe the ion concentrations, electric potential, fluid pressure and hydrogel deformation. Then the boundary and initial conditions for the governing equations are proposed and the non-dimensional implementation for the governing equations is also carried out.

2.1 Survey of existing mathematical models

As is well known, when a hydrogel is immersed a bath solution with an externally applied electric field, the fixed-charge attached on the polymer chains attracts the electro-opposite ions from the surrounding solution to maintain the electro-neutrality. Meanwhile, the external electric field also drives the ions diffusing to electro-opposite electrodes. These two effects result in the difference of ion concentrations between the hydrogel and surrounding solution and induce the fluid pressure. As the main driving force, the fluid pressure makes the

hydrogel deform, and the deformation of the hydrogel will cause the redistribution of the fixed-charge groups. Then the mobile ions in the solution will diffuse and redistribute again due to the change of fixed-charges and a new cycle of the above process will follow until the hydrogel mixture reaches equilibrium.

For simulation of the responsive behaviors of hydrogels under an applied electric field, several mathematical models have been developed recently, as mentioned in the literature survey of Chapter 1. Two of them are selected here to provide the basis for developing the present MECe model.

The first model is called the triphasic model given by Hon and his co-workers (1999, 2002). Based on the triphasic mixture theory of Lai et al. (1991), Hon develops a set of governing equations from the generalized law of thermodynamics for an irreversible thermodynamical system, in which several disadvantages are found. For example, the computational domain of this model is limited in the interior hydrogel, excluding the external bath solution, since the governing equations are totally obtained from the classical thermodynamics, whose scope mainly focuses on the mixture. Thus it can not provide the complete distribution of ionic concentrations. In addition, the electro-neutrality condition is required and the electric potential is not a variable in the governing equation, therefore the distribution of electric potential along the whole solution can not be simulated.

The second model is the multi-field formulation proposed by Wallmersperger and his co-workers (2001). In this formulation, the convection-diffusion equations,

Poisson equation and motion equation are adopted to describe the chemical field, electric field as well as mechanical field respectively. Although the computations of chemical and electric field are carried out in the full domain covering the hydrogel and surrounding solution, it should be noted that the motion equation for the mechanical field is just a general expression of Newton's second law and far from the truly complicated mechanical behavior of hydrogels.

2.2 Formulation of MECe governing equations

In order to overcome the limits of the above models, a novel mathematical model, called Multi-Effect-Coupling Electric-Stimulus (MECe) model is developed in this dissertation, based on the work done by Hon et al. (1999). Compared with the triphasic model, the MECe model provides a computational domain covering both the hydrogel and surrounding solution. The electric potential is also considered in the governing equations. Over the multi-field formulation, the MECe model includes a more accurate expression of the mechanical deformation of hydrogels. In addition, the displacement of hydrogel in the present MECe model is expressed explicitly in the governing equations, so that it is very convenient for transient simulations. As such, the developed MECe model is a fully multiphasic and mathematically precise formulation, which can give more reliable simulated results.

In the MECe model, the mixture is assumed to consist of the solid phase denoted by superscript s, interstitial water phase by w and ion phase by k

($k = 1,2,\cdots n_f$, here n_f is the total number of mobile species). Let ϕ^α ($\alpha = s, w, k$) represent the volume fraction of the phase α and it is defined as

$$\phi^\alpha = \frac{dV^\alpha}{dV} \quad (\alpha = s, w, k) \tag{2.1}$$

where V^α is the true volume of the phase α, V is the mixture volume. Then the saturation condition of the mixture can be expressed

$$\sum_{\alpha=s,w,k} \phi^\alpha = 1 \tag{2.2}$$

When infinitesimal deformation of the mixture is considered, the apparent volume ratio of the solid phase is given by

$$J = \frac{dV_0}{dV} = \frac{1}{1+tr(\boldsymbol{E})} \tag{2.3}$$

in which V_0 is the mixture volume at reference configuration, and $\boldsymbol{E}$ the elastic strain vector of the solid phase. The volume fraction of the solid phase is thus written as

$$\phi^s = \frac{dV^s}{dV} = \frac{dV^s}{dV_0} \cdot \frac{dV_0}{dV} = \phi_0^s J = \frac{\phi_0^s}{(1+tr(\boldsymbol{E}))} \tag{2.4}$$

where ϕ_0^s is the volume fraction of the solid phase at reference configuration. Due to the very small volume of the ion phase, ϕ^k is reasonably assumed zero in comparison with ϕ^s and ϕ^w. Therefore one has the expression of the volume fraction of the water phase as

$$\phi^w = 1 - \phi^s = 1 - \frac{\phi_0^s}{(1+tr(\boldsymbol{E}))} \tag{2.5}$$

If chemical reactions are neglected, each phase must follow the law of mass conservation as

$$\frac{\partial \rho^{\alpha}}{\partial t} + \nabla \cdot (\rho^{\alpha} \boldsymbol{v}^{\alpha}) = 0 \qquad (\alpha = s, w, k) \tag{2.6}$$

where $\boldsymbol{v}^{\alpha}$ (α = s, w, k) is the velocity of the phase α, and ρ^{α} (α = s, w, k) the apparent mass density of the phase α. It is noted that the apparent mass density ρ^{α} can be expressed by its respective true mass density ρ_T^{α}, i.e. $\rho^{\alpha} = \rho_T^{\alpha} \phi^{\alpha}$ (α = s, w, k). Meanwhile, on the basis of incompressibility restriction, ρ_T^{α} is reasonably assumed to be constant, and then Equation (2.6) is rewritten as

$$\frac{\partial \phi^{\alpha}}{\partial t} + \nabla \cdot (\phi^{\alpha} \boldsymbol{v}^{\alpha}) = 0 \qquad (\alpha = s, w, k) \tag{2.7}$$

By combining Equations (2.2) and (2.7), the continuity condition for the mixture is given as

$$\nabla \cdot (\sum_{\alpha=s,w,k} \phi^{\alpha} \boldsymbol{v}^{\alpha}) = 0 \tag{2.8}$$

By the tensor analysis, one has

$$\nabla \cdot (\phi^{\alpha} \boldsymbol{v}^{\alpha}) = \phi^{\alpha} \nabla \cdot \boldsymbol{v}^{\alpha} + \boldsymbol{v}^{\alpha} \cdot \nabla \phi^{\alpha} = \phi^{\alpha} \mathbf{I} : \nabla \boldsymbol{v}^{\alpha} + \boldsymbol{v}^{\alpha} \cdot \nabla \phi^{\alpha} \tag{2.9}$$

Thus Equation (2.8) is rewritten as

$$\sum_{\alpha=s,w,k} (\phi^{\alpha} \mathbf{I} : \nabla \boldsymbol{v}^{\alpha} + \boldsymbol{v}^{\alpha} \cdot \nabla \phi^{\alpha}) = 0 \tag{2.10}$$

The rate of kinetic energy $\dot{K}$ of the mixture is given by

$$\dot{K} = \sum_{\alpha=s,w,k} \dot{K}^{\alpha} = \int_V (\sum_{\alpha=s,w,k} \boldsymbol{v}^{\alpha} \cdot \dot{\boldsymbol{v}}^{\alpha} \rho^{\alpha}) dV \tag{2.11}$$

The internal energy of the mixture, U, can be expressed by the Helmholtz energy function F as

$$U = F + TS \tag{2.12}$$

The rate of internal energy $\dot{U}$ is obtained as

$$\dot{U} = \dot{F} + (\dot{T}S + T\dot{S}) = \int_V \sum_{\alpha=s,w,k} (\dot{\mathcal{F}}^{\alpha} + \dot{T}\eta^{\alpha} + T\dot{\eta}^{\alpha}) \rho^{\alpha} dV \tag{2.13}$$

where T is the absolute temperature, S the entropy of the system, $\mathscr{F}^{\alpha}$ and η^{α} are the density of Helmholtz energy and entropy per unit mass of the phase α respectively.

It is noted that both the internal energy U and Helmholtz energy F are state functions depending on their state variables, which include the following parameters of the multiphasic mixture, the thermal parameter T for the absolute temperature, the mechanical parameter $\boldsymbol{E}$ for the elastic strain tensor, the chemical parameters ρ^{α} for the apparent densities and the electrochemical parameter c^{f} for the fixed-charge density. With such constitutive consideration, the Helmholtz energy density is expressed by

$$\mathscr{F}^{\alpha} = \mathscr{F}^{\alpha}(T, \boldsymbol{E}, \rho^{s}, \rho^{w}, \rho^{k}, c^{f}) \qquad (\alpha = s, w, k) \tag{2.14}$$

Thus the rate of Helmholtz energy density is derived as

$$\dot{\mathscr{F}}^{\alpha} = \frac{\partial \mathscr{F}^{\alpha}}{\partial T}\dot{T} + \frac{\partial \mathscr{F}^{\alpha}}{\partial \boldsymbol{E}}\dot{\boldsymbol{E}} + \sum_{\beta=s,w,k}\frac{\partial \mathscr{F}^{\alpha}}{\partial \rho^{\beta}}\dot{\rho}^{\beta} + \frac{\partial \mathscr{F}^{\alpha}}{\partial c^{f}}\dot{c}^{f} \quad (\alpha = s, w, k) \tag{2.15}$$

From Equation (2.9) one can know

$$\dot{\rho}^{\beta} \equiv \frac{D\rho^{\beta}}{Dt} = -\rho^{\beta}\mathbf{I} : \nabla \boldsymbol{v}^{\beta} \tag{2.16}$$

and with the fact that $\dot{J} = -J\nabla \cdot \boldsymbol{v}^{s}$, we have

$$\dot{c}^{f} = -c_0^{f} J\mathbf{I} : \nabla \boldsymbol{v}^{s} \tag{2.17}$$

Noting the relation $\dot{\boldsymbol{E}} = (\boldsymbol{F}^{s})^{T} \cdot \nabla \boldsymbol{v}^{s} \cdot \boldsymbol{F}^{s}$, one can get

$$\frac{\partial \mathscr{F}^{\alpha}}{\partial \boldsymbol{E}} : \dot{\boldsymbol{E}} = \frac{\partial \mathscr{F}^{\alpha}}{\partial \boldsymbol{E}} : ((\boldsymbol{F}^{s})^{T} \cdot \nabla \boldsymbol{v}^{s} \cdot \boldsymbol{F}^{s}) = (\boldsymbol{F}^{s} \cdot \frac{\partial \mathscr{F}^{\alpha}}{\partial \boldsymbol{E}} \cdot (\boldsymbol{F}^{s})^{T}) : \nabla \boldsymbol{v}^{s} \tag{2.18}$$

where $\boldsymbol{F}^{s}$ and $(\boldsymbol{F}^{s})^{T}$ are the deformation gradient tensor and its transpose, respectively.

With substitution of Equations (2.16)-(2.18) into Equation (2.15), we obtain

$$\dot{\mathscr{F}}^{\alpha}=\frac{\partial \mathscr{F}^{\alpha}}{\partial T}\dot{T}+(\boldsymbol{F}^{s}\cdot\frac{\partial \mathscr{F}^{\alpha}}{\partial \boldsymbol{E}}\cdot(\boldsymbol{F}^{s})^{T}-c_{0}^{f}J\frac{\partial \mathscr{F}^{\alpha}}{\partial c^{f}}\mathbf{I}):\nabla \boldsymbol{v}^{s}-\sum_{\beta=s,w,k}\rho^{\beta}\frac{\partial \mathscr{F}^{\alpha}}{\partial \rho^{\beta}}\mathbf{I}:\nabla \boldsymbol{v}^{\beta} \quad (2.19)$$

Substituting Equation (2.19) into (2.13), we have

$$\begin{aligned}\dot{U}=\int_{V}\sum_{\alpha=s,w,k}(&\frac{\partial \mathscr{F}^{\alpha}}{\partial T}\dot{T}+(\boldsymbol{F}^{s}\cdot\frac{\partial \mathscr{F}^{\alpha}}{\partial \boldsymbol{E}}\cdot(\boldsymbol{F}^{s})^{T}-c_{0}^{f}J\frac{\partial \mathscr{F}^{\alpha}}{\partial c^{f}}\mathbf{I}):\nabla \boldsymbol{v}^{s}-\\&-\sum_{\beta=s,w,k}\rho^{\beta}\frac{\partial \mathscr{F}^{\alpha}}{\partial \rho^{\beta}}\mathbf{I}:\nabla \boldsymbol{v}^{\beta}+\dot{T}\eta^{\alpha}+T\dot{\eta}^{\alpha})\rho^{\alpha}dV\end{aligned} \quad (2.20)$$

The total rate of work $\dot{W}$ consists of two parts, the rate of work done by external forces $\dot{W}_{e}$ and rate of work done by pressure $\dot{W}_{p}$, i.e.

$$\dot{W}=\dot{W}_{e}+\dot{W}_{p} \quad (2.21)$$

The rate of work done by external forces $\dot{W}_{e}$ is defined as

$$\dot{W}_{e}=\sum_{\alpha=s,w,k}(\int_{V}\rho^{\alpha}\mathbf{f}^{\alpha}\cdot\boldsymbol{v}^{\alpha}dV+\int_{S}\boldsymbol{t}^{\alpha}\cdot\boldsymbol{v}^{\alpha}dS) \quad (2.22)$$

where $\mathbf{f}^{\alpha}$ is the body force per unit mass of the phase α, $\boldsymbol{t}^{\alpha}=\boldsymbol{\sigma}^{\alpha}\cdot\mathbf{v}$ is the drag force applied on the surface, $\boldsymbol{\sigma}^{\alpha}$ the stress tensor of the phase α and $\mathbf{v}$ the external normal on the surface. Based on the symmetry of stress tensor and Gaussian gradient formula, we have the following transformation

$$\int_{S}\boldsymbol{t}^{\alpha}\cdot\boldsymbol{v}^{\alpha}dS=\int_{S}(\boldsymbol{\sigma}^{\alpha}\cdot\boldsymbol{v}^{\alpha})\cdot\mathbf{v}dS=\int_{V}\nabla\cdot(\boldsymbol{\sigma}^{\alpha}\cdot\boldsymbol{v}^{\alpha})dV=\int_{V}((\nabla\cdot\boldsymbol{\sigma}^{\alpha})\cdot\boldsymbol{v}^{\alpha}+\boldsymbol{\sigma}^{\alpha}:\nabla\boldsymbol{v}^{\alpha})dV \quad (2.23)$$

Thus Equation (2.22) can be rewritten as

$$\dot{W}_{e}=\sum_{\alpha=s,w,k}\int_{V}((\rho^{\alpha}\mathbf{f}^{\alpha}+\nabla\cdot\boldsymbol{\sigma}^{\alpha})\cdot\boldsymbol{v}^{\alpha}+\boldsymbol{\sigma}^{\alpha}:\nabla\boldsymbol{v}^{\alpha})dV \quad (2.24)$$

The rate of work done by pressure $\dot{W}_{p}$ is defined as

$$\dot{W}_{p}=-p\dot{V} \quad (2.25)$$

Considering that, in the incompressible case $\dot{V}=0$, the continuity equation (2.10) is adopted, one can get

$$\dot{W}_p = \int_V -p \sum_{\alpha=s,w,k} (\phi^\alpha \mathbf{I} : \nabla \boldsymbol{v}^\alpha + \boldsymbol{v}^\alpha \cdot \nabla \phi^\alpha) dV \tag{2.26}$$

Substituting Equations (2.24) and (2.26) into (2.21), we obtain

$$\dot{W} = \sum_{\alpha=s,w,k} \int_V ((\rho^\alpha \mathbf{f}^\alpha + \nabla \cdot \boldsymbol{\sigma}^\alpha - p \nabla \phi^\alpha) \cdot \boldsymbol{v}^\alpha + (\boldsymbol{\sigma}^\alpha - p\phi^\alpha \mathbf{I}) : \nabla \boldsymbol{v}^\alpha) dV \tag{2.27}$$

The rate of heat transferred into the mixture is defined as

$$\dot{Q} = \sum_{\alpha=s,w,k} (\int_V \rho^\alpha \gamma^\alpha dV - \int_S \boldsymbol{q}^\alpha \cdot \mathbf{v} dS) \tag{2.28}$$

where γ^α is the rate of heat generation per unit mass of phase α, and $\boldsymbol{q}^\alpha$ the heat flux vector. Similarly, with the Gaussian gradient formula we have

$$\dot{Q} = -\sum_{\alpha=s,w,k} \int_V (\nabla \cdot \boldsymbol{q}^\alpha - \rho^\alpha \gamma^\alpha) dV \tag{2.29}$$

The rate of energy dissipation $\dot{D}$ is defined as

$$\dot{D} = \sum_{\alpha=s,w,k} \int_V \Pi^\alpha \cdot \boldsymbol{v}^\alpha dV \tag{2.30}$$

In the above Equation (2.30), Π^α is the diffusive momentum exchange among different phases, and it is a physical parameter indicating the diffusive resistance to the relative flow between two phases. Π^α can be expressed by their relative velocities as

$$\Pi^\alpha = \sum_{\beta=s,w,k} f_{\alpha\beta} (\boldsymbol{v}^\beta - \boldsymbol{v}^\alpha) \tag{2.31}$$

where $f_{\alpha\beta}$ is the diffusive drag coefficient between α and β phases (or constituents) and $f_{\alpha\beta} = f_{\beta\alpha}$. Evidently, Π^α satisfies the following condition

$$\sum_{\alpha=s,w,k} \Pi^\alpha = 0 \tag{2.32}$$

Based on the first law of thermodynamics, we have the following energy conservation relation for the irreversible thermodynamical system

$$\dot{K} + \dot{U} - \dot{D} = \dot{W} + \dot{Q} \tag{2.33}$$

With substitution of Equations (2.11), (2.20), (2.27), (2.29) and (2.30) into (2.33),

we obtain

$$-\int_V \sum_{\alpha=s,w,k}(\nabla\cdot\boldsymbol{\sigma}^\alpha+\rho^\alpha\mathbf{f}^\alpha-\rho^\alpha\dot{\boldsymbol{v}}^\alpha+\Pi^\alpha+p\nabla\phi^\alpha)\cdot\boldsymbol{v}^\alpha dV+\int_V\{[\boldsymbol{F}^s\cdot(\sum_{\alpha=\boldsymbol{s,w,k}}\frac{\partial\mathscr{F}^\alpha}{\partial\boldsymbol{E}})\cdot(\boldsymbol{F}^s)^T-$$
$$-c_0^f J(\sum_{\alpha=s,w,k}\frac{\partial\mathscr{F}^\alpha}{\partial c^f})\mathbf{I}]:\nabla\boldsymbol{v}^s+\sum_{\alpha=s,w,k}[-\boldsymbol{\sigma}^\alpha-p\phi^\alpha\mathbf{I}-(\sum_{\beta=s,w,k}\rho^\alpha\frac{\partial\mathscr{F}^\beta}{\partial\rho^\alpha})\mathbf{I}]:\nabla\boldsymbol{v}^\alpha\}dV+$$
$$+\int_V\sum_{\alpha=s,w,k}(\nabla\cdot\boldsymbol{q}^\alpha+T\rho^\alpha\dot{\eta}^\alpha-\rho^\alpha\gamma^\alpha)dV+\int_V\sum_{\alpha=s,w,k}(\frac{\partial\mathscr{F}^\alpha}{\partial T}+\rho^\alpha\eta^\alpha)\dot{T}dV=0 \tag{2.34}$$

The chemical potential is defined as

$$\mu^\alpha=\frac{\partial\mathscr{F}}{\partial\rho^\alpha} \tag{2.35}$$

Then the chemical term of Equation (2.34) becomes

$$\sum_{\beta=s,w,k}\frac{\partial\mathscr{F}^\beta}{\partial\rho^\alpha}\rho^\alpha=\rho^\alpha\frac{\partial(\sum_\beta\mathscr{F}^\beta)}{\partial\rho^\alpha}=\rho^\alpha\frac{\partial\mathscr{F}}{\partial\rho^\alpha}=\rho^\alpha\mu^\alpha \tag{2.36}$$

The mechanical term in Equation (2.34) can be expressed by the second Piola-Kirchhoff stress tensor τ_E^s and Cauchy stress tensor σ_E^s, which are defined respectively as

$$\boldsymbol{\tau}_E^s=\frac{\partial\mathscr{F}}{\partial\boldsymbol{E}}=\sum_{\alpha=s,w,k}\frac{\partial\mathscr{F}^\alpha}{\partial\boldsymbol{E}} \tag{2.37}$$

$$\boldsymbol{\sigma}_E^s=\boldsymbol{F}^s\cdot\boldsymbol{\tau}_E^s\cdot(\boldsymbol{F}^s)^T \tag{2.38}$$

In order to simplify Equation (2.34), the chemical-expansion stress T_C is introduced to replace the complicated expression, i.e.

$$T_C=c_0^f J(\sum_{\alpha=s,w,k}\rho^\alpha\frac{\partial\mathscr{F}^\alpha}{\partial\rho^\alpha}) \tag{2.39}$$

By substituting Equations (2.36), (2.38) and (2.39) into (2.34), a more complete expression for Equation (2.33) is obtained as

$$-\int_V \sum_{\alpha=s,w,k}(\nabla\cdot\boldsymbol{\sigma}^\alpha+\rho^\alpha\mathbf{f}^\alpha-\rho^\alpha\dot{\boldsymbol{v}}^\alpha+\Pi^\alpha+p\nabla\phi^\alpha)\cdot\boldsymbol{v}^\alpha dV+\int_V\{(\boldsymbol{\sigma}_E^s-T_C\mathbf{I}):\nabla\boldsymbol{v}^s+$$
$$+\sum_{\alpha=s,w,k}[-\boldsymbol{\sigma}^\alpha-p\phi^\alpha\mathbf{I}-(\sum_{\beta=s,w,k}\rho^\alpha\frac{\partial\mathscr{F}^\beta}{\partial\rho^\alpha})\mathbf{I}]:\nabla\boldsymbol{v}^\alpha\}dV+ \tag{2.40}$$
$$+\int_V\sum_{\alpha=s,w,k}(\nabla\cdot\boldsymbol{q}^\alpha+T\rho^\alpha\dot{\eta}^\alpha-\rho^\alpha\gamma^\alpha)dV+\int_V\sum_{\alpha=s,w,k}(\frac{\partial\mathscr{F}^\alpha}{\partial T}+\rho^\alpha\eta^\alpha)\dot{T}dV=0$$

Due to the independence of the variables $\boldsymbol{v}^\alpha$, $\nabla\boldsymbol{v}^\alpha$ and $\dot{T}$, in order to satisfy Equation (2.40), the following equations are derived

Momentum equations

$$\nabla\cdot\boldsymbol{\sigma}^\alpha+\rho^\alpha\mathbf{f}^\alpha-\rho^\alpha\dot{\boldsymbol{v}}^\alpha+\Pi^\alpha+p\nabla\phi^\alpha=0\quad(\alpha=s,w,k) \tag{2.41}$$

Constitutive equations

$$\boldsymbol{\sigma}^s=-\phi^s p\mathbf{I}+\boldsymbol{\sigma}_E^s-\rho^s\mu^s\mathbf{I}-T_C\mathbf{I} \tag{2.42}$$

$$\boldsymbol{\sigma}^\alpha=-\phi^\alpha p\mathbf{I}-\rho^\alpha\mu^\alpha\mathbf{I}\qquad(\alpha=w,k) \tag{2.43}$$

Heat transfer equation

$$\nabla\cdot\boldsymbol{q}^\alpha+T\rho^\alpha\dot{\eta}^\alpha-\rho^\alpha\gamma^\alpha=0\qquad(\alpha=s,w,k) \tag{2.44}$$

By summation of Equation (2.41), the momentum equation for the multiphasic mixture is written as

$$\nabla\cdot\boldsymbol{\sigma}+\rho\mathbf{f}-\rho\dot{\boldsymbol{v}}=0 \tag{2.45}$$

in which $\sigma=\sum_{\alpha=s,w,k}\sigma^\alpha$, $\mathbf{f}=(\sum_{\alpha=s,w,k}\rho^\alpha\mathbf{f}^\alpha)/\rho$ and $\boldsymbol{v}=(\sum_{\alpha=s,w,k}\rho^\alpha\boldsymbol{v}^\alpha)/\rho$. In present studies, the body force **f** and inertial force $\rho\dot{\boldsymbol{v}}$ are neglected and then Equation (2.45) is simplified to

$$\nabla\cdot\boldsymbol{\sigma}=0 \tag{2.46}$$

It is noted that for an osmotic process at constant temperature, the relation between the chemical potential and osmotic pressure p_{osm} can be derived by the Gibbs-Duhem equation as

$$dp_{osm} = \sum_{\alpha=s,w,k} \rho^{\alpha} d\mu^{\alpha} \tag{2.47}$$

Integrating Equation (2.47) we have

$$p_{osm} = \sum_{\alpha=s,w,k} \rho^{\alpha} (\mu^{\alpha} - \mu_0^{\alpha}) \tag{2.48}$$

In summation of Equations (2.42) and (2.43), the constitutive equation for the mixture stress tensor is given as

$$\boldsymbol{\sigma} = \boldsymbol{\sigma}_E^s - (p + T_C)\mathrm{I} \tag{2.49}$$

where the total pressure p includes osmotic pressure p_{osm}. As mentioned above, the chemical-expansion stress T_C is not considered here. With the assumption of isotropic elastic material, $\boldsymbol{\sigma}_E^s$ is written by

$$\boldsymbol{\sigma}_E^s = \lambda_s tr(\boldsymbol{E})\mathrm{I} + 2\mu_s \boldsymbol{E} \tag{2.50}$$

in which λ_s and μ_s are Lame coefficients of solid matrix. Therefore, Equation (2.49) is rewritten as

$$\boldsymbol{\sigma} = -p\mathbf{I} + \lambda_s tr(\boldsymbol{E})\mathbf{I} + 2\mu_s \boldsymbol{E} \tag{2.51}$$

Without consideration of body force and inertial forces, by combining Equations (2.41) and (2.43), the momentum equations of water and ion phase in terms of their chemical potential are obtained as

$$\rho^{\alpha} \nabla \mu^{\alpha} - \Pi^{\alpha} = 0 \qquad (\alpha = w,\ k) \tag{2.52}$$

Substituting Equation (2.31) into (2.52), one can get the momentum equations in terms of the chemical potential and velocity as follows

$$-\rho^{w} \nabla \mu^{w} + f_{ws}(\boldsymbol{v}^{s} - \boldsymbol{v}^{w}) + \sum_{k=1}^{n_f} f_{wk}(\boldsymbol{v}^{k} - \boldsymbol{v}^{w}) = 0 \tag{2.53}$$

$$-\rho^{k} \nabla \mu^{k} + f_{ks}(\boldsymbol{v}^{s} - \boldsymbol{v}^{k}) + f_{kw}(\boldsymbol{v}^{w} - \boldsymbol{v}^{k}) + \sum_{j=1(j\neq k)}^{n_f} f_{kj}(\boldsymbol{v}^{j} - \boldsymbol{v}^{k}) = 0 \tag{2.54}$$

Based on the work of Lai et al. (1991), we obtain the following constitutive equation for the chemical potential for water and ion phases

$$\mu^w = \mu_0^w + \frac{1}{\rho_T^w}(p - RT\sum_{k=1}^{n_f}\Phi^k c^k + \boldsymbol{B}_w tr(\boldsymbol{E})) \tag{2.55}$$

$$\mu^k = \mu_0^k + \frac{RT}{M^k}\ln(\gamma_k c^k) + \frac{z^k F_c \psi}{M^k} \tag{2.56}$$

where $\mu_0^\alpha (\alpha = w, k)$ are the chemical potentials of the phase α at reference configuration, R is the universal gas constant, F_c Faraday constant, $\boldsymbol{B}_w$ the coupling coefficient, ψ electric potential, Φ^k osmotic coefficient of ion k, c^k concentration of ion k, γ_k the activity coefficient of ion k, M^k the molar weight of ion k, z^k valance of the kth ion.

So far the previous works done by Hon et al. (1999) and Lai et al. (1991) are summarized. On the basis of their work, the MECe model is developed as follows. With the reasonable assumption that f_{sk} and f_{kj} are neglected in comparison with f_{ws} and f_{wk}, by Equations (2.53) and (2.54), the simplified formulation for the momentum equation of fluid phase is given as

$$f_{ws}(\boldsymbol{v}^s - \boldsymbol{v}^w) = \sum_{\alpha=w,k}\rho^\alpha \nabla\mu^\alpha \tag{2.57}$$

Substituting the constitutive relations of the mixture and each phase expressed by Equations (2.51), (2.55) and (2.56) into the momentum equations (2.46) and (2.57), we have

$$\nabla\cdot(-p\mathbf{I} + \lambda_s tr(\boldsymbol{E})\mathbf{I} + 2\mu_s \boldsymbol{E}) = 0 \tag{2.58}$$

$$f_{ws}(\boldsymbol{v}^s - \boldsymbol{v}^w) = \phi^w(\nabla p + RT\nabla\sum_k(1-\Phi^k)c^k + F_c\nabla\psi\sum_k z^k c^k + \boldsymbol{B_w}\nabla tr(\boldsymbol{E})) \tag{2.59}$$

With the assumption that ϕ^k is equal to zero, combining Equations (2.2) and

(2.8), one can write

$$\nabla \cdot (\phi^w (\boldsymbol{v}^s - \boldsymbol{v}^w)) = \nabla \cdot \boldsymbol{v}^s \tag{2.60}$$

By using Equation (2.60), Equation (2.59) is rewritten as

$$\nabla \frac{\partial u}{\partial t} = \nabla [\frac{(\phi^w)^2}{f_{ws}} (\nabla p + RT \nabla \sum_k (1 - \Phi^k) c^k + F_c \sum_k z^k c^k \nabla \psi + \boldsymbol{B}_w \nabla tr(\boldsymbol{E}))] \tag{2.61}$$

where u is the displacement of the solid phase.

As is well known, the pressure is caused by the ionic concentration difference between the hydrogel and surrounding solution. In the MECe model, the ionic concentration is determined by a Nernst-Planck equation as follows

$$J_i = -D_k c^k_{,i} - \frac{F_c}{RT} z^k D_k c^k \psi_{,i} + c^k \boldsymbol{v}_i \qquad (k = 1, 2, \ldots n_f) \tag{2.62}$$

where i denotes the spatial direction x_i, the subscript i after a comma indicates partial differentiation with respect to the variable x_i, and D_k is the diffusive coefficient of ion k. The diffusion equation of the ionic species k is

$$\frac{\partial c^k}{\partial t} = -J_{i,i} + r_k \qquad (k = 1, 2, \ldots n_f) \tag{2.63}$$

in which r_k is the source term resulting from the chemical conversion of the molecules.

By combining Equations (2.62) and (2.63), the following convection-diffusion equations are obtained as

$$(D_k c^k{}_{,i})_{,i} + \frac{F_c z^k}{RT} (D_k c^k \psi_{,i})_{,i} = \frac{\partial c_k}{\partial t} + (c^k \boldsymbol{v}_i)_{,i} \quad (k = 1, 2, \ldots n_f) \tag{2.64}$$

where r_k is neglected due to the ideal solution assumption.

In addition, in the MECe model, the externally applied electric field is an important factor for the deformation of hydrogels and it is expressed by the

Poisson equation as

$$\nabla^2\psi = -\frac{F_c}{\varepsilon\varepsilon_0}\sum_{k=1}^{n_f}(z^k c^k + z^f c^f) \tag{2.65}$$

in which the fixed-charge density c^f is given by

$$c^f = \frac{\phi_0^w c_0^f}{\phi^w(1+tr(\boldsymbol{E}))} = \frac{c_0^f}{(1+tr(\boldsymbol{E})/\phi_0^w)} \tag{2.66}$$

where ε is the dielectric constant, ε_0 the permittivity of free space, z^f the valence of the fixed-charge groups, c_0^f the fixed-charge density at the reference configuration and ϕ_0^w the volume fraction of the water phase at the reference configuration.

The full formulation of the MECe model is thus far completed. The model consists of the Nernst-Planck type convection-diffusion equations (2.64) for the ionic concentrations, Poisson equation (2.65) for the electric potential, the mixture continuity equation (2.61) for the fluid pressure and the mixture momentum equation (2.58) for the hydrogel displacement. They are a set of coupled nonlinear partial differential equations and numerically solved here by a hierarchical iteration technique. As shown in Figure 2.1 for the flow chart of the computation, in the inner iteration, the ionic concentrations and electric potential are computed simultaneously by solving Equations (2.64) and (2.65). Then substituting the computed results into the outer iteration, the fluid pressure and hydrogel displacement are obtained respectively by Equations (2.61) and (2.58). Additionally, ϕ^w and c^f required in solving these equations are calculated by Equations (2.5) and (2.66). The developed MECe model can be used for both

transient and steady-state simulations of the electric-sensitive hydrogels.

2.3 Boundary and initial conditions

In this dissertation, only one-dimensional simulations are conducted, and two kinds of boundary conditions are required at the solution ends (electrodes) and the hydrogel-solution interfaces, respectively. The first is the Dirichlet boundary conditions for the ionic concentrations and electric potential applied at two ends of the solution, which are expressed as follows

$$c\,|_{Anode} = c\,|_{Cathode} = c^* \tag{2.67}$$

$$\psi\,|_{Anode} = 0.5V_e \quad \text{and} \quad \psi\,|_{Cathode} = -0.5V_e \tag{2.68}$$

where c^* is the initial ion concentration of the bath solution and V_e the externally applied voltage.

The second kind of boundary conditions is to assign the values of the fluid pressure and hydrogel displacement at the hydrogel-solution interfaces. Based on the assumption that, at equilibrium state, the chemical potentials of water and ion phase within the hydrogels must be equal to those outside the hydrogels, the boundary conditions of the fluid pressure at the hydrogel-solution interfaces are given as

$$p_{\text{interface}} = RT\sum_{k=1}^{n_f}(c^k_{\text{in}-\text{interface}} - c^k_{\text{out}-\text{interface}}) - p_0 \tag{2.69}$$

where $c^k_{\text{in}-\text{interface}}$ are the ion concentrations within the hydrogels near the interfaces, $c^k_{\text{out}-\text{interface}}$ the ion concentrations within exterior solution near the interfaces, and p_0 denotes the fluid pressure at reference configuration. Due to the zero stress

of the mixture phase on the hydrogel-solution interface, the boundary conditions of displacement of the hydrogels on the hydrogel-solution interface are written as

$$\lambda_s tr(\boldsymbol{E}_{\text{interface}})\mathbf{I} + 2\mu_s \boldsymbol{E}_{\text{interface}} = p_{\text{interface}}\mathbf{I} \tag{2.70}$$

The boundary conditions mentioned above are available for both steady-state and transient simulations. However, in the implementation of the transient computations for kinetic study of hydrogels, additional initial conditions are required. It is assumed that the hydrogel is initially in the equilibrium state only under the effect of bath solution without the externally applied electric field. Corresponding to this equilibrium state taken as the initial state for transient analysis, the steady-state simulations are carried out, and then the computed results of all four variables are used as the initial values for the initial conditions of transient analysis. They are

$$c_{initial}^{transient} = c_{v=0}^{steady} \tag{2.71}$$

$$\psi_{initial}^{transient} = \psi_{v=0}^{steady} \tag{2.72}$$

$$p_{initial}^{transient} = p_{v=0}^{steady} \tag{2.73}$$

$$u_{initial}^{transient} = u_{v=0}^{steady} \tag{2.74}$$

where $c_{v=0}^{steady}$, $\psi_{v=0}^{steady}$, $p_{v=0}^{steady}$ and $u_{v=0}^{steady}$ denote the steady-state computed results without the externally applied electric field.

2.4 Non-dimensional implementation

For convenience of coding and computing, a non-dimensional formulation for the computed variables are defined as

$$\bar{\zeta} = \frac{\zeta}{L_{ref}} \qquad \bar{u} = \frac{u}{L_{ref}} \tag{2.75}$$

$$\bar{c}_k = \frac{c_k}{c_{ref}} \qquad \bar{c}_f = \frac{c_f}{c_{ref}} \tag{2.76}$$

$$\bar{\psi} = \frac{\psi}{\psi_{ref}} = \frac{F\psi}{\alpha RT} \tag{2.77}$$

$$\bar{p} = \frac{p}{p_{ref}} = \frac{p}{\beta c_{ref} RT} \tag{2.78}$$

where ζ denotes the spatial coordinate variable, and α, β are non-dimensional adjusting parameters.

Thus, the non-dimensional form of the partial differential governing equations of the MECe model can be obtained as follows

$$(D_k \bar{c}^k{}_{,i})_{,i} + \alpha z^k (D_k \bar{c}^k \bar{\psi}_{,i})_{,i} = L_{ref}^2 \frac{\partial \bar{c}_k}{\partial t} + L_{ref} (\bar{c}^k \boldsymbol{v}_i)_{,i} \tag{2.79}$$

$$\nabla^2 \bar{\psi} = -\frac{F_c^2 L_{ref}^2 c_{ref}}{\varepsilon \varepsilon_0 RT\alpha} \sum_{k=1}^{n_f} (z^k \bar{c}^k + z^f \bar{c}^f) \tag{2.80}$$

$$\beta RT c_{ref} \nabla \cdot (p\mathbf{I}) = \nabla(\lambda_s tr(\boldsymbol{E})\mathbf{I} + 2\mu_s \boldsymbol{E}) \tag{2.81}$$

$$\begin{aligned} \frac{L_{ref}^2}{c_{ref} RT} \nabla \frac{\partial \bar{u}}{\partial t} = \nabla [& \frac{(\phi^w)^2}{f_{ws}} (\beta \nabla \bar{p} + RT \nabla \sum_k (1 - \Phi^k) \bar{c}^k + \\ & + \alpha \sum_k z^k \bar{c}^k \nabla \bar{\psi} + \frac{1}{c_{ref} RT} \boldsymbol{B}_w \nabla tr(\boldsymbol{E}))] \end{aligned} \tag{2.82}$$

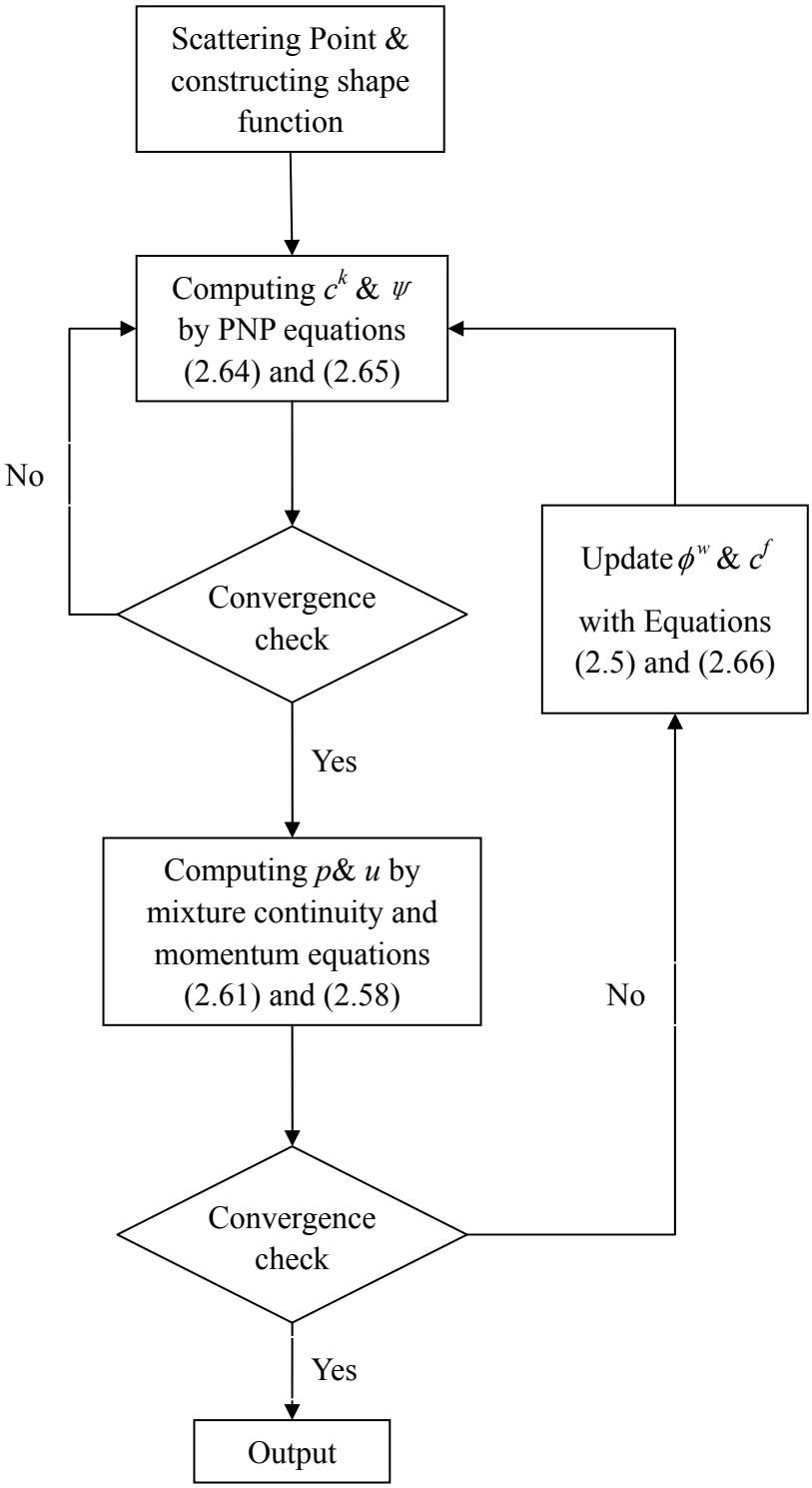

Figure 2.1 Computational flow chart of the developed MECe model.

Chapter 3

Meshless Hermite-Cloud Numerical Method

In this chapter, a meshless numerical technique, called Hermite-Cloud Method (HCM), is introduced in detail, which will be employed for the present numerical simulations. After a brief overview of meshless numerical methods, the development of HCM is fully presented, including the theoretical formulation, computational implementation and numerical validations. An engineering application of HCM is also addressed for the nonlinear fluid-structure analysis of submarine pipelines.

3.1 A brief overview of meshless methods

For decades the finite element method (FEM) has been a dominant numerical tool for modeling and simulation of wide-range engineering problems. However, for some cutting-edge technologies, such as bio-micro-electro-mechanical systems (BioMEMS), which require the multiphysical and multiscale studies commonly, FEM exposes certain disadvantageous features, including the iterative remeshing to track dynamic processes in large deformation problems and the requirement for large storage and memory due to the large number of element nodes involved in FEM discretization. In order to overcome these deficiencies resulting from FEM, various meshless numerical techniques are recently developed (Liu GR, 2003).

According to the use of integration or not, these meshless methods can be classified into two groups. One is based on the strong-form of partial differential equations (PDEs), and it includes the finite point method (Onate et al., 1996) and smooth particle hydrodynamics (SPH) (Lucy, 1977). The other is based on the weak-form of PDEs, and it includes the element-free Galerkin method (EFG) (Belytschko et al., 1994) and diffuse element method (Nayroles et al., 1992). It should be noted that in the field of meshless technique development, Liu GR and his coworkers have made significant contributions by developing several efficient approaches, including the point interpolation method (PIM) (Liu GR and Gu, 2001), the meshless Petrov-Galerkin method (MLPG) (Liu GR et al., 2001) and local point interpolation method (LPIM) (Liu GR and Gu, 2001).

For solution of the presently developed MECe mathematical model, the new meshless HCM is used to solve the complex nonlinear coupled partial differential governing equations. Based on the Hermite interpolation theorem and point collocation as well as reproducing kernels techniques, the HCM is developed as a strong-form truly meshless technique. It employs the Hermite theorem to construct the interpolation functions, where the shape functions are constructed to correspond respectively to the unknown functions and their first-order derivatives. It is formulated on the basis of the classical RKPM but the fixed kernels are used here instead as the kernel function (Aluru and Li, 2001). Furthermore, for a given set of PDEs with the Dirichlet and/or Neumann boundary conditions, certain differential-type auxiliary conditions are derived with the Hermite theorem to

generate a complete set of partial differential boundary value (PDBV) problem. By scattering a set of points in the computational domain and its edges, the point collocation technique is applied for the PDBV discretization. The approximate solutions of both the unknown functions and their first-order derivatives are expressed in terms of the shape functions and unknown point values, resulting in a complete set of discrete algebraic equations. Finally, they are solved with respect to the unknown point values and the numerical solutions of the PDBV problem can be computed in a straightforward manner.

3.2 Development of Hermite-Cloud method

3.2.1 Theoretical formulation

As one of mathematical operators, which can reproduce a function by integration transform over a computational domain, the reproducing kernel method for a 2-D real function $f(x, y)$ in a domain Ω is expressed as follows

$$f(x, y) = \int_{\Omega} \Phi(x - p, y - q) f(p, q) dpdq \tag{3.1}$$

where $\Phi(x, y)$ is a real window function. According to the definition of the reproducing kernel method, the ideal window functions should be orthogonal, and its integration over Ω should be unity, so as to reproduce $f(x, y)$ exactly. Corresponding to various reproducing kernel methods, the selection of window functions is different. However, it is not often easy to select suitable functions because the window functions must satisfy both the conditions to exactly reproduce the unknown function $f(x)$. In the classical RKPM (Liu et al., 1995),

an approximate solution is constructed by introducing a window function $\Phi(x, y)$ as the product of a correction function $C(x, y, p, q)$ and a kernel function $K(x, y)$, that is

$$\Phi(x-p, y-q) = C(x, y, p, q)K(x-p, y-q) \tag{3.2}$$

Substituting Equation (3.2) into Equation (3.1), the approximation $\widetilde{f}(x, y)$ of the unknown function $f(x, y)$ can be rewritten as follows

$$\widetilde{f}(x, y) = \int_{\Omega} C(x, y, p, q)K(x-p, y-q)f(p, q)dpdq \tag{3.3}$$

Further to that mentioned above, the selection of kernel functions also differentiates the various reproducing kernel methods. If the fixed kernel is used as the present kernel function $K(x, y)$, Equation (3.3) can be represented as

$$\widetilde{f}(x, y) = \int_{\Omega} C(x, y, p, q)K(x_k - p, y_k - q)f(p, q)dpdq \tag{3.4}$$

in which the point (x_k, y_k) is the center point of the fixed kernel corresponding to the kernel function $K(x_k - p, y_k - q)$. It should be addressed that, for different PDBV problems, the kernel function may be constructed by different forms of weighted window functions, such as the Gaussian functions, spline functions or radial basis functions. In the present HCM, a cubic spline function is employed to construct the kernel function as

$$K(x_k - p, y_k - q) = W^*((x_k - p)/\Delta x)W^*((y_k - q)/\Delta y)/(\Delta x \Delta y) \tag{3.5}$$

where $W^*(z)$ is a cubic-spline window function and is defined as

$$W^*(z) = \begin{cases} 0 & |z| \geq 2 \\ \dfrac{(2-|z|)^3}{6} & 1 \leq |z| \leq 2 \\ \dfrac{2}{3} - z^2\left(1 - \dfrac{|z|}{2}\right) & |z| \leq 1 \end{cases} \tag{3.6}$$

where $z=(x_k-p)/\Delta x$ for the x-component and $z=(y_k-q)/\Delta y$ for the y-component. Δx and Δy denote the cloud size of the fixed kernel with the center point (x_k, y_k) in x- and y- directions respectively. These parameters are adjusted depending on the point distribution and accuracy requirement, due to the consistency conditions, of the reproducing kernel approach.

It is well-known in mathematics that a continuous function can be expressed as a sum of the linearly independent functions. As a result, the correction function $C(x,y,p,q)$ in Equation (3.4) may be given by

$$C(x,y,p,q)=\mathbf{B}(p,q)\mathbf{C}^*(x,y)=\{b_1(p,q),b_2(p,q),\cdots,b_\beta(p,q)\}\{c_1,c_2,\cdots,c_\beta\}^T \quad (3.7)$$

where $\boldsymbol{C}^*(x,y)$ is a β^{th}-order column coefficient vector and $\mathbf{B}(p,q)$ a β^{th}-order row basis-function vector, in which $b_i(p,q)$ (i=1, 2, …, β) are linearly independent basis functions (β denotes the degree of the polynomials of the basis function). Usually the selection of basic functions depends on the PDBV problems to be solved. For example, for the one- or two-dimensional PDE system, the basis-function vector is defined as respectively

$$\mathbf{B}(p)=\{1,p,p^2,\cdots p^{\beta-1}\} \quad (3.8)$$

$$\mathbf{B}(p,q)=\{b_1(p,q),b_2(p,q),\ldots,b_\beta(p,q)\}=\{1,p,q,p^2,pq,q^2\} \quad (\beta=6) \quad (3.9)$$

The coefficients c_i (i=1, 2, …, β) in the coefficient vector $\boldsymbol{C}^{*T}(x,y)=\{c_1,c_2,\cdots,c_\beta\}$ of Equation (3.7) are unknown and can be determined by the following consistency conditions of the reproducing kernel techniques

$$b_i(x,y)=\int_\Omega C(x,y,p,q)K(x_k-p,y_k-q)b_i(p,q)dpdq \qquad (i=1,2,...,\beta) \quad (3.10)$$

If a set of points is distributed arbitrarily in the integral domain Ω and along

its edges, the point collocation technique can be applied for PDBV discretization. By substituting Equation (3.7) into Equation (3.10), the consistency conditions (3.10), is represented in discrete form as

$$\begin{aligned} b_i(x,y) &= \sum_{n=1}^{N_T} C(x,y,p_n,q_n)K(x_k-p_n,y_k-q_n)b_i(p_n,q_n)\Delta S_n \\ &= \sum_{n=1}^{N_T} \mathbf{B}(p_n,q_n)\mathbf{C}^*(x,y)K(x_k-p_n,y_k-q_n)b_i(p_n,q_n)\Delta S_n \end{aligned} \quad (i=1,2,\ldots,\beta) \tag{3.11}$$

where N_T is the total number of scattered points covering the interior domain Ω and the surrounding edges. The subscript n represents the n^{th} scattered point. ΔS_n denotes the cloud area of the n^{th} point. It is seen that Equation (3.11) is a set of linear algebraic equations with respect to the coefficients c_i (i=1, 2, …, β). Therefore, it can be rewritten in the following matrix form with respect to the coefficient vector $\boldsymbol{C}^{*T}(x,y)=\{c_1,c_2,\cdots,c_\beta\}$

$$\mathbf{B}^T(x,y) = \mathbf{A}(x_k,y_k)\mathbf{C}^*(x,y) \tag{3.12}$$

From Equation (3.12), we obtain

$$\boldsymbol{C}^*(x,y) = \boldsymbol{A}^{-1}(x_k,y_k)\boldsymbol{B}^T(x,y) \tag{3.13}$$

where $\boldsymbol{A}(x_k,y_k)$ is a symmetric constant matrix at the fixed-cloud center point (x_k,y_k)

$$A_{ij}(x_k,y_k) = \sum_{n=1}^{N_T} b_i(p_n,q_n)K(x_k-p_n,y_k-q_n)b_j(p_n,q_n)\Delta S_n \ (i,j=1,2,\cdots,\beta) \tag{3.14}$$

By substituting Equations (3.5), (3.7) and (3.13) into Equation (3.4), the approximate expression $\widetilde{f}(x,y)$ of the unknown real function $f(x,y)$ can be obtained as

$$\begin{aligned}\widetilde{f}(x,y) &= \int_{\Omega} \mathbf{B}(p,q)\mathbf{C}^{*}(x,y)K(x_k-p,y_k-q)f(p,q)dpdq \\ &= \int_{\Omega} \mathbf{B}(p,q)\mathbf{A}^{-1}(x_k,y_k)\mathbf{B}^{T}(x,y)K(x_k-p,y_k-q)f(p,q)dpdq\end{aligned} \tag{3.15}$$

which can further be discretized as

$$\widetilde{f}(x,y) = \sum_{n=1}^{N_T}(\mathbf{B}(p_n,q_n)\mathbf{A}^{-1}(x_k,y_k)\mathbf{B}^{T}(x,y)K(x_k-p_n,y_k-q_n)\Delta S_n)f_n = \sum_{n=1}^{N_T} N_n(x,y)f_n \tag{3.16}$$

where f_n is defined as the point value of the n^{th} point. $N_n(x,y)$ are the shape functions that consist of the basis functions and are simply polynomials in x and y. Thus, any derivative of the shape functions can be easily obtained by the differentiation of basis function vector $\boldsymbol{B}(x,y)$. Furthermore, it is obvious that the present shape functions $N_n(x,y)$ satisfy the consistency conditions (3.10) or (3.11) for all independent basis functions $b_i(x,y)$ (i=1, 2, …, β). In particular, when $b_1(x,y)=1.0$ (i=1), $b_2(x,y)=x$ (i=2) and $b_3(x,y)=y$ (i=3) are taken for the discretized consistency conditions (3.11), we have

$$1.0=\sum_{n=1}^{N_T} N_n(x,y), \qquad x=\sum_{n=1}^{N_T} N_n(x,y)x_n, \qquad y=\sum_{n=1}^{N_T} N_n(x,y)y_n \tag{3.17}$$

According to the Hermite theorem, the first-order derivatives of the unknown real function $f(x,y)$ with respect to the variables x and y are defined as

$$g_x(x,y)=\frac{\partial f(x,y)}{\partial x}, \qquad g_y(x,y)=\frac{\partial f(x,y)}{\partial y} \tag{3.18}$$

When they are discretized by imposing Equation (3.16) in a similar manner, their approximate expression can be written as

$$\widetilde{g}_x(x,y)=\sum_{m=1}^{N_S} M_m(x,y)g_{xm} \tag{3.19}$$

$$\widetilde{g}_y(x,y)=\sum_{m=1}^{N_S}M_m(x,y)g_{ym} \tag{3.20}$$

where $N_S(\le N_T)$ is the total number of scattered points, and g_{xm} and g_{ym} are the unknown point values for the m^{th} point. $M_m(x,y)$ are the shape functions corresponding to the unknown first-order differential functions $g_x(x,y)$ and $g_y(x,y)$, but their basis functions are now $B_g(x,y)\in R^{\beta-1}$.

Based on the Hermite interpolation theorem, a true meshless approximation $\widetilde{f}(x,y)$ of the unknown real function $f(x,y)$ can now be finally constructed in the following form

$$\begin{aligned}\widetilde{f}(x,y)=&\sum_{n=1}^{N_T}N_n(x,y)f_n+\sum_{m=1}^{N_S}(x-\sum_{n=1}^{N_T}N_n(x,y)x_n)M_m(x,y)g_{xm}+\\&+\sum_{m=1}^{N_S}(y-\sum_{n=1}^{N_T}N_n(x,y)y_n)M_m(x,y)g_{ym}\end{aligned} \tag{3.21}$$

It is noted that there are many computational advantages in the presently constructed Hermite-based interpolation approximation. Most notably, the computational accuracy at scattered discrete points in the domain is much refined not only for the approximate functions, but also for their first-order derivatives. This is clearly demonstrated in the subsequently formulated equations (3.30)-(3.33), in which the final unknown vector of the set of the algebraic governing equations is derived by the discretized partial differential governing equations, and consists of all three unknown point-value vectors $\{f_n\}_{1\times N_T}$, $\{g_{xm}\}_{1\times N_S}$ and $\{g_{ym}\}_{1\times N_S}$ corresponding to the approximate solutions of both the unknown functions and their first-order derivatives, which can thus be computed directly. In addition, the Hermite-based interpolation approximation (3.21) is also

used for construction of the following necessary auxiliary conditions.

Due to the inclusion of additional unknown functions $g_x(x,y)$ and $g_y(x,y)$, certain auxiliary conditions are required to generate a complete set of PDBV equations. Based on Equation (3.18) for the defined $g_x(x,y)$ and $g_y(x,y)$, the following auxiliary conditions are developed naturally with consideration of Equations (3.17) and (3.19)-(3.21)

$$\sum_{n=1}^{N_T} N_{n,x}(x,y) f_n - \sum_{m=1}^{N_S} (\sum_{n=1}^{N_T} (N_{n,x}(x,y) x_n)) M_m(x,y) g_{xm} - \\ - \sum_{m=1}^{N_S} (\sum_{n=1}^{N_T} (N_{n,x}(x,y) y_n)) M_m(x,y) g_{ym} = 0 \tag{3.22}$$

$$\sum_{n=1}^{N_T} N_{n,y}(x,y) f_n - \sum_{m=1}^{N_S} (\sum_{n=1}^{N_T} (N_{n,y}(x,y) y_n)) M_m(x,y) g_{ym} - \\ - \sum_{m=1}^{N_S} (\sum_{n=1}^{N_T} (N_{n,y}(x,y) x_n)) M_m(x,y) g_{xm} = 0 \tag{3.23}$$

where the variable in the subscript after a comma indicates partial differentiation with respect to that variable. These auxiliary conditions are a necessary requirement in the implementation of the proposed HCM.

Hence, the above formulation defines the HCM. In summary, on the basis of the Hermite interpolation theorem, HCM consists of the approximation $\widetilde{f}(x,y)$ of the unknown function $f(x,y)$, the approximations $\widetilde{g}_x(x,y)$ and $\widetilde{g}_y(x,y)$ of the first-order derivatives $g_x(x,y)$ and $g_y(x,y)$, and further combines the necessary auxiliary conditions.

3.2.2 Computational implementation

In general, engineering PDBV problems can be written as

$$\boldsymbol{L}f(x,y) = P(x,y) \quad \text{PDEs in interior domain } \Omega \tag{3.24}$$

$$f(x,y) = Q(x,y) \quad \text{Dirichlet boundary condition on } \Gamma_D \tag{3.25}$$

$$\frac{\partial f(x,y)}{\partial n} = R(x,y) \quad \text{Neumann boundary condition on } \Gamma_N \tag{3.26}$$

where L is a differential operator and $f(x,y)$ an unknown real function. By the point collocation technique and taking $\widetilde{f}(x,y)$ as the approximation of $f(x,y)$, the problem is discretized and expressed approximately by

$$\boldsymbol{L}\widetilde{f}(x_i,y_i) = P(x_i,y_i) \qquad i=1,2,\ldots,N_\Omega \tag{3.27}$$

$$\widetilde{f}(x_i,y_i) = Q(x_i,y_i) \qquad i=1,2,\ldots,N_D \tag{3.28}$$

$$\frac{\partial \widetilde{f}(x_i,y_i)}{\partial n} = R(x_i,y_i) \qquad i=1,2,\ldots,N_N \tag{3.29}$$

where N_Ω, N_D and N_N are the numbers of scattered points in the interior domain, and along the Dirichlet and Neumann edges, respectively, and the total number of scattered points is thus N_T=(N_Ω+N_D+N_N).

With the substitution of the approximations (3.19)-(3.21) into Equations (3.27)-(3.29), and further combining the auxiliary conditions (3.22) and (3.23), followed by rearrangement of the resulting equations, a set of discrete algebraic governing equations with respect to the unknown point values f_i, g_{xi} and g_{yi}, is derived and expressed in the following matrix form as

$$[H_{ij}]_{(N_T+2N_S)\times(N_T+2N_S)}\{F_i\}_{(N_T+2N_S)\times 1} = \{d_i\}_{(N_T+2N_S)\times 1} \tag{3.30}$$

where $\{d_i\}$ and $\{F_i\}$ are (N_T+2N_S)-order column vectors, with

$$\{F_i\}_{(N_T+2N_S)\times 1} = \{\{f_i\}_{1\times N_T},\{g_{xi}\}_{1\times N_S},\{g_{yi}\}_{1\times N_S}\}^T \tag{3.31}$$

$$\{d_i\}_{(N_T+2N_S)\times 1} = \{\{P(x_i,y_i)\}_{1\times N_\Omega},\{Q(x_i,y_i)\}_{1\times N_D},\{R(x_i,y_i)\}_{1\times N_N},\{0\}_{1\times 2N_S}\}^T \tag{3.32}$$

and $[H_{ij}]$ is a $(N_T+2N_S)\times(N_T+2N_S)$ coefficient square matrix

$$[H_{ij}]=\begin{bmatrix} [\boldsymbol{L}N_j(x_i,y_i)]_{N_\Omega\times N_T} & [\boldsymbol{L}((x_i-\sum_{n=1}^{N_T}N_n(x_i,y_i)x_n)M_j(x_i,y_i))]_{N_\Omega\times N_S} & [\boldsymbol{L}((y_i-\sum_{n=1}^{N_T}N_n(x_i,y_i)y_n)M_j(x_i,y_i))]_{N_\Omega\times N_S} \\ [N_j(x_i,y_i)]_{N_D\times N_T} & [0]_{N_D\times N_S} & [0]_{N_D\times N_S} \\ [0]_{N_N\times N_T} & [M_j(x_i,y_i)]_{N_N\times N_S} & [M_j(x_i,y_i)]_{N_N\times N_S} \\ [N_{j,x}(x_i,y_i)]_{N_S\times N_T} & [-(\sum_{n=1}^{N_T}N_{n,x}(x_i,y_i)x_n)M_j(x_i,y_i)]_{N_S\times N_S} & [-(\sum_{n=1}^{N_T}N_{n,x}(x_i,y_i)y_n)M_j(x_i,y_i)]_{N_S\times N_S} \\ [N_{j,y}(x_i,y_i)]_{N_S\times N_T} & [-(\sum_{n=1}^{N_T}N_{n,y}(x_i,y_i)x_n)M_j(x_i,y_i)]_{N_S\times N_S} & [-(\sum_{n=1}^{N_T}N_{n,y}(x_i,y_i)y_n)M_j(x_i,y_i)]_{N_S\times N_S} \end{bmatrix} \tag{3.33}$$

By solving numerically the complete set of linear algebraic equations, equation (3.30), (N_T+2N_S) point values $\{F_i\}$ are obtained, consisting of the N_T point values $\{f_i\}$ and $2N_S$ point values $\{g_{xi}\}$ and $\{g_{yi}\}$. The approximate solution $\widetilde{f}(x,y)$ and the first-order derivatives $\widetilde{g}_x(x,y)$ and $\widetilde{g}_y(x,y)$ of the PDBV problem can be computed through Equations (3.21), (3.19) and (3.20) respectively.

3.2.3 Numerical validations

In order to examine the numerical stability and accuracy of the present HCM, numerical comparisons are made here for several 2-D plane-stress elasticity problems, including a higher-order patch subjected to a uniform unit-intensity unidirectional stress by comparison with exact solutions, cantilever beams subjected to linearly varying axial loads or shear end loads by comparison with the meshless *h*M-DOR method (Ng et al., 2003), and a 2-D thermo-elasticity analysis by comparison with the meshless Finite Cloud method (Aluru and Li, 2001). These comparisons indicate that the computational accuracy of the present HCM at scattered discrete points in the domain is much refined not only for the approximate solutions, but also for the first-order derivatives of these solutions (Li

et al., 2003). To measure the numerical accuracy of the present HCM, a refined global error ξ is defined for the numerical comparison

$$\xi = \frac{1}{|f_{\max}|}\sqrt{\frac{1}{N_T}\sum_{i=1}^{N_T}(\tilde{f}_i - f_i)^2} \tag{3.34}$$

3.2.3.1 Higher-order patch

For an isotropic higher-order patch subjected to uniform unidirectional stress of unit magnitude, as shown in Figure 3.1, the plane-stress equilibrium governing equations are given in terms of the displacements u and v as follows

$$\frac{E}{1-\mu^2}\left(\frac{\partial^2 u}{\partial x^2} + \frac{1-\mu}{2}\frac{\partial^2 u}{\partial y^2} + \frac{1+\mu}{2}\frac{\partial^2 v}{\partial x \partial y}\right) + X_x = 0 \tag{3.35}$$

$$\frac{E}{1-\mu^2}\left(\frac{\partial^2 v}{\partial y^2} + \frac{1-\mu}{2}\frac{\partial^2 v}{\partial x^2} + \frac{1+\mu}{2}\frac{\partial^2 u}{\partial x \partial y}\right) + X_y = 0 \tag{3.36}$$

where E is the elastic modulus and μ the Poisson's ratio. X_x and X_y denote the body forces in the x and y directions, respectively.

When the material constants are taken as E=1 and μ=0.25, the exact solution of this problem is

$$u(x, y) = x\,, \qquad v(x, y) = -0.25y \tag{3.37}$$

By implementation of presently developed HCM, the displacements u and v are obtained numerically, as shown in Figures 3.2(a) and 3.2(b). It is observed that, for a point distribution 5×3, the global errors are $\xi=3.19\times10^{-7}$ for the displacement u, and $\xi=3.32\times10^{-7}$ for the displacement v when the numerical solution is compared with the exact one. It is evident that the present HCM can achieve almost exact results at the scattered discrete points even with a coarse 5×3 point

distribution for the present patch test problem. This example clearly indicates that the efficiency and ease of implementation of the present HCM are much improved over that of existing generic meshless techniques, such as the EFG method, since the HCM does not require a mesh background and has better consistency characteristics in the construction of the shape functions.

3.2.3.2 Cantilever beam subjected to various loadings

With the same equilibrium governing equations as Equations (3.35) and (3.36), a 2-D plane-stress cantilever beam is studied here. It is subjected to a linearly varying axial end load and a shear end load as shown in Figure 3.3 and Figure 3.5, respectively.

The exact solution for the case shown in Figure 3.3 is given by

$$u(x,y) = xy\,, \qquad v(x,y) = -(4x^2 + y^2)/8 \tag{3.38}$$

With the application of the HCM for this elastic analysis, the numerical displacements u and v are computed and plotted in Figures 3.4(a) and 3.4(b). It is again noted that, for the same coarse 5×3 point distribution, comparison with the exact solution reveals the global errors $\xi=1.61\times10^{-6}$ for the displacement u and $\xi=3.86\times10^{-6}$ for the displacement v.

In addition, the exact solution for the cantilever beam subjected to a shear end load, as shown in Figure 3.5, is given by

$$u(x,y) = -\frac{P(y-0.5D)}{6EI}[(6L-3x)x + (2+\mu)(y^2 - 2Dy)] \tag{3.39}$$

$$v(x,y) = \frac{P}{6EI}[3\mu(y^2 - 2Dy + 0.5D^2)(L-x) + (1+1.25\mu)D^2x + (3L-x)x^2] \tag{3.40}$$

where $I = D^3/12$ and D and L are respectively the height and length of the cantilever beam.

The displacement fields are solved numerically by the HCM, and the computed displacement profiles are illustrated in Figures 3.6(a) and 3.6(b). Further, in order to examine the present HCM convergence, the convergence comparison between the HCM and the meshless *h*M-DOR method (Ng et al., 2003) is made in Table 3.1. It is observed from the table that the HCM global errors of both the displacement u and first-order derivative $u_{,x}$ decrease monotonically with increasing the scattered points, and the HCM global errors are smaller than those of the *h*M-DOR method (Ng et al., 2003). These numerical results thus verify the HCM advantages mentioned above, that is, the HCM computational accuracy at scattered discrete points in the domain is much refined not only for the approximate solutions, but also for the first-order derivatives of these solutions.

3.2.3.3 Coupled thermo-elasticity

A plane-stress analysis of coupled thermo-elasticity is conducted here by the developed HCM, as shown in Figure 3.7. The partial differential governing equations in terms of the displacements u and v and temperature T consist of the heat conduction equation and the generic thermo-stress elastic equations as follows

$$\frac{\partial^2 T}{\partial x^2} + \frac{\partial^2 T}{\partial y^2} = h \tag{3.41}$$

$$\frac{\partial^2 u}{\partial x^2}+\frac{1-\mu}{2}\frac{\partial^2 u}{\partial y^2}+\frac{1+\mu}{2}\frac{\partial^2 v}{\partial x\partial y}-(1+\mu)\alpha\frac{\partial(T-T_0)}{\partial x}=0 \tag{3.42}$$

$$\frac{\partial^2 v}{\partial y^2}+\frac{1-\mu}{2}\frac{\partial^2 v}{\partial x^2}+\frac{1+\mu}{2}\frac{\partial^2 u}{\partial x\partial y}-(1+\mu)\alpha\frac{\partial(T-T_0)}{\partial y}=0 \tag{3.43}$$

where h is the heat source, T_0 the initial reference temperature and α the coefficient of thermal expansion. The considered boundary conditions are

$$u(x,y)=0,\quad \sigma_{xy}(x,y)=0,\quad T_{,x}(x,y)=0,\quad \text{at } x\text{=0 and 1} \tag{3.44}$$

$$v(x,y)=0,\quad \sigma_{xy}(x,y)=0,\quad T(x,y)=0,\quad \text{at } y\text{=0} \tag{3.45}$$

$$\sigma_{xy}(x,y)=0,\quad \sigma_{yy}(x,y)=0,\quad T(x,y)=0,\quad \text{at } y\text{=1} \tag{3.46}$$

If we take $T_0=0$, $h=20$, $E=3.0\times10^7$, $\alpha=0.001$ and $\mu=0.25$, the exact solutions of this coupled thermo-elasticity problem are

$$T(x,y)=10y^2,\quad u(x,y)=0,\quad v(x,y)=10\alpha(1+\mu)y^3/3=0.0125y^3/3 \tag{3.47}$$

Again the computations are carried out with the developed HCM, and the variable fields $T(x,y)$, $u(x,y)$ and $v(x,y)$ and their first-order derivatives are obtained numerically, with a regular 5×5 point distribution. The numerical results demonstrate that the standard error of the displacement u is of the order of 10^{-11} and the global error of the temperature $T(x,y)$ is less than 1.0×10^{-7}. A probable reason for the excellent results is that the exact solutions of u and T can be found in the basis functions. However, this explanation is not applicable for the numerical results of the displacement v because its exact cubic solution does not exist in any of the basis functions. In comparison with the exact solution, Figure 3.8 presents the accuracy variation of the displacement v with the increase of the regularly scattered points, for N_T (total point number) = 25 (5×5), 121 (11×11)

and 441 (21×21). It is evident that the computed accuracy of displacement v is significantly refined with increasing the scattered points. Figure 3.9 compares the convergence characteristics of the present displacement $v(x,y)$ and the first-derivatives $v_{,y}(x,y)$ with those obtained by the meshless Finite Cloud method (Aluru and Li, 2001). Present HCM convergence rates are 2.12 for $v(x,y)$ and 1.89 for $v_{,y}(x,y)$ while those of the Finite Cloud method are 2.2 for $v(x,y)$ and 1.95 for $v_{,y}(x,y)$. Therefore, it is convinced that the present HCM can achieve better computational accuracy for both the field-variable solution and the first-order derivative than the Finite Cloud method.

3.3 An application for nonlinear fluid-structure analysis of submarine pipelines

As an application of the present HCM in submarine engineering, a nonlinear fluid-structure interaction of near-bed submarine pipelines under a current is studied (Li et al., 2004) in this section. As is well known, if a submarine pipeline is placed near the seabed, the horizontal current is not symmetrical to the pipeline because of the influence of seabed. As such, a downward external load is produced and applied on the pipeline, resulting in the deformation of pipeline. This problem can be simplified as a beam with various boundary supporting conditions. In a previously published work, Lam et al. (2002) simplified the pipeline as a Bernoulli-Euler beam by the assumption that there is no transverse shear strain, and they studied the static behavior of the pipeline under a static

nonlinear external load. However, the assumption is not applicable for some problems, such as the case when the ratio of length to diameter of the pipeline is not very large, and then the effect of shear deformation can not be neglected. In order to overcome the limit, the Timoshenko beam theory (Reddy, 1993) is introduced here to include the effect of transverse shear deformation.

According to the Timoshenko beam theory, the governing equations of the pipeline are generally written as

$$\frac{\partial}{\partial x}[GAk_s(\frac{\partial w}{\partial x}+\theta)]+f(x)=0 \tag{3.48}$$

$$\frac{\partial}{\partial x}(EI\frac{\partial \theta}{\partial x})-GAk_s(\frac{\partial w}{\partial x}+\theta)=0 \tag{3.49}$$

where w is the pipeline deflection, θ the rotation, G the shear modulus, A the cross section area, k_s the shear correction coefficient, E the elasticity modulus and I the inertia moment. The corresponding boundary conditions are generally given as

$$w(x_0)=\overline{w}, \quad \text{on} \quad \Gamma_w \tag{3.50}$$

$$\theta(x_0)=\overline{\theta}, \quad \text{on}\,\Gamma_\theta \tag{3.51}$$

$$M(x_0)=EI\frac{\partial \theta}{\partial x}\Big|_{x=x_0}=\overline{M}, \qquad \text{on} \quad \Gamma_M \tag{3.52}$$

$$V(x_0)=GAk_s(\theta+\frac{\partial w}{\partial x})\Big|_{x=x_0}=\overline{V}, \qquad \text{on} \quad \Gamma_V \tag{3.53}$$

in which Γ_w, Γ_θ, Γ_M and Γ_V are the boundaries where w, θ, M and V are satisfied, respectively. With the fully fixed boundary conditions of the present study, $\overline{w}$ and $\overline{\theta}$ are equal to zero.

In the governing equation (3.48), $f(x)$ is the fluid load caused by the difference of current pressure. Because the analytical solution of $f(x)$ converges slowly, Lam

et al. (2002) constructed the approximation of the exact solution by the boundary element method (BEM) to speed up the computation. The numerical results match well with the analytical solution of Lai et al. (2002). Thus, the expression of fluid load $f(x)$ is given as

$$f(x) = \frac{1}{2}\rho A U_0^2 c(d) \tag{3.54}$$

where ρ is the mass density, U_0 the current velocity, c and d are dimensionless coefficients and they are defined by the following relation

$$c(d) = \frac{2.23d^2 + 12.54d + 0.02}{0.77d^3 + 0.44d^2 + 0.02d} \tag{3.55}$$

in which d is defined as $d = (D_0 - w(x) - R_s)/(2R_s)$, and D_0 is the distance between the seabed and the central line of pipeline at initial stage, and R_s the pipe outer radius.

It is observed from Equations (3.54) and (3.55) that the fluid load $f(x)$ is a nonlinear variable related to the deflection $w(x)$. The governing equations (3.48) and (3.49) for the pipeline deformation are thus a set of coupled nonlinear equations. It is also noted that, when the material and dimension of pipelines are given, the fluid load $f(x)$ is a function of both the current velocity U_0 and the gap D_0. This means that the deformation behaviors of the near-bed submarine pipelines are greatly affected by these two parameters.

Several simulations are carried out here for a circular steel pipeline placed near the seabed under a static current, as shown in Figure 3.10. The relevant physical and material parameters given are the pipeline length L=10(m), R_s=0.5(m), the thickness of steel pipeline t_s=0.02(m), D_0=0.7(m),

E=2.11×10^{11} (N/m^2), Poisson ratio ν =0.3, ρ_s =7800(kg/m^3), steel yield stress Y_s=2.5×10^8 (N/m^2), and the allowable deflection/span ratio Y_w=0.004. It is seen that the ratio L/R_s is not very large. As such, the pipeline should be simplified as a thick beam fixed at two ends. By the Timosheko beam theory and meshless Hermite-Cloud method, numerical simulations are conducted and then discussions are presented subsequently.

The variation of mid-point deflection $w_{L/2}$ with the current velocity U_0 is illustrated in Figure 3.11. It is observed that, the deflection enlarges with the increase of current velocity U_0 until a critical value U_{cb}. If the velocity U_0 is under the critical value U_{cb}, the computed deflection converges well with the iterations and the pipeline reaches the stable equilibrium. However, when the velocity U_0 is larger than the critical one U_{cb}, the computed deflection does not converge, which is defined as the instability, and then the pipeline will fall into the seabed. This is the first failure pattern of pipelines, termed the instability failure.

Figure 3.12 reveals the influence of the distance D_0 on the critical current velocities U_{cb} caused by instability failure. It is shown that U_{cb} is a monotonically increasing function of D_0. As indicated in Equations (3.54)-(3.55), when other variables are given, the fluid load $f(x)$ decreases with the enlargement of D_0, and increases with increasing U_0. Therefore, in order to attain the same critical fluid force causing the pipeline to lose the stability, it is reasonable to require a higher critical velocity U_{cb} corresponding to an increasing D_0. It is also expected that the critical velocity U_{cb} becomes infinite when the gap grows to be infinite, since the

effect of seabed on the current is then zero and the flow keeps the symmetry.

Sometimes failure due to the material properties happens before the instability failure, thus it is necessary to discuss the material failure here. The distribution of stress along the pipeline is plotted in Figure 3.13. Although the presently observed curve is similar to that of a fully fixed beam under the uniform load, their essential characteristics are different. For the full-fixed beam subject to uniform load, the maximal absolute value of stresses or moments along the beam occurs at the middle point, while the present maximal absolute value of stresses or moments appears at the end points, as shown in Figure 3.13. This phenomenon results from the different external load distribution. In this discussed problem, the fluid load $f(x)$ is coupled with the pipeline deflection $w(x)$ as a decreasing function. Since the deflections at two ends due to the fully fixed boundary conditions are equal to zero and thus are always smaller than that of middle point, it is known by Equations (3.54) and (3.55) that the fluid load $f(x)$ at two ends is larger than that at middle point. Therefore, the characteristic of the beam when the load is independently imposed on the beam is totally different from that coupled with the deflection of pipeline.

Figure 3.14 presents the critical velocities caused respectively by the two types of material failures – the strength failure and the deflection failure. As mentioned above, the stress at end points and the deflection at the middle point firstly reach the respective critical values along the whole pipeline. Thus it is reasonable to define their corresponding critical current velocities as the critical

values of the whole pipeline system. It is seen from Figures 3.14(a) and 3.14(b) that, with the increase of current velocity U_0, both the stress at end point and deflection at middle point increase. When they reach the yield stress and allowable deflection respectively, the corresponding critical velocities U_{cs} and U_{cw} are obtained.

Similarly, for analysis of the influence of the distance D_0 between the pipeline and seabed on the critical velocities of different failure patterns, the variations of respective critical velocities including U_{cb} due to instability failure, U_{cs} due to strength failure and U_{cw} due to deflection failure, with the gap D_0 are synthetically plotted in Figure 3.15. It is found from the figure that bifurcations occur at both points A and B. It means that, beyond point A, the pipeline will not break down because of the stability loss, since the strength failure always appears before the instability failure. The present results agree well with Lam's work (2002), in which the pipeline is simplified as a Bernoulli-Euler beam.

Table 3.1 Numerical comparisons between the present Hermite-Cloud method and the *h*M-DOR method for a cantilever beam subjected to a shear end load (E=3.0×10^7, D=1, L=8 and μ=0.25).

Points Distribution ($N_x \times N_y$)	Global Error (ξ) for u		Global Error (ξ) for $u_{,x}$	
	*h*M-DOR	Hermite-Cloud	*h*M-DOR	Hermite-Cloud
5×11	35.9%	35.9%	30.9%	30.9%
11×11	17.9%	17.7%	15.0%	14.9%
21×11	6.16%	5.92%	5.38%	5.19%
65×11	4.28%	1.95%	3.92%	2.13%
81×11	4.01%	0.384%	3.90%	1.92%

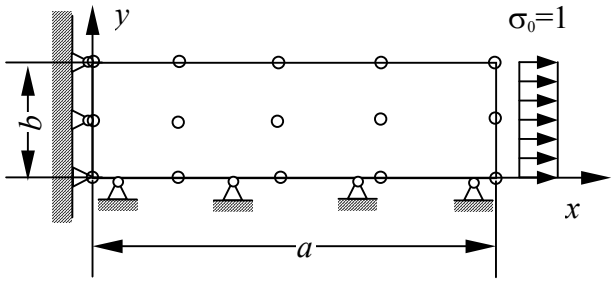

Figure 3.1 Geometry and point distribution for the higher-order patch subjected to a uniform unidirectional stress of unit magnitude.

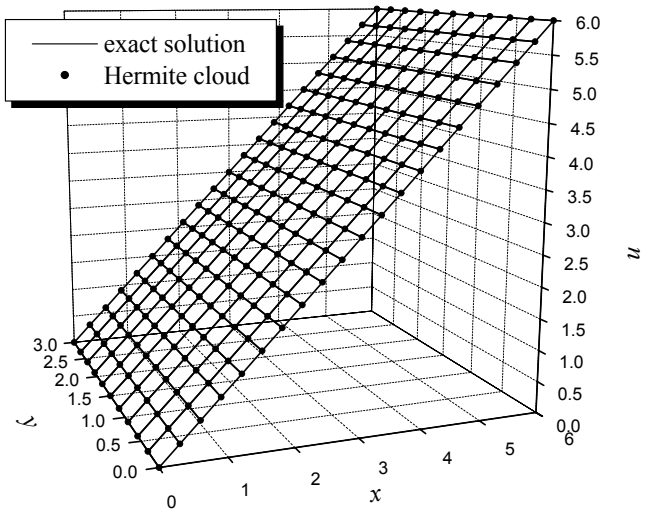

Figure 3.2(a) Numerical comparison of displacement *u* for the higher-order patch subjected to a uniform unidirectional stress of unit magnitude.

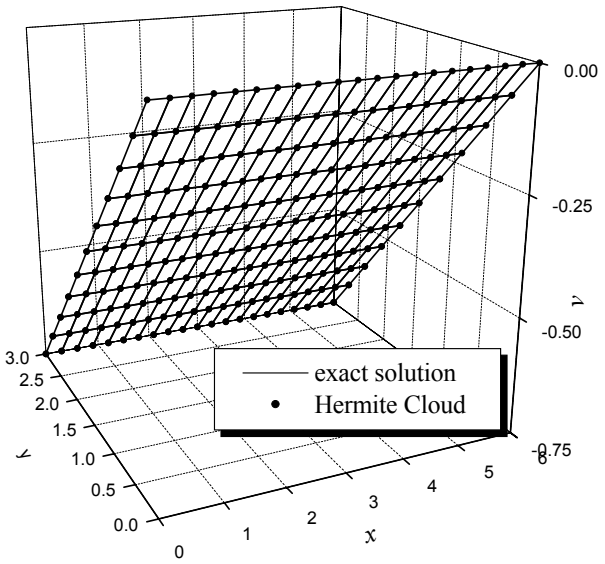

Figure 3.2(b) Numerical comparison of displacement *v* for the higher-order patch subjected to a uniform unidirectional stress of unit magnitude.

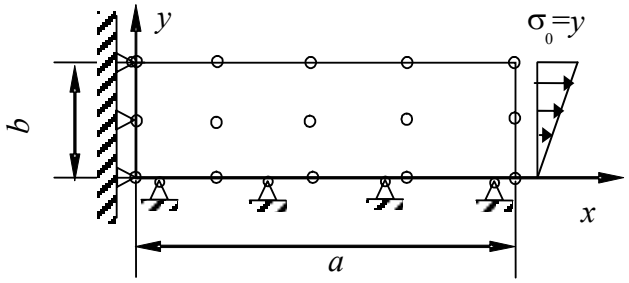

Figure 3.3 Geometry and point distribution for a cantilever beam subjected to a linearly varying axial load at the end of the beam.

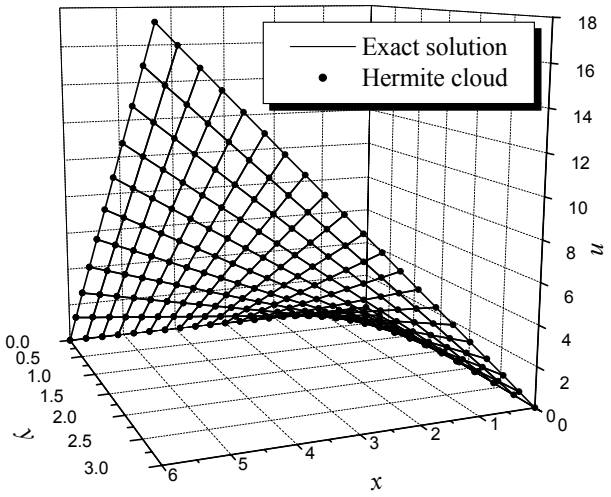

Figure 3.4(a) Numerical comparison of displacement u for the cantilever beam subjected to a linearly varying axial load at the end of the beam.

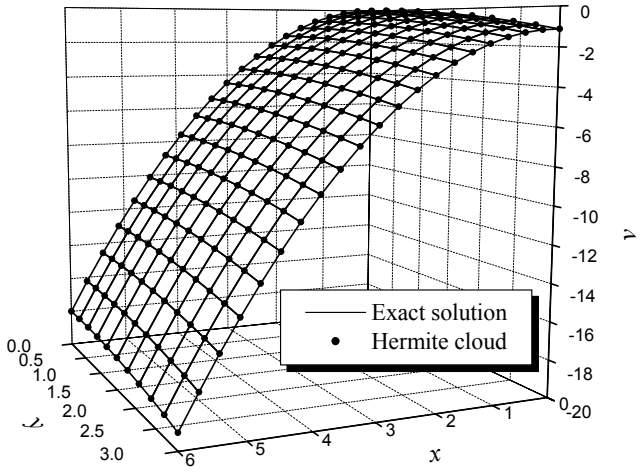

Figure 3.4(b) Numerical comparison of displacement v for the cantilever beam subjected to a linearly varying axial load at the end of the beam.

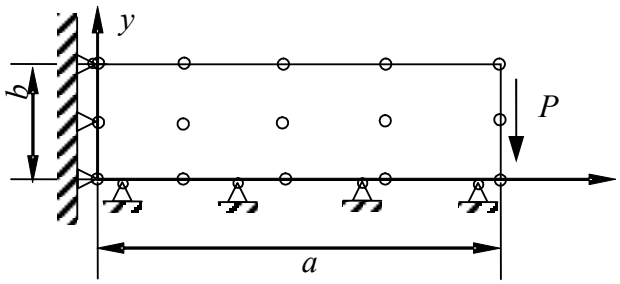

Figure 3.5 Geometry and point distribution for a cantilever beam subjected to a shear load at the end of the beam.

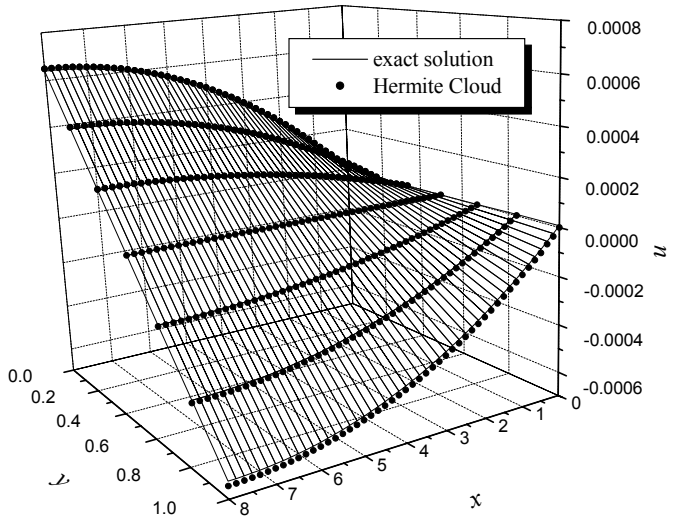

Figure 3.6(a) Numerical comparison of displacement *u* for the cantilever beam subjected to a shear load at the end of the beam.

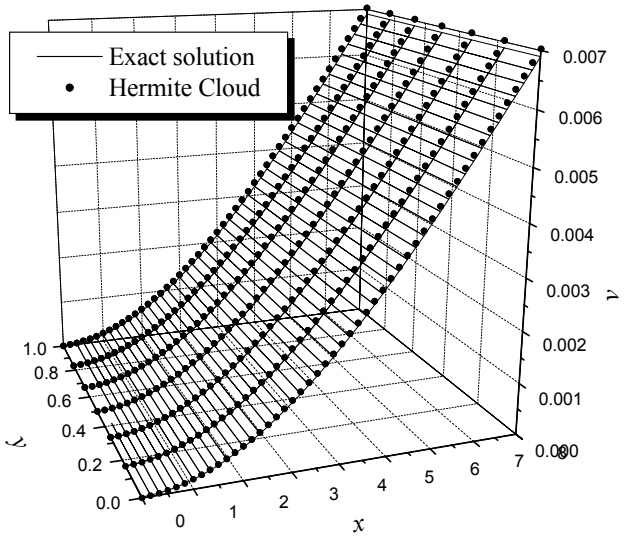

Figure 3.6(b) Numerical comparison of displacement v for the cantilever beam subjected to a shear load at the end of the beam.

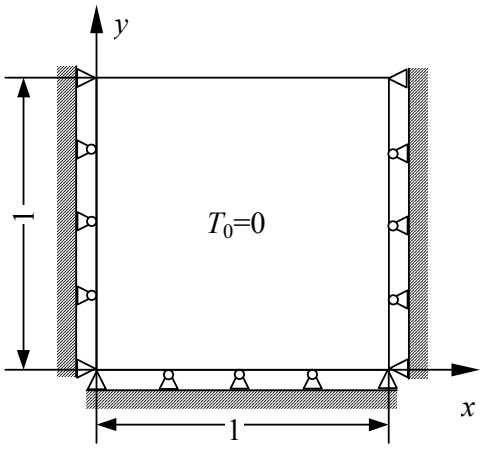

Figure 3.7 Geometry of the 2-D thermoelasticity problem.

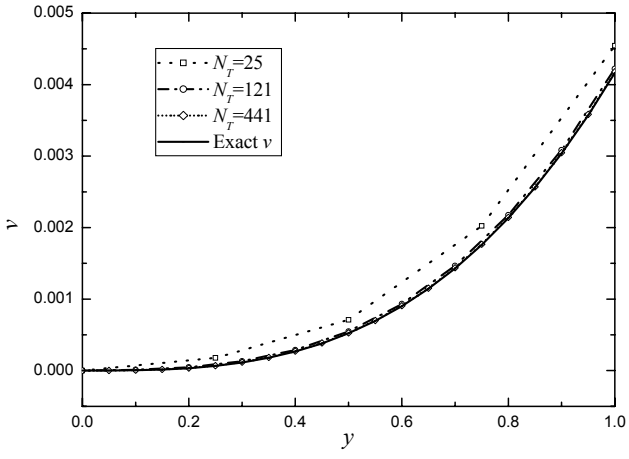

Figure 3.8 Variation of the numerical displacement v with the point distribution density for the thermo-elasticity case.

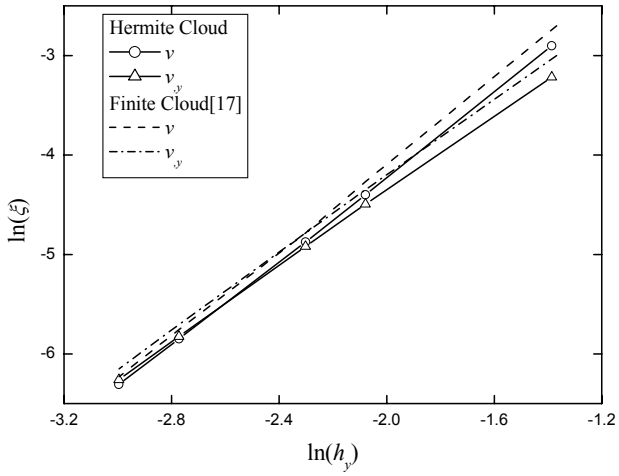

Figure 3.9 Convergence comparison between the present Hermite-Cloud method and Finite-Cloud method for the thermo-elasticity case

(ξ– global error, h – point distance).

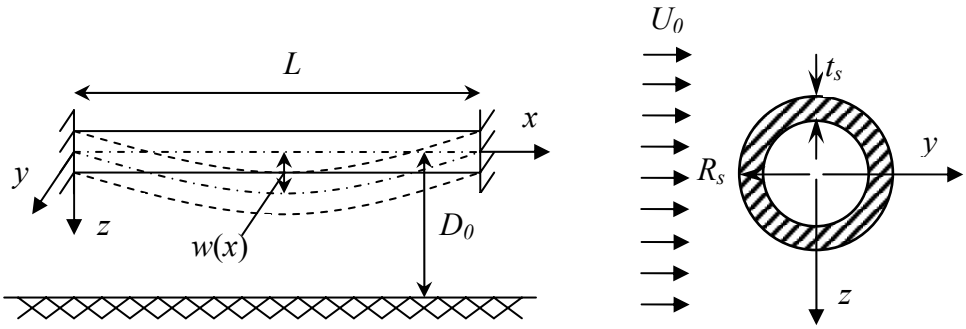

Figure 3.10 Schematic diagram of a submarine pipeline and its deformation under a current.

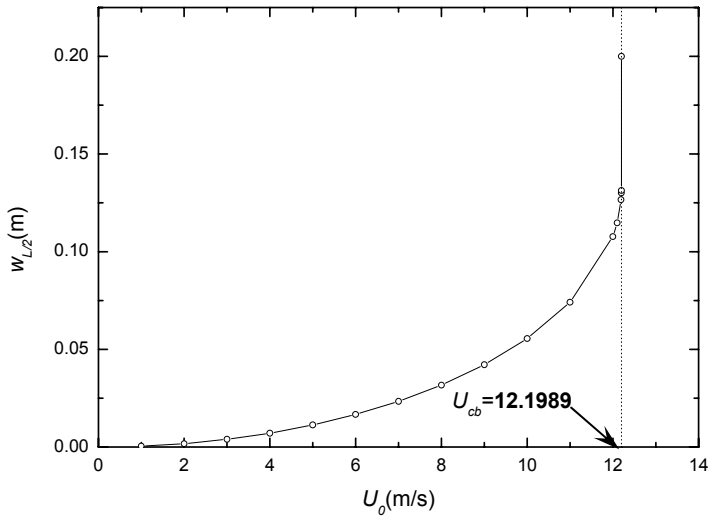

Figure 3.11 Variation of the deflection at the mid-point of pipeline with respect to the current velocity U_0 (when D_0=0.7m).

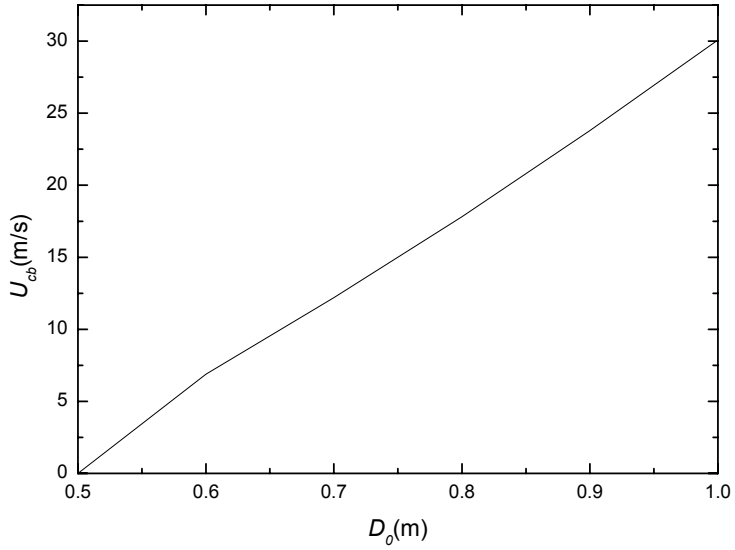

Figure 3.12 Effect of the gap D_0 on the critical velocities U_{cb} of the instability failure.

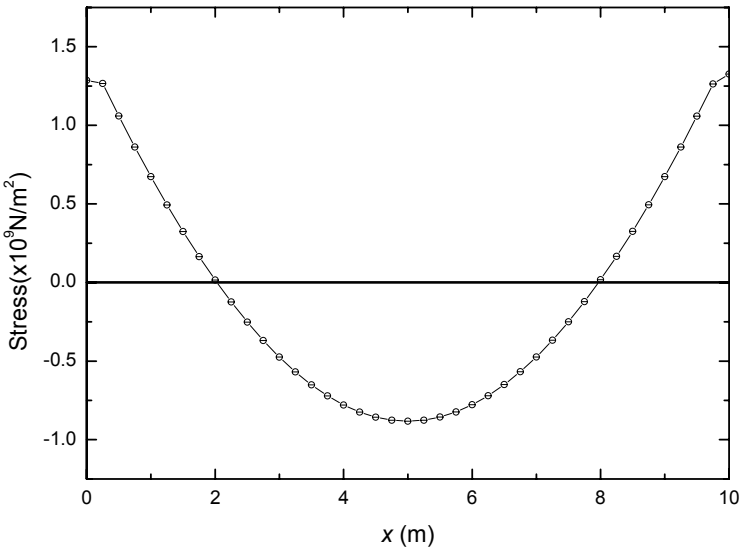

Figure 3.13 Distribution of the stress along the pipeline (when U_0=10m/s and D_0=0.7m).

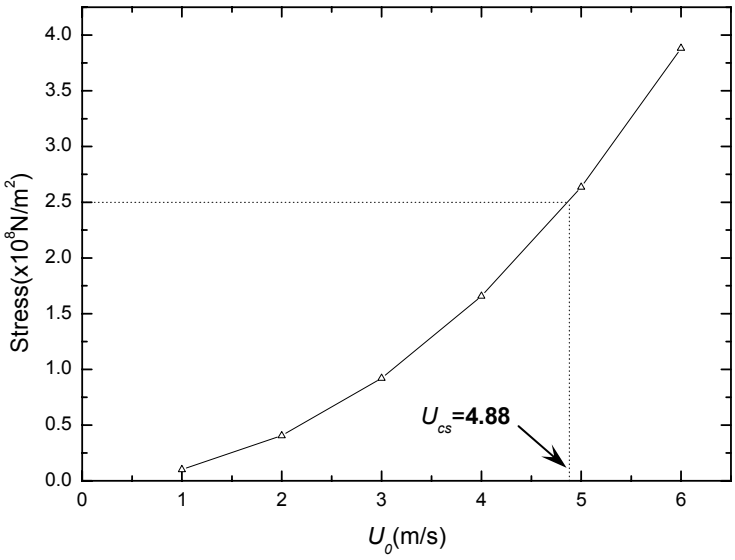

Figure 3.14(a) Critical velocities of strength failure (when D_0=0.7m).

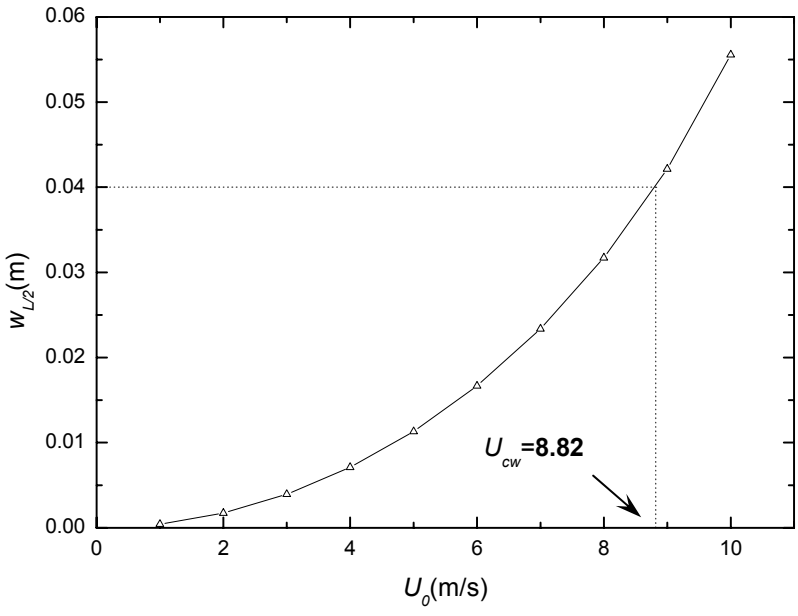

Figure 3.14(b) Critical velocities of deflection failure (when D_0=0.7m).

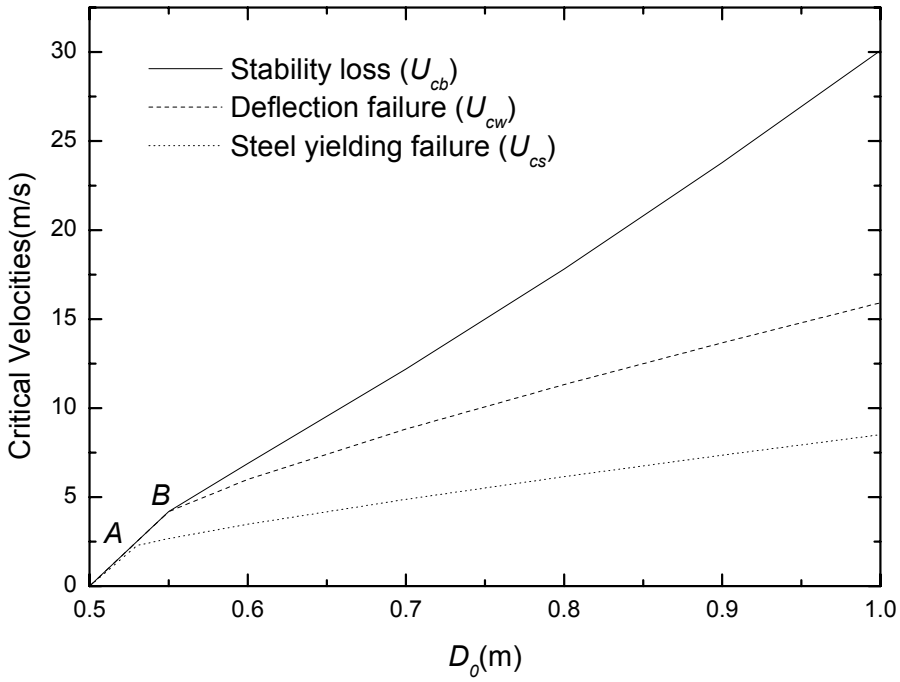

Figure 3.15 Comparison of distributions of respective critical velocities with respect to the gap D_0 in various failure patterns.

Chapter 4

One-dimensional Steady-State Simulations for Equilibrium of Electric-Sensitive Hydrogels

In this chapter, the simplified one-dimensional model of a hydrogel strip is firstly described. It is followed by the steady-state formulations of the reduced governing equations and corresponding discretizations. After validation of the developed MECe model by comparison with experiments, several studies of the physical parameters are carried out in detail.

4.1 A reduced 1-D study on hydrogel strip subject to applied electric field

As shown in Figure 4.1, a hydrogel strip is immersed into a bath solution subject to an externally applied electric field. With the coupling effects of the chemical and electric fields, the hydrogel strip is expected to bend towards either the cathode or anode direction, depending on the electric distribution of fixed-charges in hydrogels. It is noted that, in this dissertation, only the one-dimensional studies for hydrogels are made in both the steady-state and transient simulations. Thus only the deformation of hydrogels along the x direction is computed. It is also assumed that one of the middle points of hydrogel thickness b is fixed and its displacement is thus equal to zero. Further, although

the MECe model is applicable for the multi-electrolyte bath solution, this dissertation mainly focuses on the study associated with the simple solution consisting of two ionic species, such as NaCl solution.

4.2 Discretization of steady-state MECe governing equations

For the one-dimensional steady-state simulations, the reduced governing equations of the MECe model can be derived from Equations (2.79)-(2.82)

Convection-diffusion equations (2.79) for the ion concentration c^k *is reduced to*

$$\frac{\partial^2 \bar{c}^k}{\partial \bar{x}^2} + \alpha z^k \frac{\partial \bar{c}^k}{\partial \bar{x}} \frac{\partial \bar{\psi}}{\partial \bar{x}} + \alpha z^k \bar{c}^k \frac{\partial^2 \bar{\psi}}{\partial \bar{x}^2} = 0 \quad (k = +, -) \tag{4.1}$$

Poisson equation for the electric potential ψ

$$\frac{\partial^2 \bar{\psi}}{\partial \bar{x}^2} + \frac{F_c^2 L_{ref}^2 c_{ref}}{\varepsilon \varepsilon_0 RT\alpha} \left(\sum_{k=+,-} z^k \bar{c}^k + z^f \bar{c}^f \right) = 0 \tag{4.2}$$

Continuity equation of the mixture for the pressure p

$$\begin{aligned} \beta \left(\phi^w \frac{\partial^2 \bar{p}}{\partial \bar{x}^2} + 2 \frac{\partial \phi^w}{\partial \bar{x}} \frac{\partial \bar{p}}{\partial \bar{x}} \right) + \alpha \Bigg[2 \frac{\partial \phi^w}{\partial \bar{x}} \frac{\partial \bar{\psi}}{\partial \bar{x}} \sum_{k=+,-} z^k \bar{c}^k + \\ + \phi^w \left(\frac{\partial \bar{\psi}}{\partial \bar{x}} \sum_{k=+,-} \left(z^k \frac{\partial \bar{c}^k}{\partial \bar{x}} \right) + \frac{\partial^2 \bar{\psi}}{\partial \bar{x}^2} \sum_{k=+,-} z^k \bar{c}^k \right) \Bigg] = 0 \end{aligned} \tag{4.3}$$

in which $\Phi^+ = \Phi^- = 1$ is assumed for an ideal solution without chemical reaction, and the assumption $\boldsymbol{B}_w = 0$ is also adopted since its value is very small when $\boldsymbol{B}_w tr(\boldsymbol{E})$ is compared with the pressure *p*.

Momentum equation for the hydrogel displacement u

$$(3\lambda_s + 2\mu_s) \frac{\partial^2 \bar{u}}{\partial \bar{x}^2} - \beta RT c_{ref} \frac{\partial \bar{p}}{\partial \bar{x}} = 0 \tag{4.4}$$

where isotropic strain is assumed for the hydrogel strip, namely

$tr(\boldsymbol{E}) = 3e_{11} = 3(\partial u / \partial x)$ (Here e_{11} is the *x*-component of strain vector $\boldsymbol{E}$). With this assumption, the boundary condition (2.68) is simplified as

$$(3\lambda_s + 2\mu_s)\frac{\partial \overline{u}_{\text{interface}}}{\partial \overline{x}} = \beta RTc_{ref}\,\overline{p}_{\text{interface}} \tag{4.5}$$

In order to discretize the reduced governing equations, the discrete form of the variables are employed as

$$\overline{c}^k = \sum_{j=1}^{np} N_j(\overline{x}_i)\overline{c}_j^k - \sum_{m=1}^{np}(\overline{x} - \sum_{j=1}^{np} N_j(\overline{x}_i)\overline{x}_j)M_m(\overline{x}_i)\overline{c}_{xm} \tag{4.6}$$

$$\overline{\psi} = \sum_{j=1}^{np} N_j(\overline{x}_i)\overline{\psi}_j - \sum_{m=1}^{np}(\overline{x} - \sum_{j=1}^{np} N_j(\overline{x}_i)\overline{x}_j)M_m(\overline{x}_i)\overline{\psi}_{xm} \tag{4.7}$$

$$\overline{p} = \sum_{j=1}^{npGel} N_j(\overline{x}_i)\overline{p}_j - \sum_{m=1}^{npGel}(\overline{x} - \sum_{j=1}^{npGel} N_j(\overline{x}_i)\overline{x}_j)M_m(\overline{x}_i)\overline{p}_{xm} \tag{4.8}$$

$$\overline{u} = \sum_{j=1}^{npGel} N_j(\overline{x}_i)\overline{u}_j - \sum_{m=1}^{npGel}(\overline{x} - \sum_{j=1}^{npGel} N_j(\overline{x}_i)\overline{x}_j)M_m(\overline{x}_i)\overline{u}_{xm} \tag{4.9}$$

Based on the Hermite-Cloud method, the disretizations of the 1-D steady-state MECe governing equations and auxiliary conditions are obtained as follows

$$\begin{aligned}&\sum_{j=1}^{np} N_{xxj}(\overline{x}_i)\overline{c}_j^k + \alpha z^k[\sum_{m=1}^{np} M_m(\overline{x}_i)\overline{c}_{xm}^{\,k}][\sum_{m=1}^{np} M_m(\overline{x}_i)\overline{\psi}_{xm}] + \\ &+ \alpha z^k[\sum_{j=1}^{np} N_j(\overline{x}_i)\overline{c}_j^k - \sum_{m=1}^{np}(\overline{x}_i - \sum_{j=1}^{np} N_j(\overline{x}_i)\overline{x}_j)M_m(\overline{x}_i)\overline{c}_{xm}][\sum_{j=1}^{np} N_{xxj}(\overline{x}_i)\overline{\psi}_j] = 0\end{aligned} \tag{4.10}$$

$$\begin{aligned}&\sum_{j=1}^{np} N_{xxj}(\overline{x}_i)\overline{\psi}_j + \frac{F_c^2 L_{ref}^2 c_{ref}}{\varepsilon\varepsilon_0 RT\alpha}\{z^f\overline{c}^f + \sum_{k=+,-} z^k[\sum_{j=1}^{np} N_j(\overline{x}_i)\overline{c}_j^k - \\ &\qquad - \sum_{m=1}^{np}(\overline{x}_i - \sum_{j=1}^{np} N_j(\overline{x}_i)\overline{x}_j)M_m(\overline{x}_i)\overline{c}_{xm}]\} = 0\end{aligned} \tag{4.11}$$

$$(3\lambda_s + 2\mu_s)\sum_{j=1}^{npGel} N_{xxj}(\overline{x}_i)\overline{u}_j - \beta RTc_{ref}\sum_{m=1}^{npGel} M_m(\overline{x}_i)\overline{p}_{xm} = 0 \tag{4.12}$$

$$\begin{aligned}
&\beta[\phi^w \sum_{j=1}^{npGel} N_{xxj}(\bar{x}_i)\bar{p}_j + 2\frac{\partial \phi^w}{\partial \bar{x}} \sum_{m=1}^{npGel} M_m(\bar{x}_i)\bar{p}_{xm}] + \\
&+\alpha\{2\frac{\partial \phi^w}{\partial \bar{x}} \sum_{m=1}^{npGel} M_m(\bar{x}_i)\bar{\psi}_{xm}[\sum_{k=+,-} z^k \sum_{j=1}^{npGel}(N_j(\bar{x}_i)\bar{c}_j^k - \\
&-\sum_{m=1}^{npGel}(\bar{x}_i - \sum_{j=1}^{npGel} N_j(\bar{x}_i)\bar{x}_j)M_m(\bar{x}_i)\bar{c}_{xm})] + \\
&+\phi^w[\sum_{m=1}^{npGel} M_m(\bar{x}_i)\bar{\psi}_{xm}(\sum_{k=+,-} z^k \sum_{m=1}^{npGel} M_m(\bar{x}_i)\bar{c}_{xm}^k) + \\
&+\sum_{j=1}^{npGel} N_{xxj}(\bar{x}_i)\bar{\psi}_j \sum_{k=+,-} z^k \sum_{j=1}^{npGel}(N_j(\bar{x}_i)\bar{c}_j^k - \\
&-\sum_{m=1}^{npGel}(\bar{x}_i - \sum_{j=1}^{npGel} N_j(\bar{x}_i)\bar{x}_j)M_m(\bar{x}_i)\bar{c}_{xm})]\} = 0
\end{aligned} \tag{4.13}$$

$$\sum_{j=1}^{np} N_{xj}(\bar{x}_i)\bar{c}_j^k - [\sum_{j=1}^{np} N_{xj}(\bar{x}_i)\bar{x}_j]\sum_{m=1}^{np} M_m(\bar{x}_i)\bar{c}_{xm}^k = 0 \tag{4.14}$$

$$\sum_{j=1}^{np} N_{xj}(\bar{x}_i)\bar{\psi}_j - [\sum_{j=1}^{np} N_{xj}(\bar{x}_i)\bar{x}_j]\sum_{m=1}^{np} M_m(\bar{x}_i)\bar{\psi}_{xm} = 0 \tag{4.15}$$

$$\sum_{j=1}^{npGel} N_{xj}(\bar{x}_i)\bar{u}_j - [\sum_{j=1}^{npGel} N_{xj}(\bar{x}_i)\bar{x}_j]\sum_{m=1}^{npGel} M_m(\bar{x}_i)\bar{u}_{xm} = 0 \tag{4.16}$$

$$\sum_{j=1}^{npGel} N_{xj}(\bar{x}_i)\bar{p}_j - [\sum_{j=1}^{npGel} N_{xj}(\bar{x}_i)\bar{x}_j]\sum_{m=1}^{npGel} M_m(\bar{x}_i)\bar{p}_{xm} = 0 \tag{4.17}$$

where *np* is the number of scattered points in the whole domain covering the hydrogel and surrounding solution, and *npGel* is that within the hydrogel domain only.

4.3 Experimental comparison

To validate the presently developed MECe model, a simulation is carried out and the computed results are compared with the experimental data for a specified hydrogel strip with positive fixed charges (z^f=+1). The parameters used in the simulation are taken from experimental data (Zhou et al., 2002) as

R=9.648×10^4(J/mol·K), F=9.648×10^4(C/mol), T=278(K), $\phi_0^w = 0.8$, $\varepsilon = 80$, $\varepsilon_0 = 8.854\times10^{-12}(\mathrm{C^2/Nm^2})$, $3\lambda + 2\mu = 1.2\times10^5$(Pa), $c^* = 5.5(\mathrm{mol/m^3})$, c_0^f=20 (mol/ m^3), the 1-D computational domain L=20(mm), the thickness of hydrogel strip in the computing direction h=1(mm). The comparisons are presented in Figure 4.2, where the average curvature *Ka*, as a physical parameter measuring the extent of hydrogel deformation, is defined at the middle point of hydrogel thickness and $Ka = 2(e_1 - e_2)/(h(2 + e_1 + e_2))$ (e_1 and e_2 are the hydrogel strains at the two ends of the strip thickness). It is observed from Figure 4.2 that, with increasing applied voltage V_e, the average curvature *Ka* increases quasi-linearly. The simulated results agree well with the experimental data under 5 (V) applied electric field, in which their relative errors at V_e=1 and 3 (V) are 2.6% and 4.1%, respectively. However, they seem to have different trends above 5 (V), in which their relative errors at V_e=5, 7 and 9 (V) are 10.5%, 6.0% and 8.1%, respectively. The reasons may be that the bending deformation of the present electric-sensitive hydrogels depends directly on many parameters, including the voltage of applied electric field, electrolyte composition, fixed-charge, chemical reactions, temperature, heat conduction, ionic diffusion and convection. As a preliminary work with isotropy assumption, the influences of chemical reactions, heat conduction and temperature have not been included in the presently developed mathematical MECe model. The simplifications are feasible under low voltage (such as 5V) of the applied electric field. However, with the increase of the applied electric voltage, these nonlinear effects become more and more

significant and they should thus be considered. Probably, these are the main reasons for the different trends above 5V between the experimental data and the numerical results. Anyway, the present comparisons achieve very good agreements between the simulated results and experimental data.

4.4 Parameters studies

In the simulations for influences of physical parameters on the responsive behaviors of electric-sensitive hydrogels, the parameters used as input include T=298(K), F=9.648×10^4(C/mol), R=9.648×10^4(J/mol·K), $\phi_0^w = 0.8$, $\varepsilon = 80$, $3\lambda + 2\mu = 1.2\times10^5$(Pa), $\varepsilon_0 = 8.854\times10^{-12}$(C^2/Nm^2), $L = 1.5\times10^{-2}$(m) z^f =–1, and $h = 5\times10^{-3}$(m). As shown in Figure 4.3, a preliminary study is made before the parameter influences are discussed, where the distributions of ion concentrations and electric potential in both the hydrogel and exterior solution, and the displacement field of hydrogel strip are presented with $c^* = 1$(mol/m^3), $c_0^f = 10$(mol/m^3) and $V_e = 0.2$(V). It is observed from Figure 4.3(a) that, in the surrounding bath solution, the concentration of diffusive Na^+ is equal to that of the diffusive Cl^-. The ionic concentrations near the cathode increases with the distance away from the cathode while the ionic concentrations near the anode decreases with the distance away from the anode. However, within the hydrogel, there is a concentration difference between the diffusive Na^+ and Cl^- due to the effect of fixed-charge, and both the ion concentrations decrease with the distance away from the cathode. It is also noted that, on the hydrogel-solution interface,

there is an evident difference between the ionic concentrations in the interior of the hydrogels and the surrounding solution, which results in the pressure to drive the hydrogels deform. In Figure 4.3(b), it is seen that, due to the influence of the fixed-charge groups, the distribution of electric potential is no longer linear in the whole computational domain, which collapses within the hydrogel domain. Due to the higher conductivity of the mobile ions within the hydrogels, the gradient of electric potential distributed in the hydrogels is smaller than that in the surrounding solution, which is compensated by a smaller step of the distributed electric potential on hydrogel-solution interface near the cathode in comparison with that near the anode. These simulated results are in a good agreement with the FEM results completed by Wallmersperger et al. (2001). In Figure 4.3(c), it is shown that the hydrogel displacement increases with the coordinate x, and it results from the non-uniform distributions of ionic concentrations and electric potential.

4.4.1 Influence of external electric field

In the present study on the electric-sensitive hydrogel, the influence of external electric field on the responsive behaviors of the hydrogels is discussed in this section. Figure 4.4 shows the influences on the distributions of ionic concentrations, electric potential and hydrogel displacement, and Figures 4.5 to 4.7 show the influences on the variations of the average curvature Ka with various physical parameters including the fixed-charge density c_0^f, bath solution

concentration c^* and hydrogel strip thickness h.

In Figures 4.4(a) and (b), $c_0^f = 2(\text{mol/m}^3)$, $c^* = 1(\text{mol/m}^3)$, and $V_e = 0.02$, 0.04, 0.08, 0.16(V), with ψ=+0.01, +0.02, +0.04 and +0.08(V) at the anode, ψ=–0.01, –0.02, -0.04 and –0.08(V) at the cathode respectively. It is observed from the figure that, with the increment of the applied voltage V_e, the variations of Na^+ and Cl^- concentrations on the hydrogel-solution interface near the anode are always smaller than those near the cathode, and the distributed gradients of Na^+ and Cl^- concentrations within the hydrogels increase. Figure 4.4(c) shows that, when the applied voltage increases, the gradient of distributed electric potential increases in both the hydrogels and surrounding solution. Figure 4.4(d) demonstrates that, with the increase of applied voltage, the ionic concentration difference on the hydrogel-solution interface increases, and the hydrogel displacement increases as well.

Figure 4.5 presents the influence of the externally applied electric field V_e on the variation of average curvature Ka with the fixed-charge density c_0^f, where c^*=1(mol/m^3), V_e=0.02, 0.1 and 0.2(V), respectively. It is seen that, for a given applied voltage V_e, the average curvature Ka increases with the fixed-charge density c_0^f. The presently simulated phenomena are validated by the experiment (Homma et al., 2000). Furthermore, in order to investigate the influence of the externally applied electric field V_e on the variation of average curvature Ka with the bath solution concentration c^*, Figure 4.6 is depicted when $c_0^f = 10\,(\text{mol/m}^3)$, and V_e=0.02, 0.1 and 0.2(V), respectively. It is observed that an optimal c^* value

appears when the hydrogel strip reaches the largest bending deformation. This means, when the bath solution concentration c^* is larger than the computed optimal value, the bending deformation of hydrogel strip decreases with increasing c^*. The present simulations agree well with the experimental phenomena (Homma et al., 2000, 2001; Sun et al, 2001; Fei et al., 2002).

Figure 4.7 shows the relation between the average curvature *Ka* and the thickness *h* of hydrogel strip under various externally applied electric fields, V_e=0.02, 0.1 and 0.2(V) respectively, where $c_o^f = 10\,(\text{mol/m}^3)$ and c^*=1(mol/m^3). It is predicted that the average curvature *Ka* of the hydrogel strip decreases rapidly with increasing the strip thickness *h*, which is in consistence with the experiment (Homma et al., 2000, 2001).

4.4.2 Influence of fixed-charge density

For the ionized hydrogels with capability of responding to electric stimulus, the fixed-charge density has significant influences on the responsive behavior of the hydrogels subject to externally applied electric field. Figure 4.8 demonstrates the influence of fixed-charge density c_0^f on the distributions of diffusive ionic concentrations, electric potential and hydrogel displacement, where $c^* = 1(\text{mol/m}^3)$, $V_e = 0.2(\text{V})$ and $c_0^f = 2,\ 4,\ 8(\text{mol/m}^3)$ respectively. It is illustrated in Figure 4.8(a) that the ionic Na^+ concentration within the hydrogels increases with the fixed-charge density c_0^f. This phenomenon results from that the present anion fixed-charge groups ($z^f = -1$) attached on the polymeric network

chains of the hydrogels attract the mobile cations Na^+ to compensate the electric potential. Furthermore, it is seen from the Figure 4.8(b) that, the influence of the fixed-charge density c_0^f on the distribution of Cl^- concentration is relatively small due to the anion fixed-charge groups. Figure 4.8(c) is plotted for the c_0^f effect on the distributed electric potential. With the increase of fixed-charge density c_0^f, the more mobile ions diffuse into the hydrogels, the higher conductivity the hydrogels achieve. This results in the smaller gradient of electric potential distributed in hydrogels, compared with that in the surrounding solution. Figure 4.8(d) indicates that, with the increase of fixed-charge density c_0^f, the ionic concentration difference increases on the solution-hydrogel interfaces, which leads to the larger deformation of the hydrogels.

Figure 4.9 is presented to study the mechanical deformation of the hydrogel strip with h=5×10^{-3}(m) and c^*=1(mol/m^3), where the variations of the average curvature Ka against the externally applied electric field V_e are illustrated for different fixed-charge densities c_0^f=1, 5 and 10(mol/m^3). It is observed that, with the increase of the externally applied electric voltage V_e, the differences of both ionic concentrations and electric potential increase between the hydrogel strip and the surrounding bath solution. As such, the average curvature Ka increases rapidly with the applied electric voltage, and the bending deformation becomes larger, which are in a good match with the experimental phenomena (Homma et al., 2000; Sun et al, 2001; Fei et al., 2002).

4.4.3 Influence of concentrations of bath solution

The effect of bath solution concentration c^* on the distributions of diffusive ionic concentrations, electric potential and hydrogel displacement are shown in Figure 4.10, where $c_0^f = 2(\text{mol/m}^3)$, $V_e = 0.2(\text{V})$ and $c^* = 1, 2, 4, 8(\text{mol/m}^3)$, respectively. Figures 4.10(a) and 4.10(b) show that the increment of bath solution concentration c^* makes the diffusive Na^+ and Cl^- concentrations increase in both the hydrogels and surrounding solution. It is also found in Figure 4.10(c) that, when the bath solution concentration c^* reaches a certain value much larger than the fixed-charge density c_0^f, the concentration change of diffusive ions due to the attractive effect of fixed-charge may be neglected if compared with the distribution of bath solution concentration c^*. Then the conductivity of hydrogels is almost equal to that of surrounding solutions, which makes the electric potential quasi-linearly distribute in whole computational domain. In Figure 4.10(d), it is observed that, with the increase of c^*, the ionic concentration difference on the hydrogel-solution interfaces decreases, and then the hydrogel displacement decreases as well.

4.4.4 Influence of ionic valences

Figure 4.11 is plotted for discussion of the effect on ionic valence z_k on the distributions of ionic concentrations, electric potential and hydrogel displacement, where $c_0^f = 2(\text{mol/m}^3)$, $c^* = 1(\text{mol/m}^3)$, $V_e = 0.2(\text{V})$ and $|z_k| = 1, 2, 3$ respectively. It is observed from Figure 4.11(a) that, when the ionic valence $|z_k|$

increases, the cation concentration decreases clearly within the hydrogels. The corresponding concentration distribution in the surrounding solution has an obvious variation near the anode while there is little variation near the cathode. Figure 4.11(b) shows that, with increasing $|z_k|$, the corresponding anion concentration within the hydrogels grows. In the surrounding solutions, the distribution of anion concentration is almost equal to that of cation concentration. It is also found from Figures 4.11(c) and (d) that, when $|z_k|$ varies from 1 to 2, the changes of the electric potential and hydrogel displacement are much more distinct than those when $|z_k|$ varies from 2 to 3.

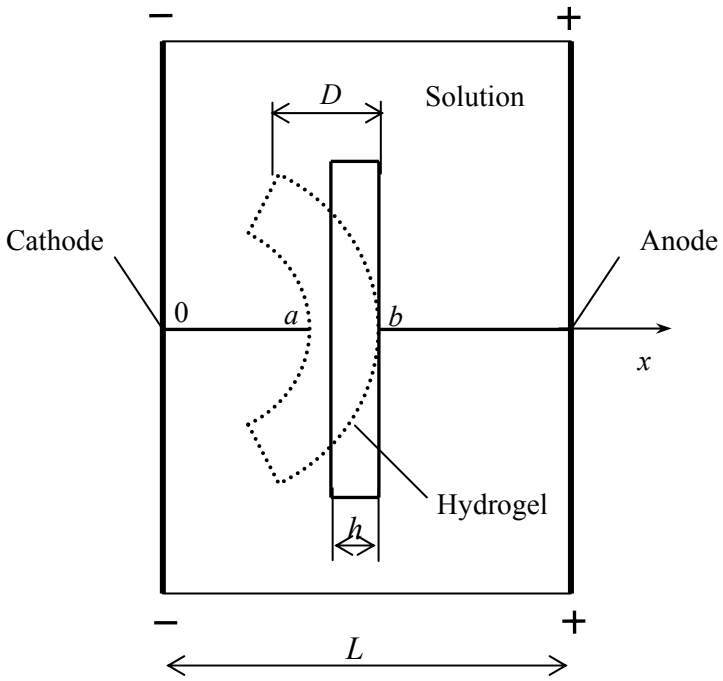

Figure 4.1 Schematic diagram of a hydrogel strip immersed in a bath solution under an externally applied electric field.

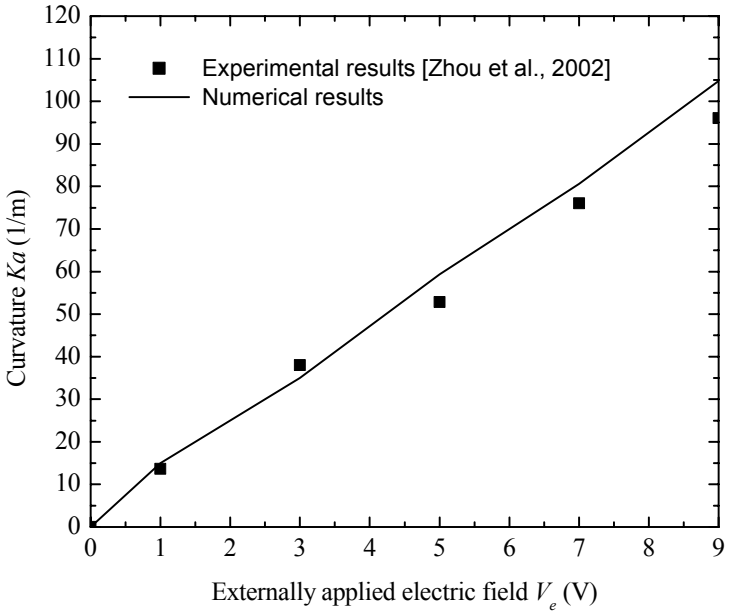

Figure 4.2 Comparison of numerically simulated results with experimental data.

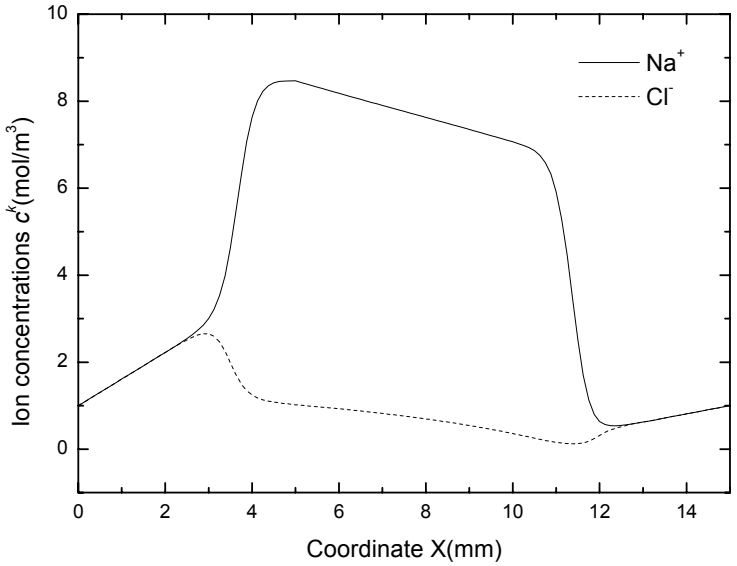

Figure 4.3(a) Distribution of ion concentrations.

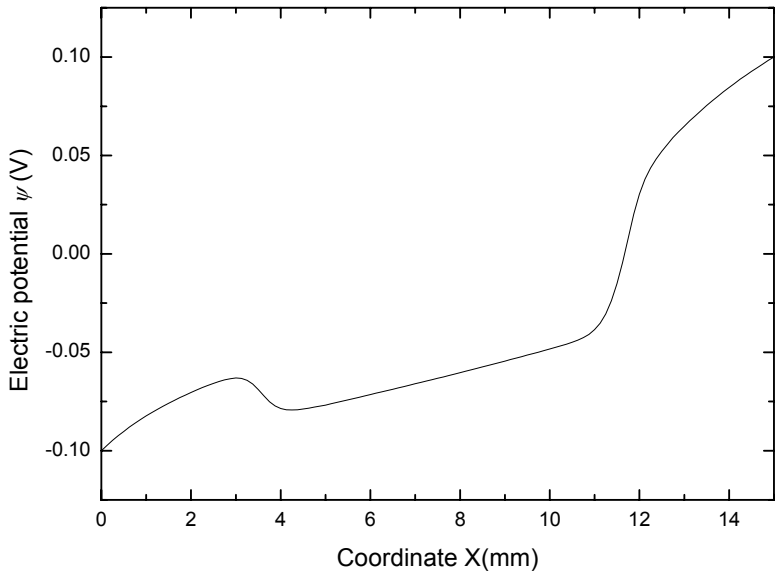

Figure 4.3(b) Distribution of electric potential.

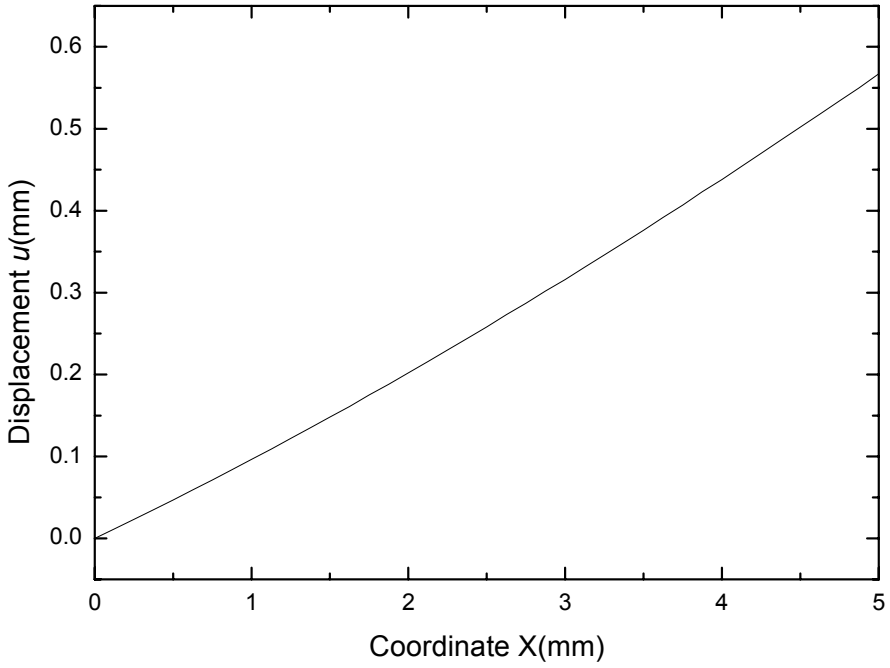

Figure 4.3(c) Distribution of hydrogel displacement.

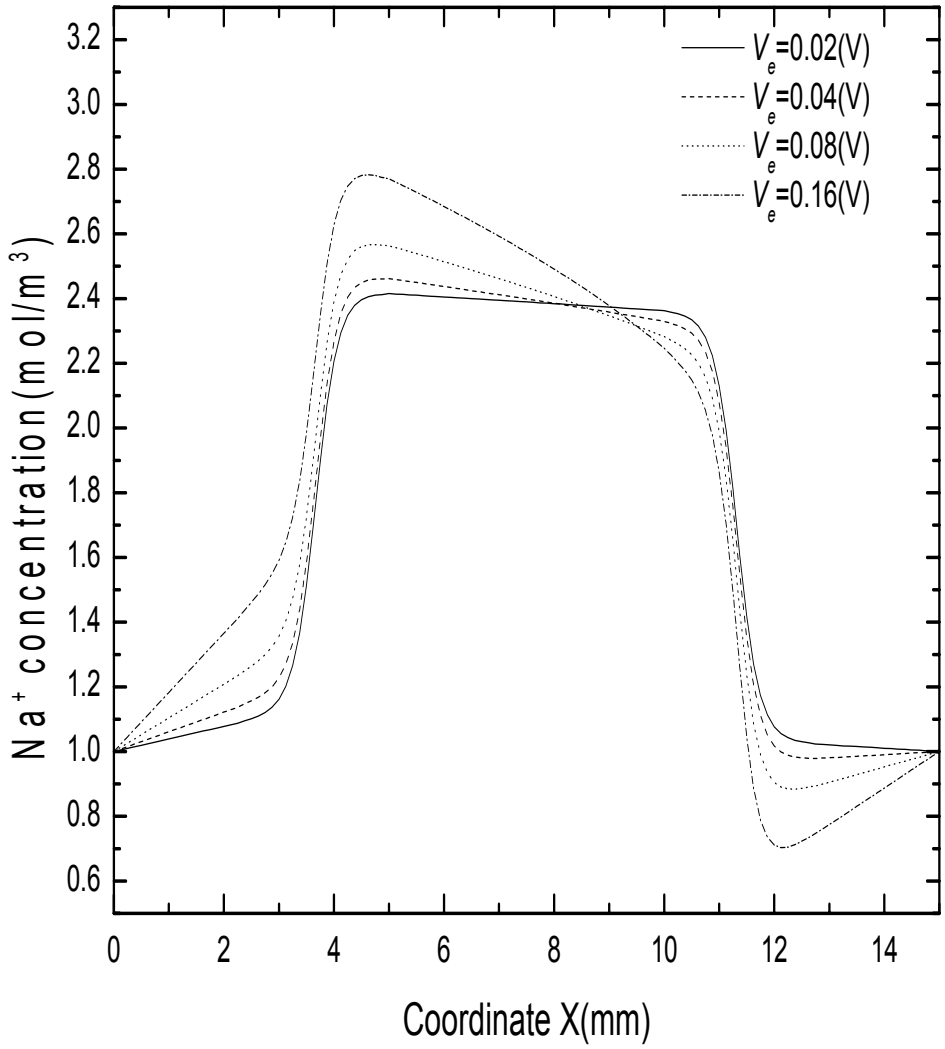

Figure 4.4(a) Effect of externally applied electric field on the variation of Na^+ concentration.

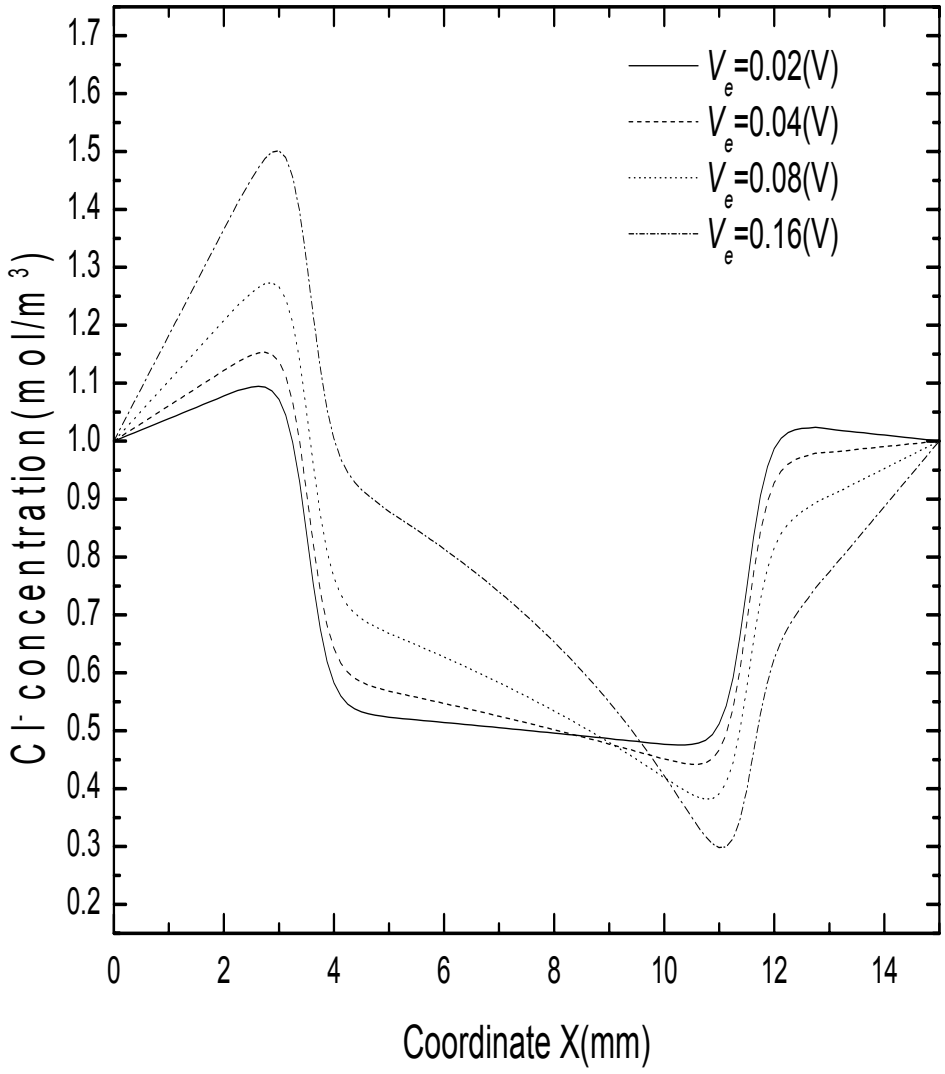

Figure 4.4(b) Effect of externally applied electric field on the variation of Cl^- concentration.

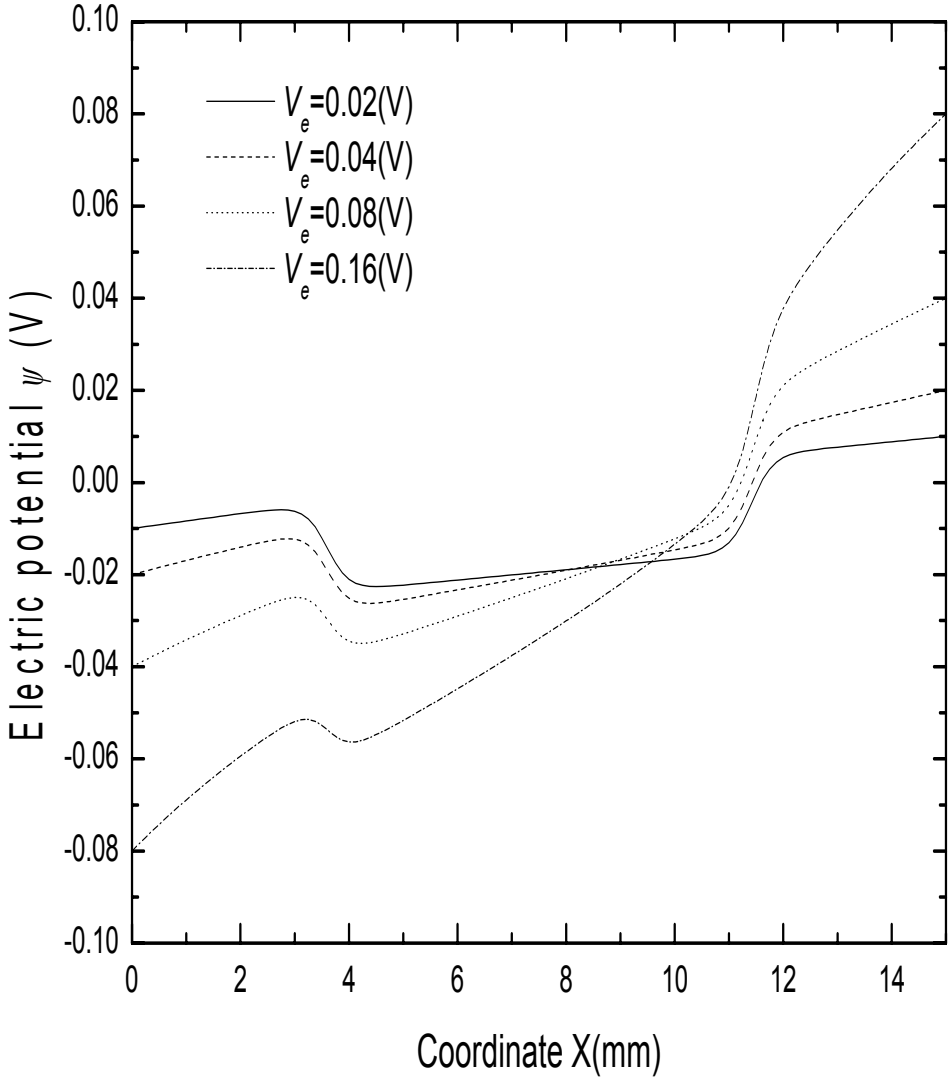

Figure 4.4(c) Effect of externally applied electric field on the variation of electric potential.

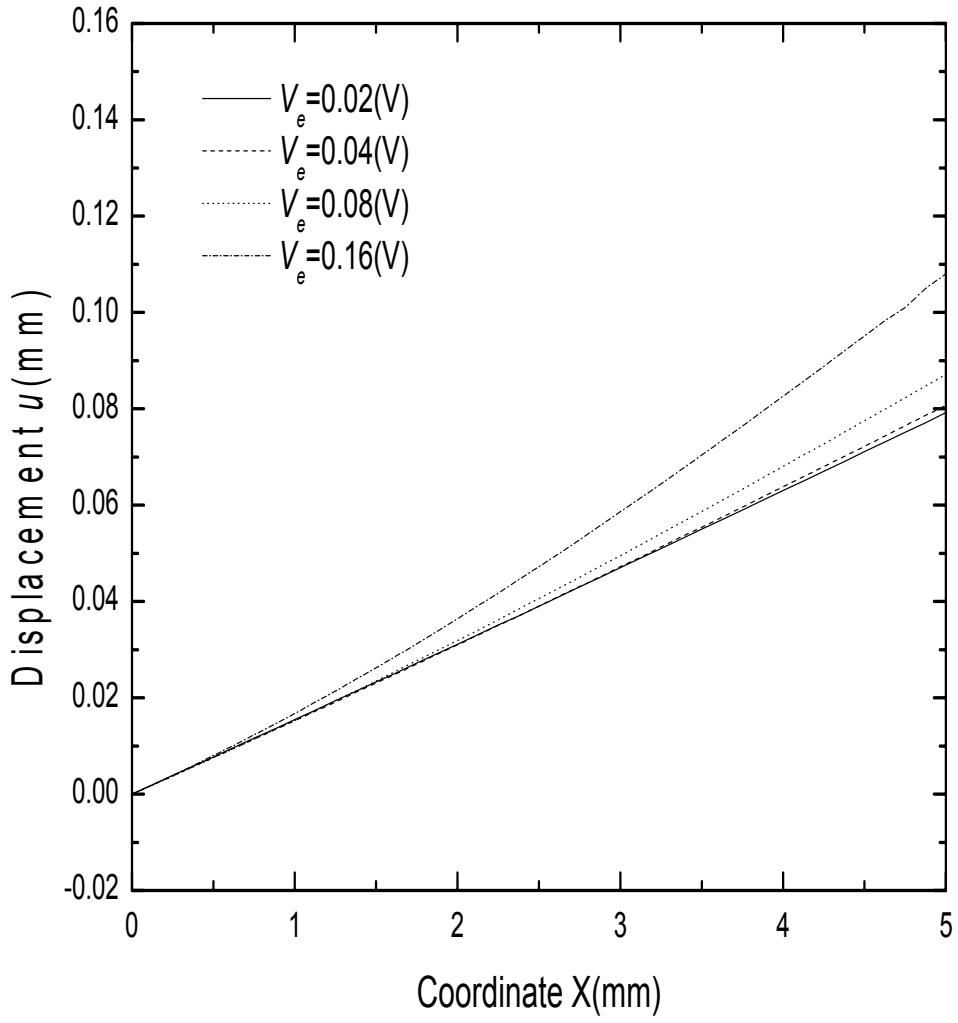

Figure 4.4(d) Effect of externally applied electric field on the variation of displacement.

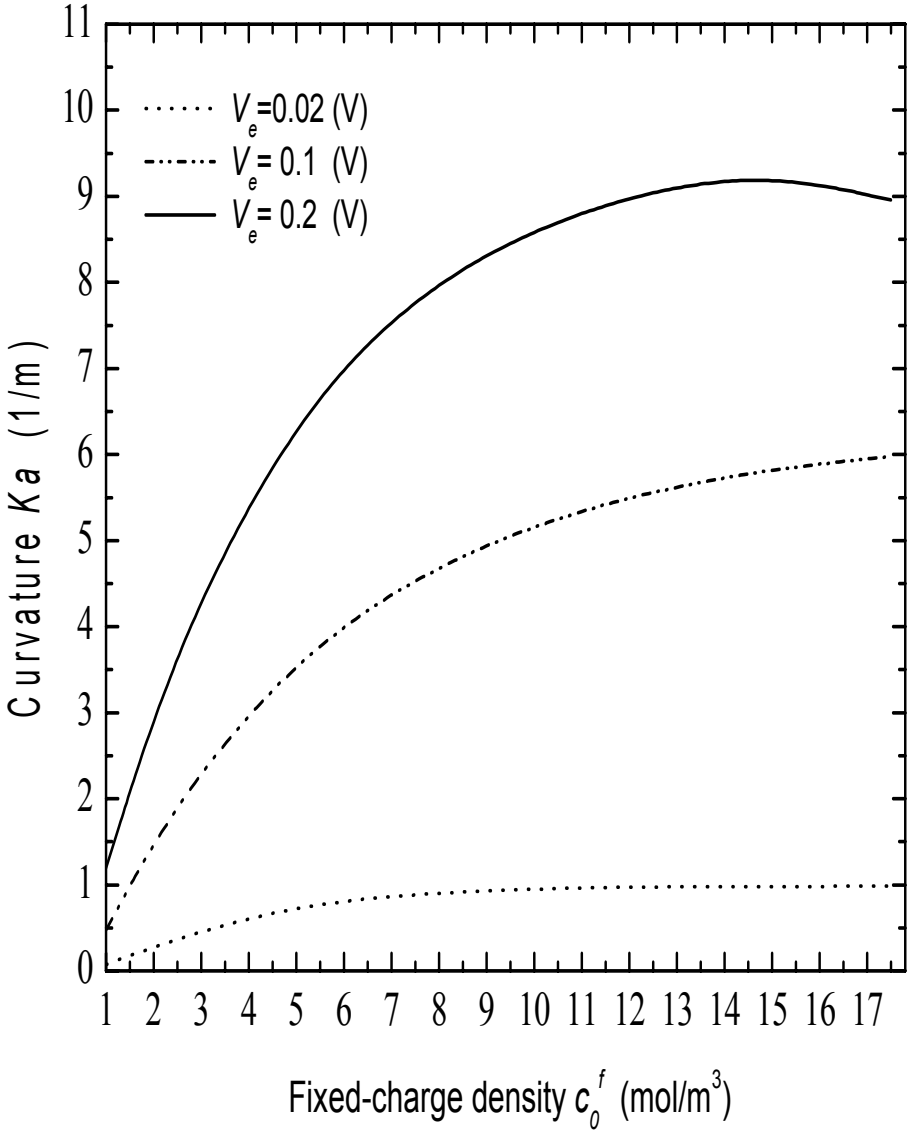

Figure 4.5 Effect of externally applied electric field on the variation of average curvature *Ka* against fixed charge density.

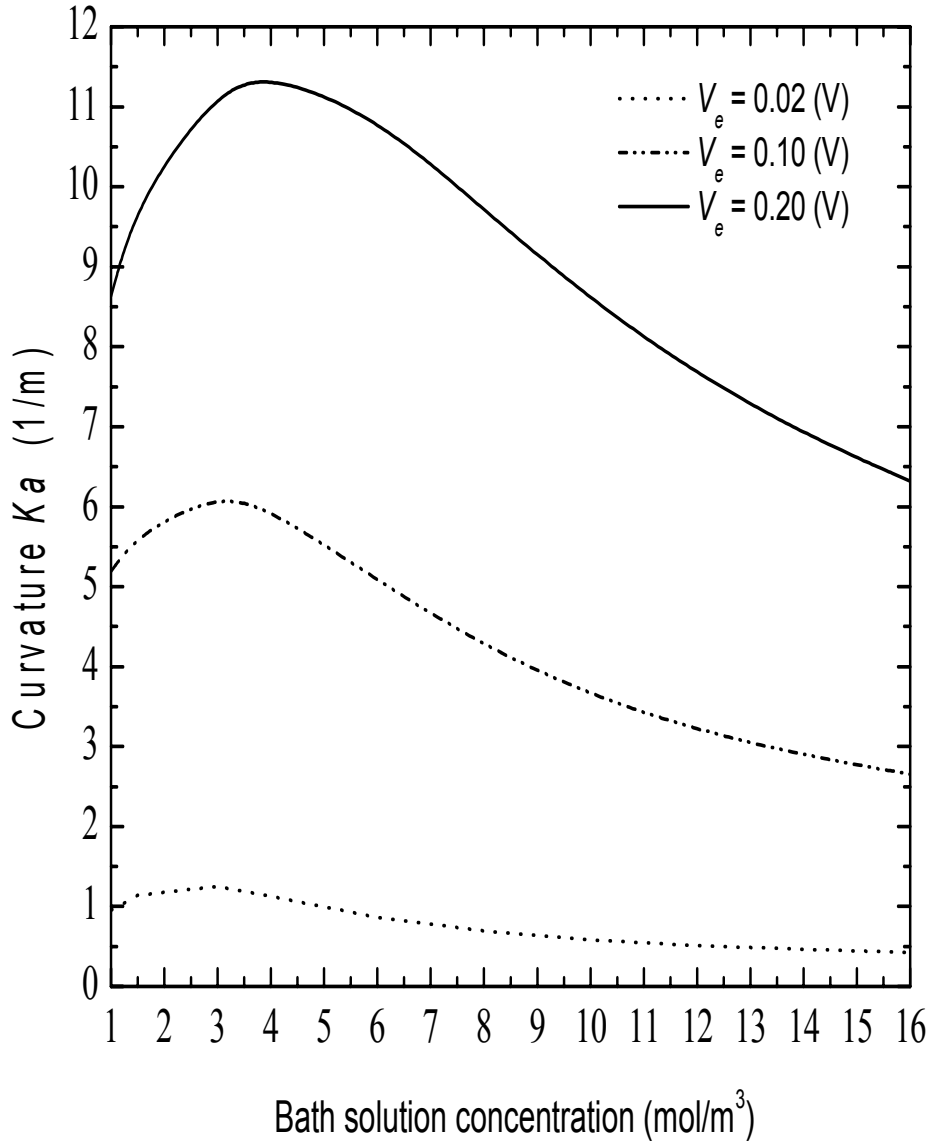

Figure 4.6 Effect of externally applied electric field on the variation of average curvature *Ka* against bath solution concentration.

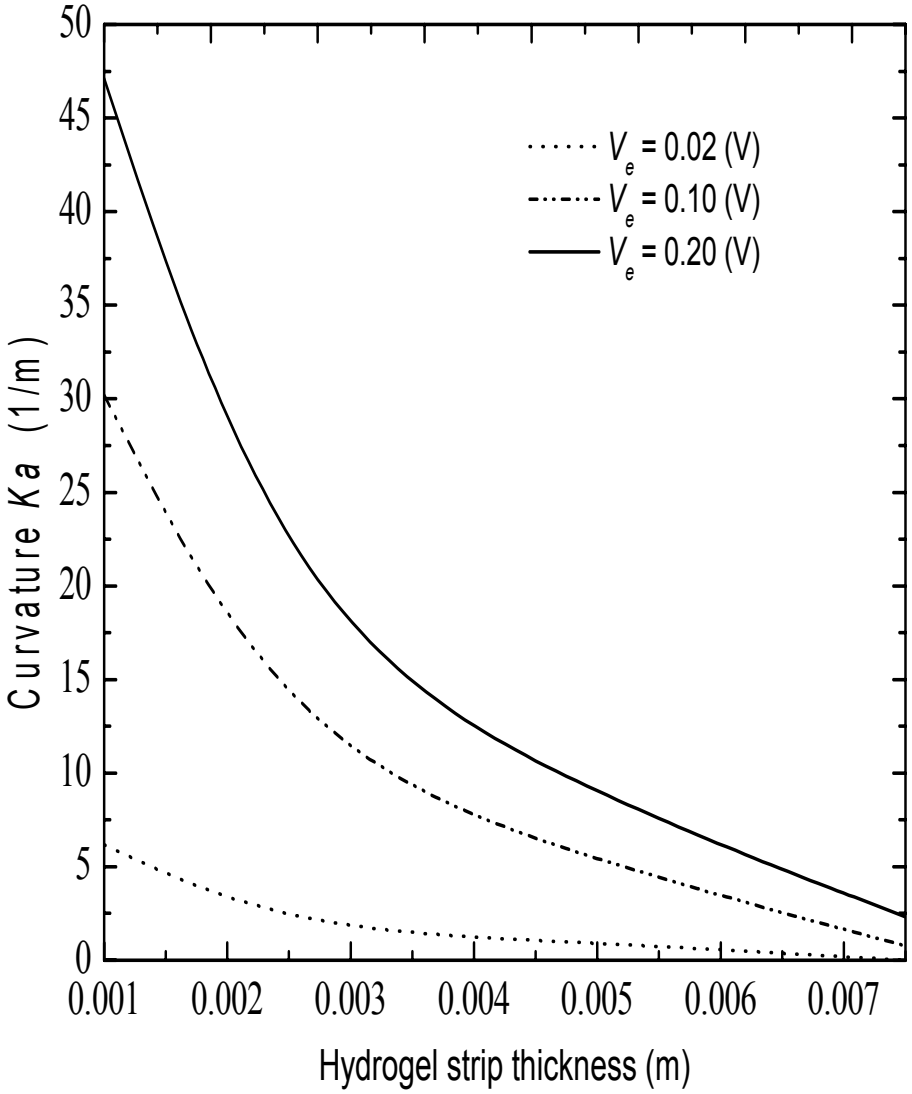

Figure 4.7 Effect of externally applied electric field on the variation of average curvature *Ka* against the thickness of hydrogel strip.

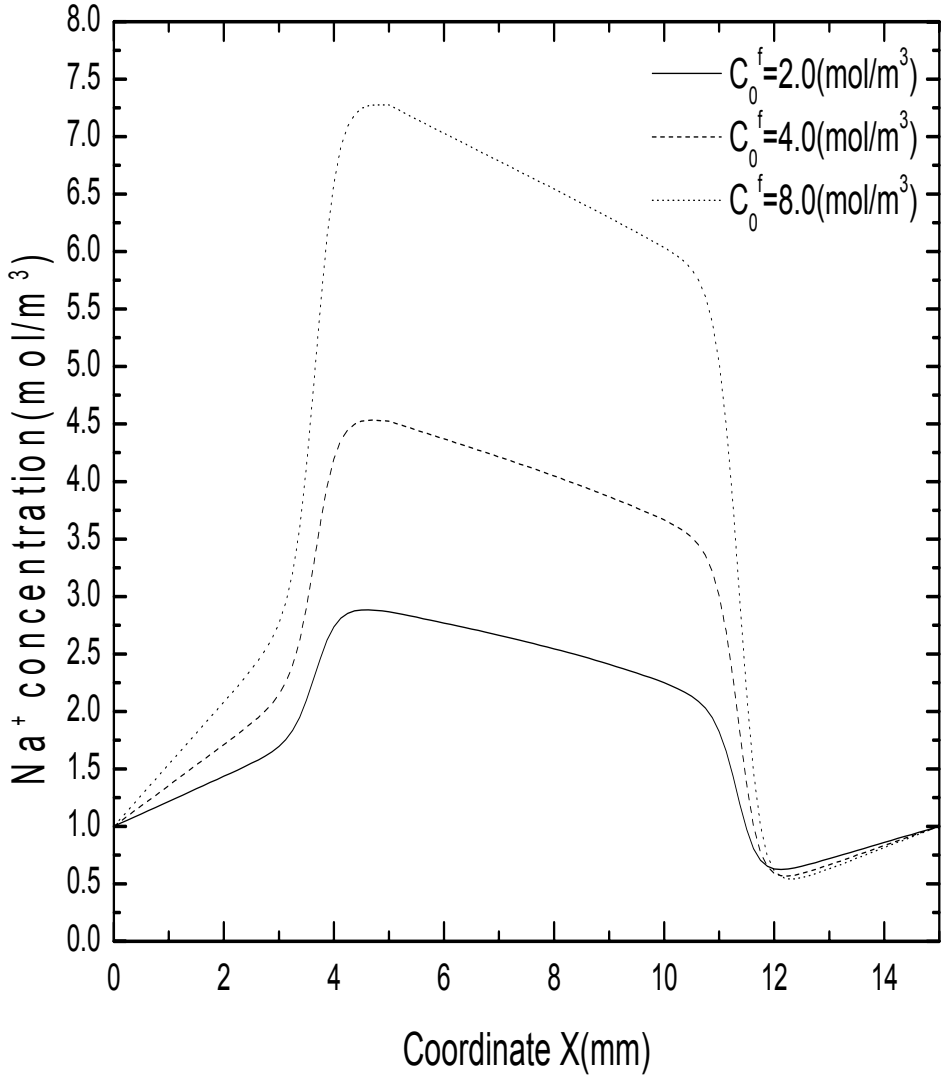

Figure 4.8(a) Effect of fixed charge density on the variation of Na^+ concentration.

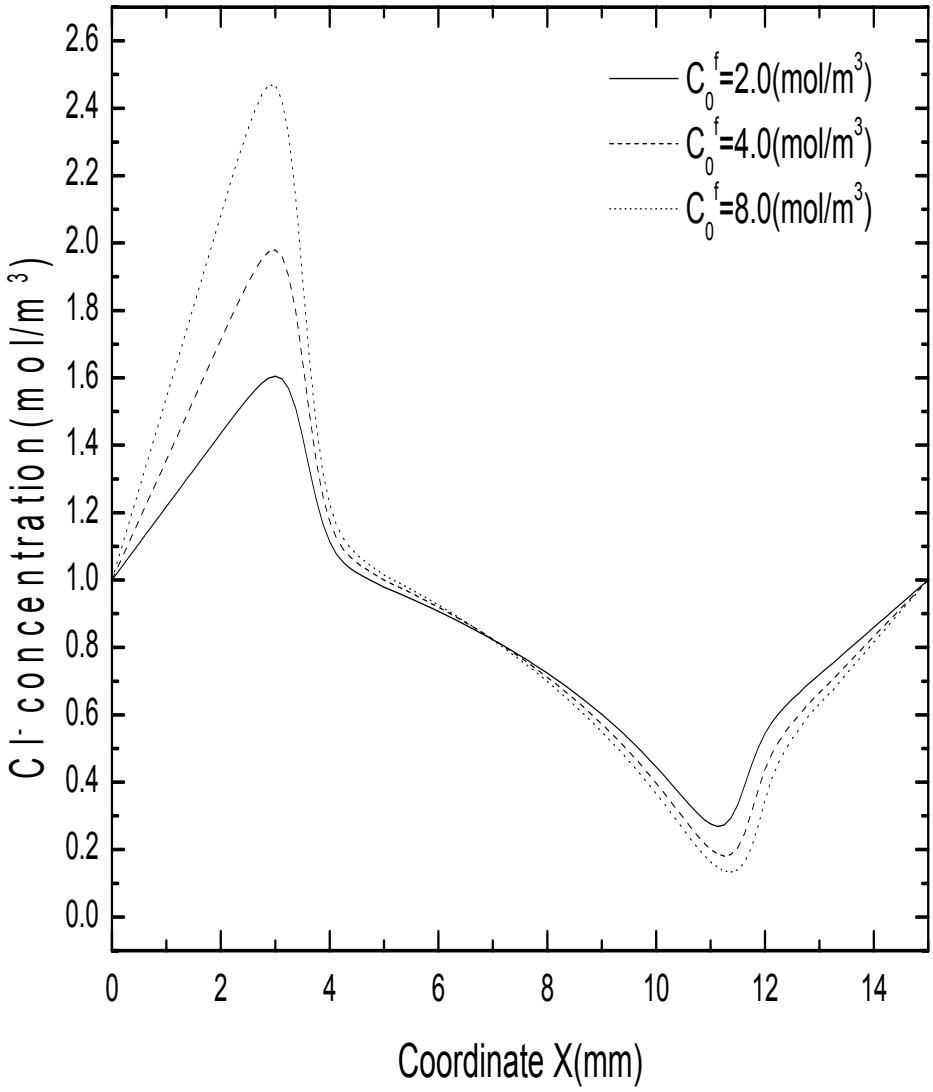

Figure 4.8(b) Effect of fixed charge density on the variation of Cl^- concentration.

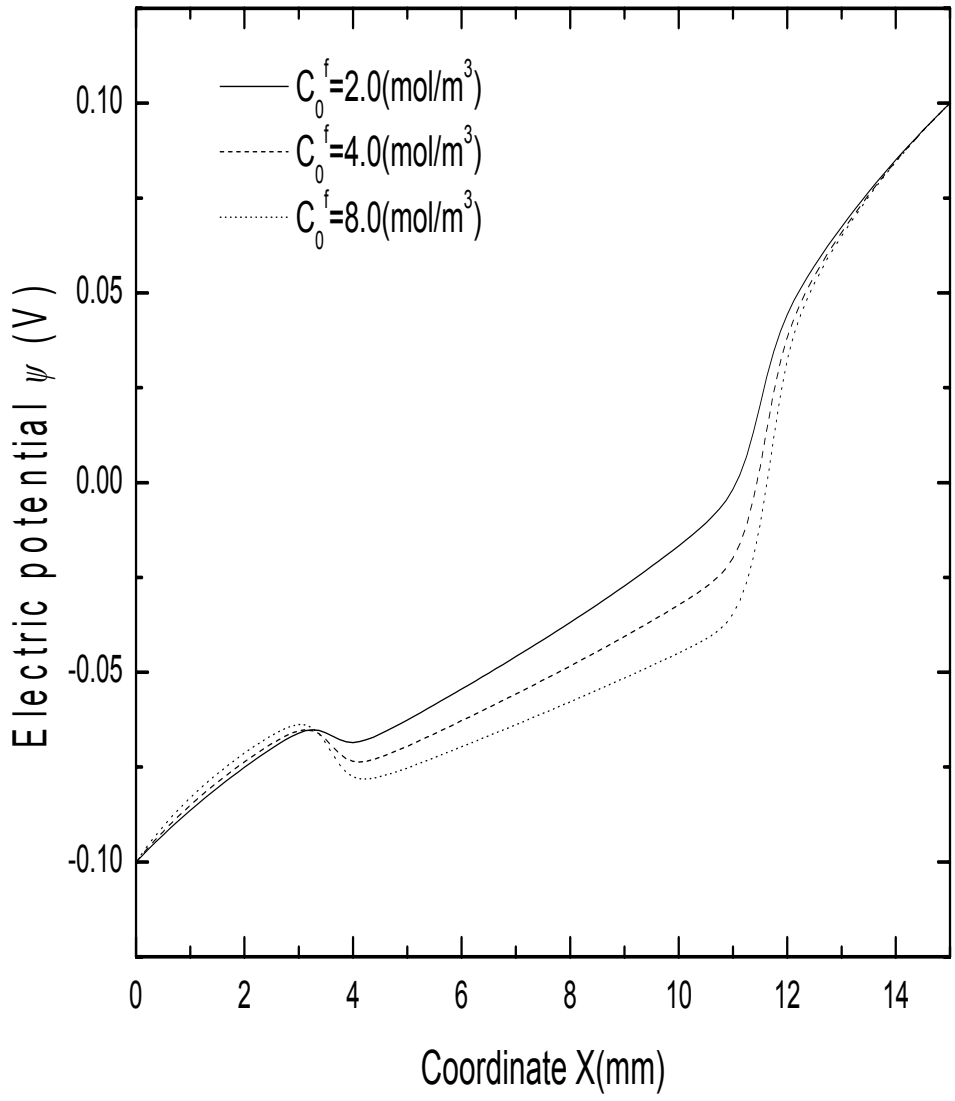

Figure 4.8(c) Effect of fixed charge density on the variation of electric potential

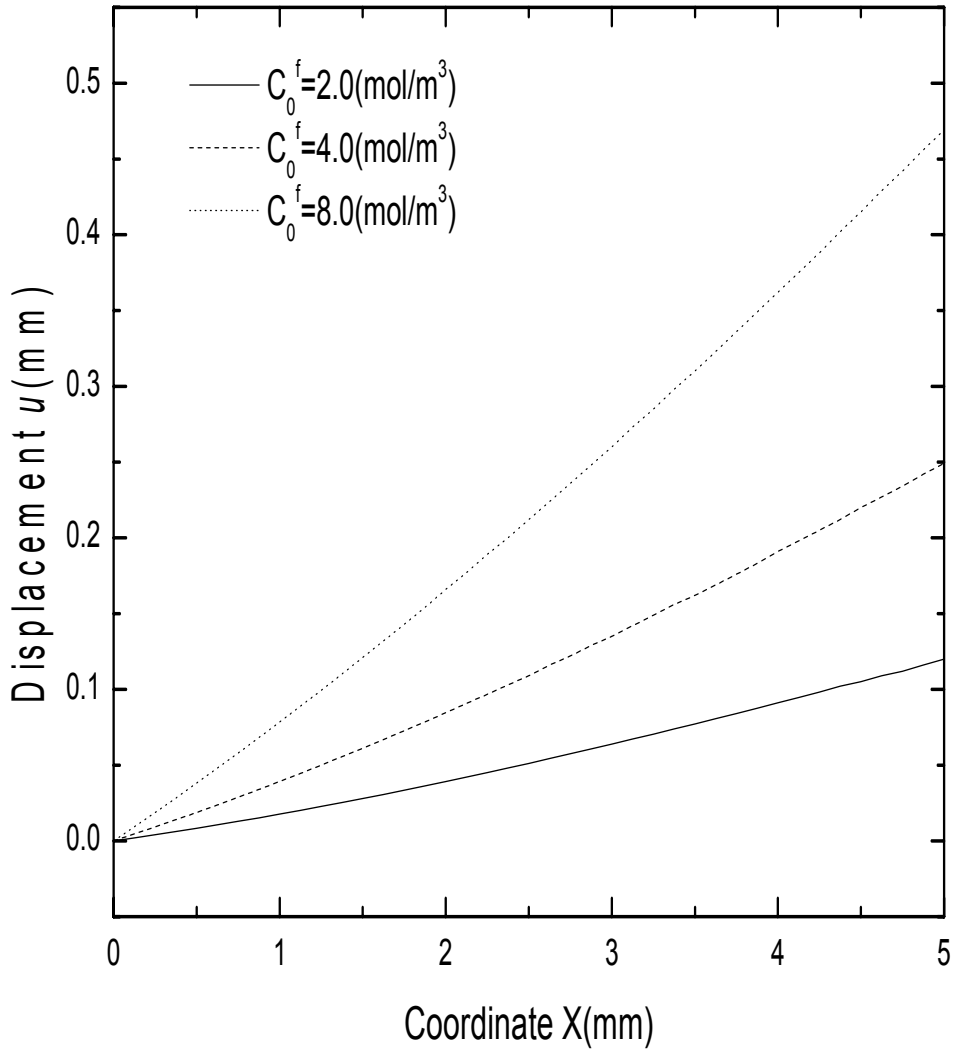

Figure 4.8(d) Effect of fixed charge density on the variation of displacement.

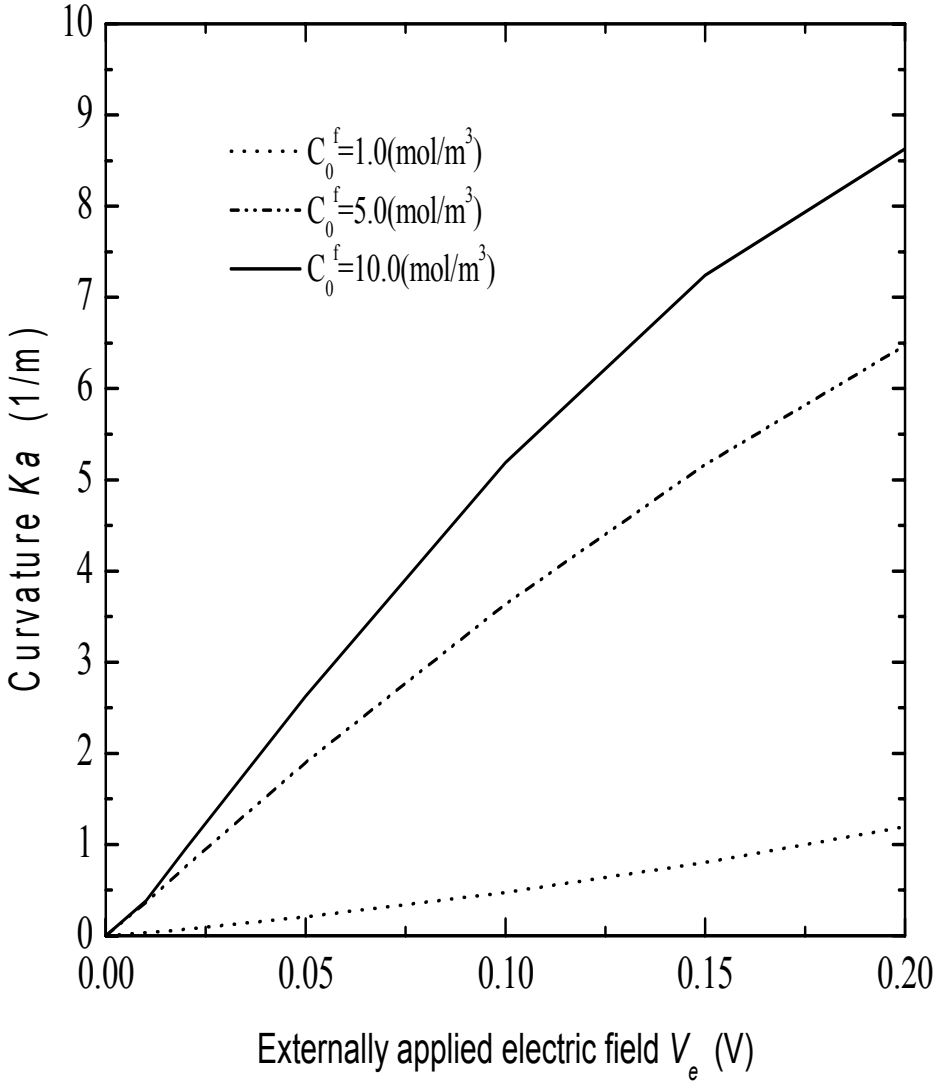

Figure 4.9 Effect of fixed charge on the variation of average curvature *Ka* against externally applied electric field.

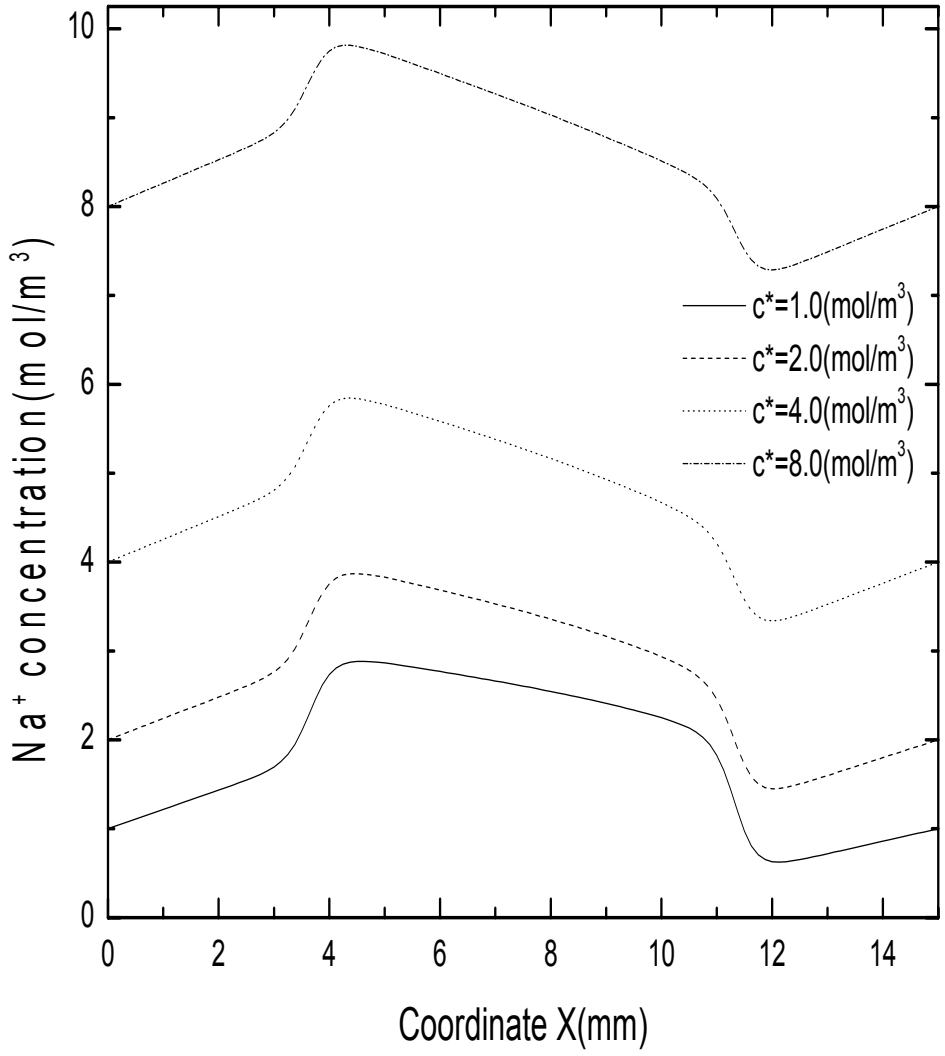

Figure 4.10(a) Effect of exterior solution concentration on the variation of Na^+ concentration.

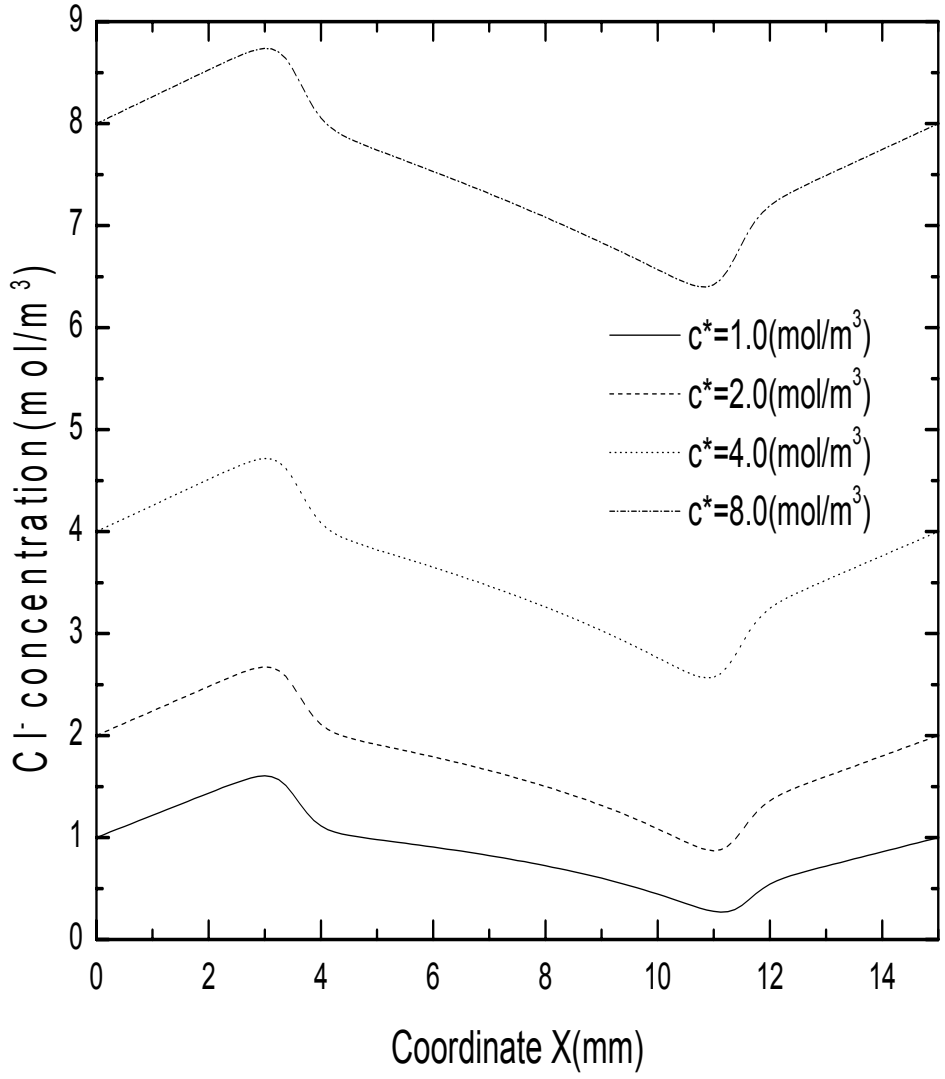

Figure 4.10(b) Effect of exterior solution concentration on the variation of Cl^- concentration.

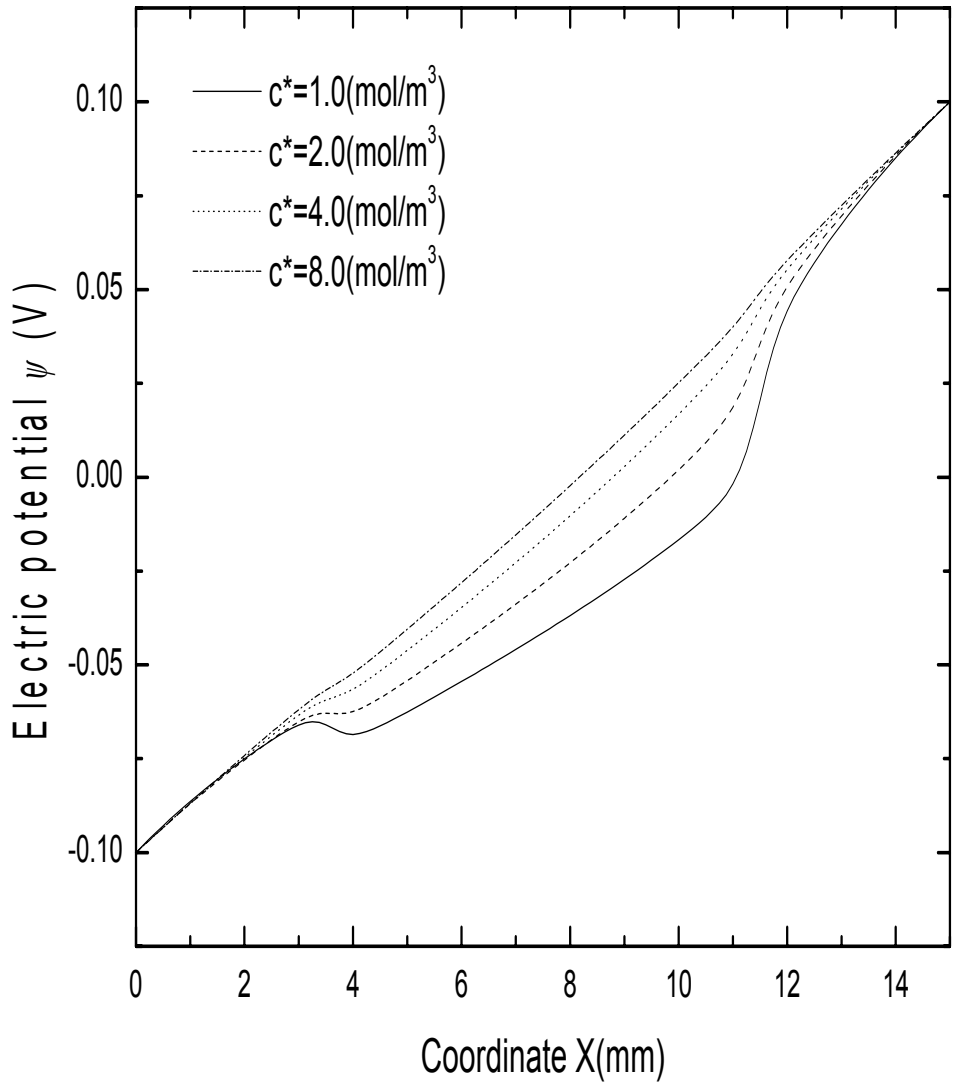

Figure 4.10(c) Effect of exterior solution concentration on the variation of electric potential.

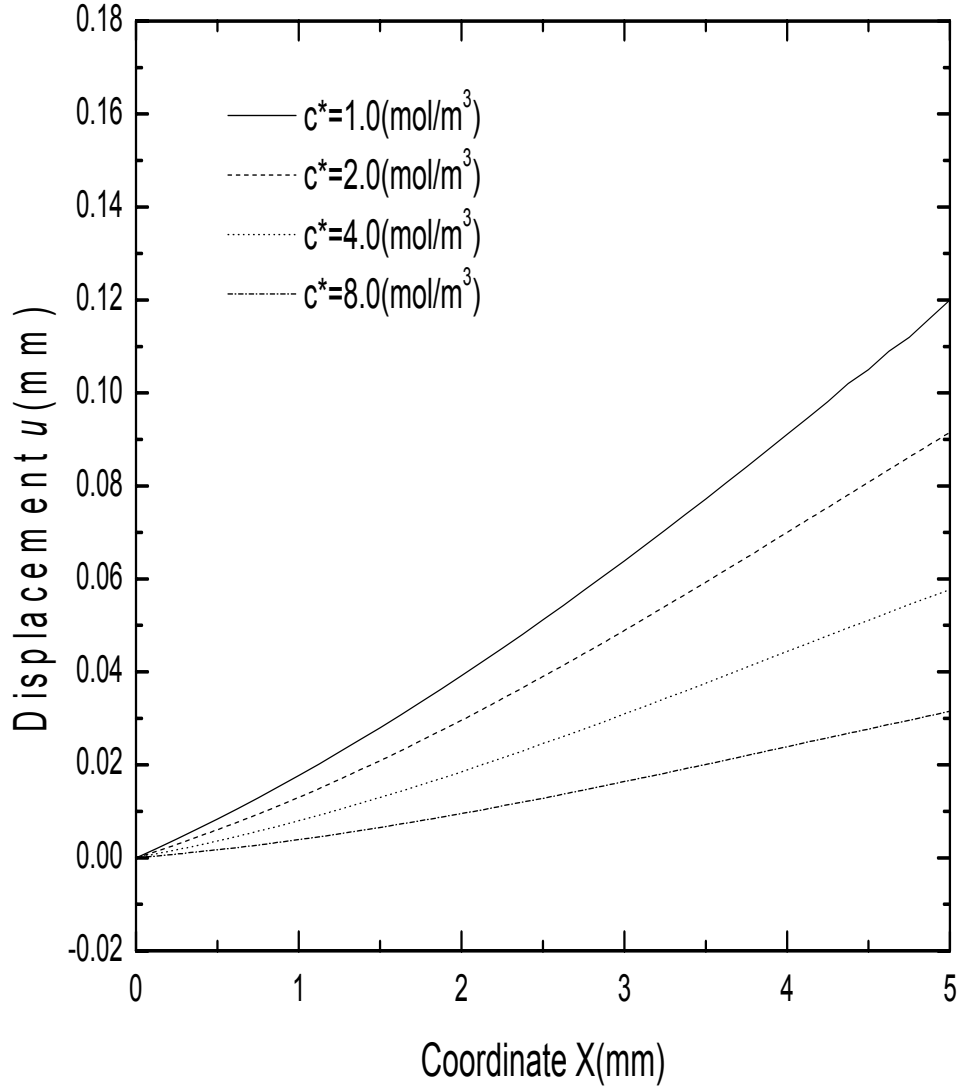

Figure 4.10(d) Effect of exterior solution concentration on the variation of displacement.

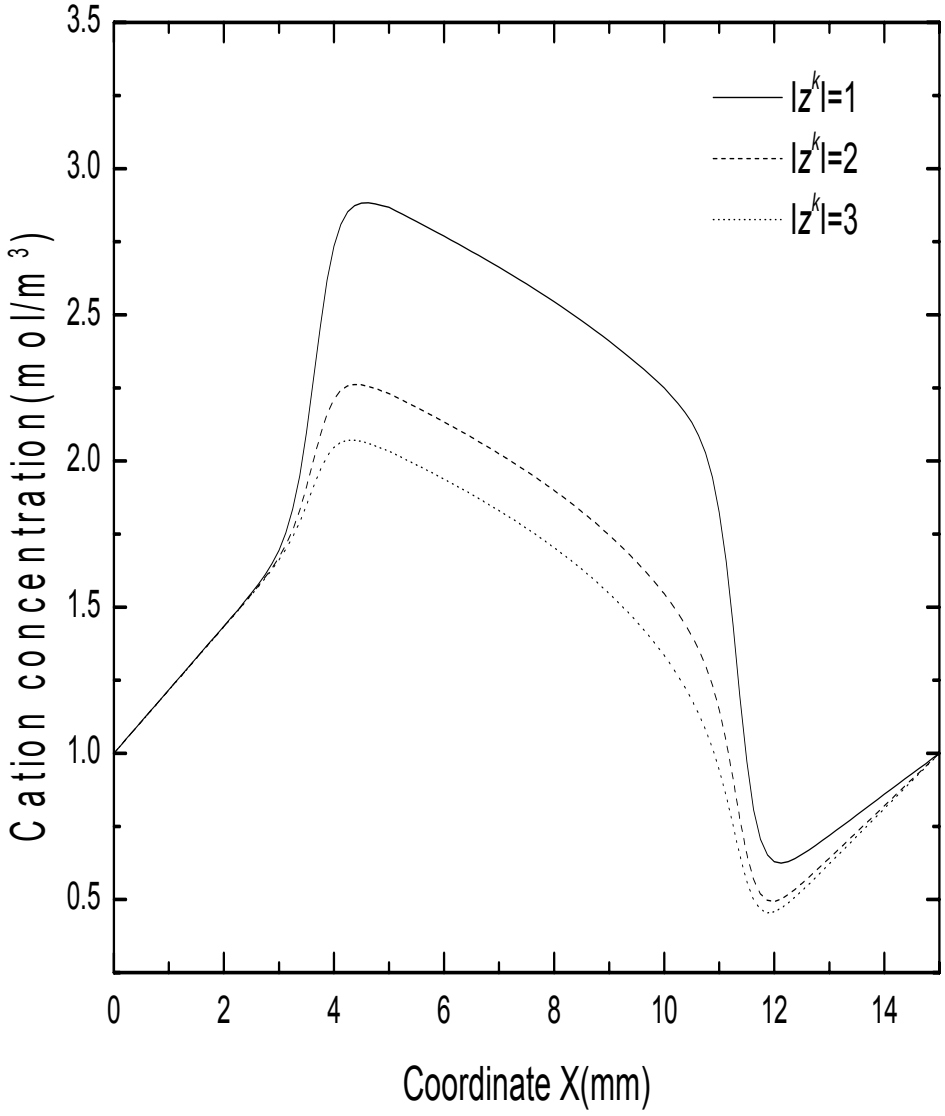

Figure 4.11(a) Effect of valence on the variation of cation concentration.

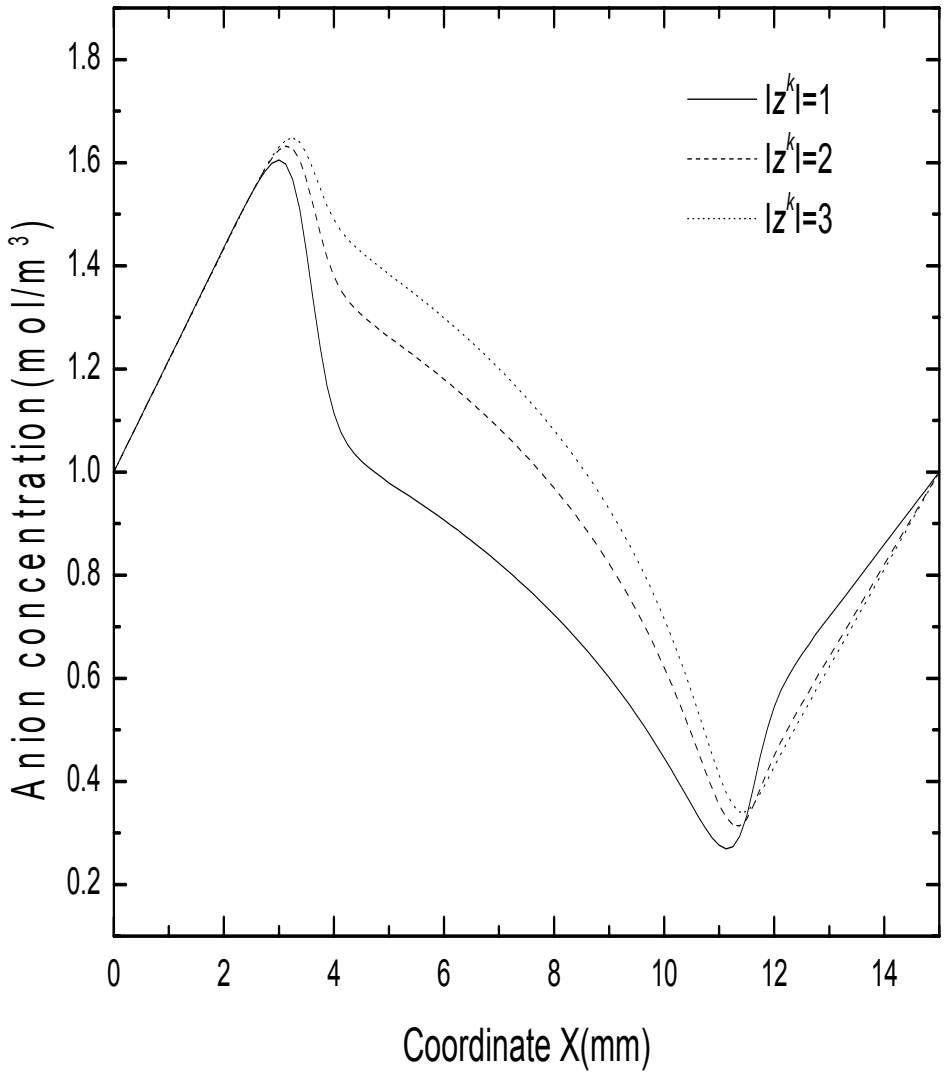

Figure 4.11(b) Effect of valence on the variation of anion concentration.

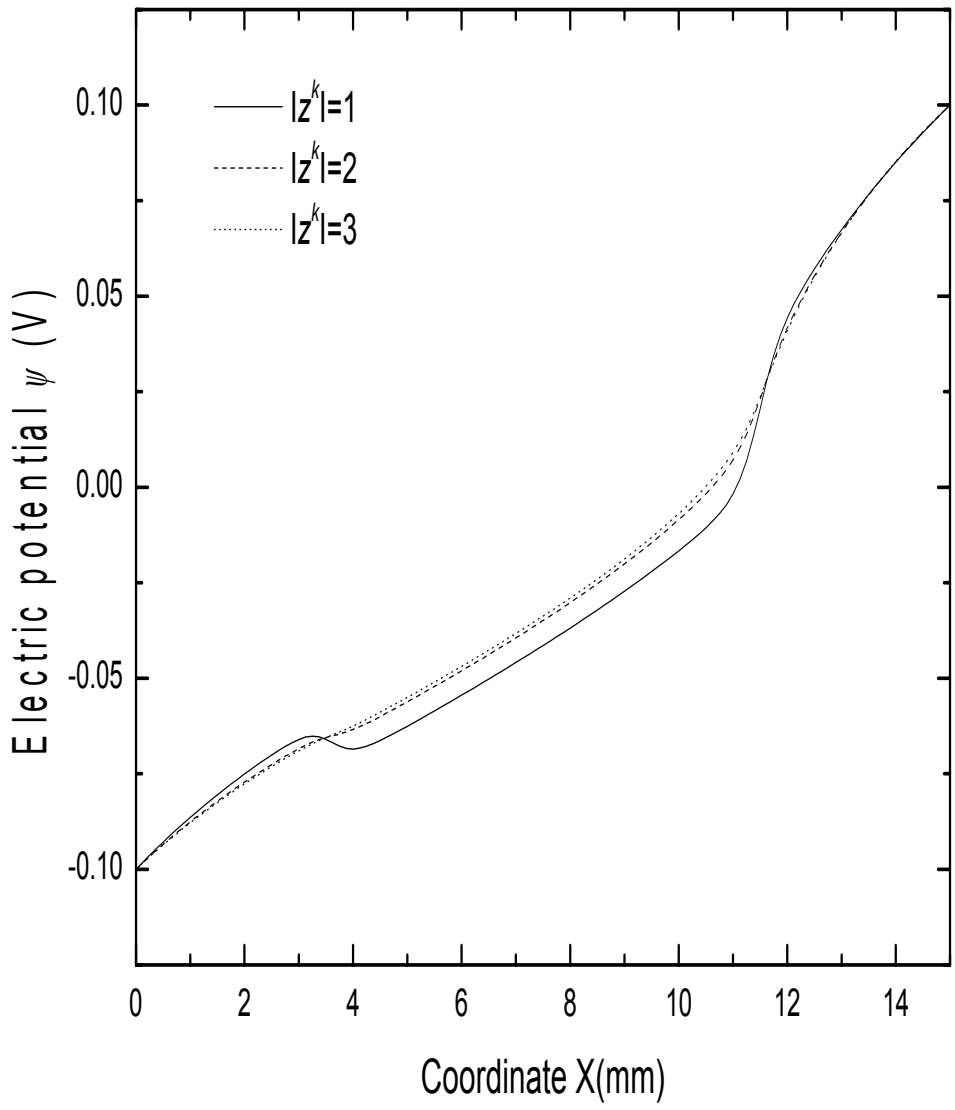

Figure 4.11(c) Effect of valence on the variation of electric potential.

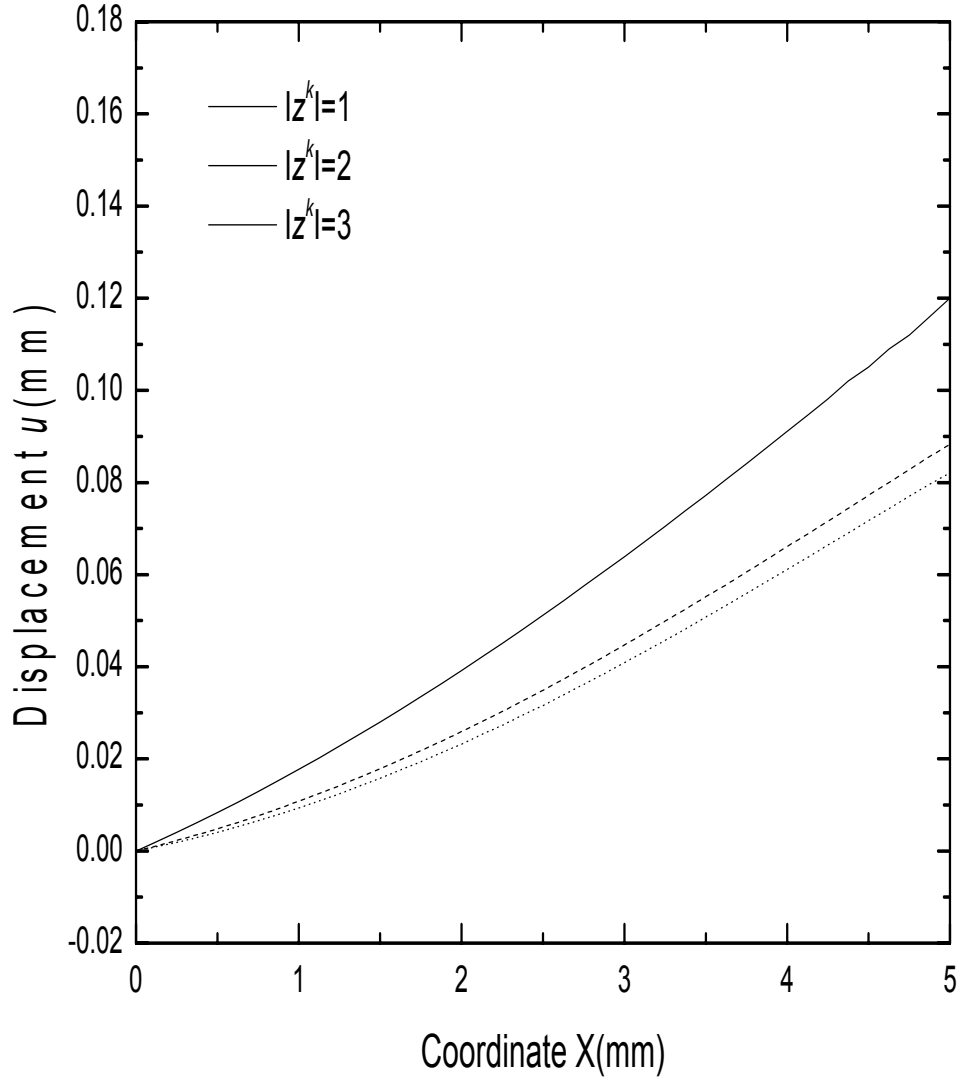

Figure 4.11(d) Effect of valence on the variation of displacement.

Chapter 5

One-dimensional Transient Simulations for Kinetics of Electric-Sensitive Hydrogels

In this chapter, the transient simulations for the kinetics of electric-stimulus responsive hydrogels are conducted by the developed MECe model. After the discretization of the MECe governing equations, a numerical comparison is made between the presently simulated results and experimental data extracted from the open literature. It is followed by the detailed discussions of the kinetic variations of several important parameters.

5.1 Discretization of the 1-D transient MECe governing equations

For transient analysis of the electric-sensitive hydrogels, the time term is required in the MECe transient governing equations. Corresponding to the non-dimensional nonlinear partial differential governing equations of the MECe model expressed by Equations (2.79)-(2.82), 1-D non-dimensional MECe transient governing equations can be written as

$$L_{ref}^2 \frac{\partial \bar{c}^k}{\partial t} = D_k \left(\frac{\partial^2 \bar{c}^k}{\partial \bar{x}^2} + \alpha z^k \frac{\partial \bar{c}^k}{\partial \bar{x}} \frac{\partial \bar{\psi}}{\partial \bar{x}} + \alpha z^k \bar{c}^k \frac{\partial^2 \bar{\psi}}{\partial \bar{x}^2} \right) \quad (k = +, -) \tag{5.1}$$

$$\frac{\partial^2 \bar{\psi}}{\partial \bar{x}^2} + \frac{F_c^2 L_{ref}^2 c_{ref}}{\varepsilon \varepsilon_0 RT\alpha} \left(\sum_{k=+,-} z^k \bar{c}^k + z^f \bar{c}^f \right) = 0 \tag{5.2}$$

$$(3\lambda_s + 2\mu_s) \frac{\partial^2 \bar{u}}{\partial \bar{x}^2} - \beta RT c_{ref} \frac{\partial \bar{p}}{\partial \bar{x}} = 0 \tag{5.3}$$

$$\frac{L_{ref}^2 f_{ws}}{c_{ref} RT}\frac{\partial \overline{u}_{,x}}{\partial t} = \beta(\phi^w \frac{\partial^2 \overline{p}}{\partial \overline{x}^2} + 2\frac{\partial \phi^w}{\partial \overline{x}}\frac{\partial \overline{p}}{\partial \overline{x}}) + \alpha[2\frac{\partial \phi^w}{\partial \overline{x}}\frac{\partial \overline{\psi}}{\partial \overline{x}}\sum_{k=+,-} z^k \overline{c}^k + \\ + \phi^w(\frac{\partial \overline{\psi}}{\partial \overline{x}}\sum_{k=+,-}(z^k \frac{\partial \overline{c}^k}{\partial \overline{x}}) + \frac{\partial^2 \overline{\psi}}{\partial \overline{x}^2}\sum_{k=+,-} z^k \overline{c}^k)] \tag{5.4}$$

in which all non-dimensional parameters and variables are defined in Equations (2.75)-(2.78).

According to the θ-weighted numerical finite-difference scheme ($0.5<\theta<1.0$), Equation (5.1) can be discretized in time domain as follows

$$\overline{c}^k_{(n+1)} - \overline{c}^k_{(n)} = \frac{\Delta t D_k}{L_{ref}^2}[\theta(\frac{\partial^2 \overline{c}^k_{(n+1)}}{\partial \overline{x}^2} + \alpha z^k \frac{\partial \overline{c}^k_{(n+1)}}{\partial \overline{x}}\frac{\partial \overline{\psi}_{(n+1)}}{\partial \overline{x}} + \alpha z^k \overline{c}^k_{(n+1)}\frac{\partial^2 \overline{\psi}_{(n+1)}}{\partial \overline{x}^2}) + \\ + (1-\theta)(\frac{\partial^2 \overline{c}^k_{(n)}}{\partial \overline{x}^2} + \alpha z^k \frac{\partial \overline{c}^k_{(n)}}{\partial \overline{x}}\frac{\partial \overline{\psi}_{(n)}}{\partial \overline{x}} + \alpha z^k \overline{c}^k_{(n)}\frac{\partial^2 \overline{\psi}_{(n)}}{\partial \overline{x}^2})] \tag{5.5}$$

where the subscript (n) and (n+1) denote time variable at $t = t_n$ and at subsequent time $t = t_{n+1}$ respectively and $\Delta t = t_{n+1} - t_n$ is the time step.

By the meshless Hermite-Cloud method, the governing equation (5.5) is further discretized in spatial domain as follows

$$\sum_{j=1}^{np} N_j(\overline{x}_i)\overline{c}^k_{j(n+1)} - \sum_{m=1}^{np}(\overline{x}_i - \sum_{j=1}^{np} N_j(\overline{x}_i)\overline{x}_j)M_m(\overline{x}_i)\overline{c}_{x\,m(n+1)} - \\ - \frac{\Delta t D_k \theta}{L_{ref}^2}\{\sum_{j=1}^{np} N_{xx\,j}(\overline{x}_i)\overline{c}^k_{j(n+1)} + \alpha z^k \sum_{m=1}^{np} M_m(\overline{x}_i)\overline{c}^{\,k}_{x\,m(n+1)}\sum_{m=1}^{np} M_m(\overline{x}_i)\overline{\psi}_{x\,m(n+1)} + \\ + \alpha z^k \sum_{j=1}^{np} N_{xx\,j}(\overline{x}_i)\overline{\psi}_{j(n+1)}[\sum_{j=1}^{np} N_j(\overline{x}_i)\overline{c}^k_{j(n+1)} - \sum_{m=1}^{np}(\overline{x}_i - \sum_{j=1}^{np} N_j(\overline{x}_i)\overline{x}_j)M_m(\overline{x}_i)\overline{c}_{x\,m(n+1)}]\} = \\ = \sum_{j=1}^{np} N_j(\overline{x}_i)\overline{c}^k_{j(n)} - \sum_{m=1}^{np}(\overline{x}_i - \sum_{j=1}^{np} N_j(\overline{x}_i)\overline{x}_j)M_m(\overline{x}_i)\overline{c}_{x\,m(n)} + \\ + \frac{\Delta t D_k (1-\theta)}{L_{ref}^2}\{\sum_{j=1}^{np} N_{xx\,j}(\overline{x}_i)\overline{c}^k_{j(n)} + \alpha z^k \sum_{m=1}^{np} M_m(\overline{x}_i)\overline{c}^{\,k}_{x\,m(n)}\sum_{m=1}^{np} M_m(\overline{x}_i)\overline{\psi}_{x\,m(n)} + \\ + \alpha z^k [\sum_{j=1}^{np} N_j(\overline{x}_i)\overline{c}^k_{j(n)} - \sum_{m=1}^{np}(\overline{x}_i - \sum_{j=1}^{np} N_j(\overline{x}_i)\overline{x}_j)M_m(\overline{x}_i)\overline{c}_{x\,m(n)}]\sum_{j=1}^{np} N_{xx\,j}(\overline{x}_i)\overline{\psi}_{j(n)}\} \tag{5.6}$$

Similarly, the other three governing equations (5.2) to (5.4) can also be

discretized to

$$\sum_{j=1}^{np} N_{xx\,j}(\bar{x}_i)\overline{\psi}_{j(n+1)} + \frac{F_c^2 L_{ref}^2 c_{ref}}{\varepsilon\varepsilon_0 RT\alpha}\{z^f \bar{c}^f + \sum_{k=+,-} z^k [\sum_{j=1}^{np} N_j(\bar{x}_i)\bar{c}^k_{j(n+1)} - \\ - \sum_{m=1}^{np}(\bar{x}_i - \sum_{j=1}^{np} N_j(\bar{x}_i)\bar{x}_j) M_m(\bar{x}_i)\bar{c}_{x\,m(n+1)}]\} = 0 \tag{5.7}$$

$$(3\lambda_s + 2\mu_s)\sum_{j=1}^{npGel} N_{xx\,j}(\bar{x}_i)\bar{u}_{j(n+1)} - \beta RTc_{ref}\sum_{m=1}^{npGel} M_m(\bar{x}_i)\bar{p}_{x\,m(n+1)} = 0 \tag{5.8}$$

$$\frac{L_{ref}^2 f_{ws}}{c_{ref}RT}\sum_{m=1}^{npGel} M_m(\bar{x}_i)\bar{u}_{x\,m(n+1)} - \Delta t\theta\beta[\phi^w \sum_{j=1}^{npGel} N_{xx\,j}(\bar{x}_i)\bar{p}_{j(n+1)} + \\ + 2\frac{\partial\phi^w}{\partial\bar{x}}\sum_{m=1}^{npGel} M_m(\bar{x}_i)\bar{p}_{x\,m(n+1)}] - \alpha\Delta t\theta\{2\frac{\partial\phi^w}{\partial\bar{x}}[\sum_{m=1}^{npGel} M_m(\bar{x}_i)\overline{\psi}_{x\,m(n+1)}]\times \\ \times[\sum_{k=+,-} z^k \sum_{j=1}^{npGel}(N_j(\bar{x}_i)\bar{c}^k_{j(n+1)} - \sum_{m=1}^{npGel}(\bar{x}_i - \sum_{j=1}^{npGel} N_j(\bar{x}_i)\bar{x}_j) M_m(\bar{x}_i)\bar{c}_{x\,m(n+1)})] + \\ + \phi^w[\sum_{m=1}^{npGel} M_m(\bar{x}_i)\overline{\psi}_{x\,m(n+1)}(\sum_{k=+,-} z^k \sum_{m=1}^{npGel} M_m(\bar{x}_i)\bar{c}^{\,k}_{x\,m(n+1)}) + \\ + \sum_{j=1}^{npGel} N_{xx\,j}(\bar{x}_i)\overline{\psi}_{j(n+1)}\sum_{k=+,-} z^k \sum_{j=1}^{npGel}(N_j(\bar{x}_i)\bar{c}^k_{j(n+1)} - \\ - \sum_{m=1}^{npGel}(\bar{x}_i - \sum_{j=1}^{npGel} N_j(\bar{x}_i)\bar{x}_j) M_m(\bar{x}_i)\bar{c}_{x\,m(n+1)})]\} =$$

$$= \frac{L_{ref}^2 f_{ws}}{c_{ref}RT}\sum_{m=1}^{npGel} M_m(\bar{x}_i)\bar{u}_{x\,m(n)} + \\ + \Delta t(1-\theta)\beta[\phi^w \sum_{j=1}^{npGel} N_{xx\,j}(\bar{x}_i)\bar{p}_{j(n)} + 2\frac{\partial\phi^w}{\partial\bar{x}}\sum_{m=1}^{npGel} M_m(\bar{x}_i)\bar{p}_{x\,m(n)}] + \\ + \alpha\Delta t(1-\theta)\{2\frac{\partial\phi^w}{\partial\bar{x}}[\sum_{m=1}^{npGel} M_m(\bar{x}_i)\overline{\psi}_{x\,m(n)}][\sum_{k=+,-} z^k \sum_{j=1}^{npGel}(N_j(\bar{x}_i)\bar{c}^k_{j(n)} - \\ - \sum_{m=1}^{npGel}(\bar{x}_i - \sum_{j=1}^{npGel} N_j(\bar{x}_i)\bar{x}_j) M_m(\bar{x}_i)\bar{c}_{x\,m(n)})] + \\ + \phi^w[\sum_{m=1}^{npGel} M_m(\bar{x}_i)\overline{\psi}_{x\,m(n)}(\sum_{k=+,-} z^k \sum_{m=1}^{npGel} M_m(\bar{x}_i)\bar{c}^{\,k}_{x\,m(n)}) + \\ + \sum_{j=1}^{npGel} N_{xx\,j}(\bar{x}_i)\overline{\psi}_{j(n)}\sum_{k=+,-} z^k \sum_{j=1}^{npGel}(N_j(\bar{x}_i)\bar{c}^k_{j(n)} - \\ - \sum_{m=1}^{npGel}(\bar{x}_i - \sum_{j=1}^{npGel} N_j(\bar{x}_i)\bar{x}_j) M_m(\bar{x}_i)\bar{c}_{x\,m(n)})]\} \tag{5.9}$$

Additionally, based on the Hermite theorem, the following auxiliary equations are required

$$\sum_{j=1}^{np} N_{xj}(\bar{x}_i)\bar{c}_j^k - [\sum_{j=1}^{np} N_{xj}(\bar{x}_i)\bar{x}_j]\sum_{m=1}^{np} M_m(\bar{x}_i)\bar{c}_{xm}^{\,k} = 0 \tag{5.10}$$

$$\sum_{j=1}^{np} N_{xj}(\bar{x}_i)\overline{\psi}_j - [\sum_{j=1}^{np} N_{xj}(\bar{x}_i)\bar{x}_j]\sum_{m=1}^{np} M_m(\bar{x}_i)\overline{\psi}_{xm} = 0 \tag{5.11}$$

$$\sum_{j=1}^{npGel} N_{xj}(\bar{x}_i)\bar{u}_j - [\sum_{j=1}^{npGel} N_{xj}(\bar{x}_i)\bar{x}_j]\sum_{m=1}^{npGel} M_m(\bar{x}_i)\bar{u}_{xm} = 0 \tag{5.12}$$

$$\sum_{j=1}^{npGel} N_{xj}(\bar{x}_i)\bar{p}_j - [\sum_{j=1}^{npGel} N_{xj}(\bar{x}_i)\bar{x}_j]\sum_{m=1}^{npGel} M_m(\bar{x}_i)\bar{p}_{xm} = 0 \tag{5.13}$$

5.2 Experimental validation

In the experimental aspect of the kinetic responsive behaviors of electric-sensitive hydrogels subject to an externally applied electric field, extensive search of the literature has thus far yielded only one published work done by Shiga et al. (1990), who measured the endpoint displacement *D* of hydrogel strip in a convenient observation manner in the experiments, as shown in Figure 4.1, instead of the displacement *u* at the edge point *a* of the hydrogel domain between points *a* and *b* along *x* axis in the present 1-D simulations. Thus a relationship is required between these two displacements to compare the simulated results with experimental data. The experimental data (Shiga et al., 1990) employed as the input data for the present numerical computation include T=298(K), F_c=9.648×10^4(C/mol), R=8.314(J/mol·K), $\phi_0^w = 0.8$, $L = 5.0\times10^{-2}$(m), $\varepsilon_0 = 8.854\times10^{-12}$(C^2/Nm^2), $\varepsilon = 80$, V_e = 3.0(V), h = 5.0×10^{-3} (m),

$c_0^f = 35.3(\text{mol/m}^3)$, c^* = 35.3 (mol/m^3), z^f =–1, and $3\lambda + 2\mu = 1.8\times10^4$(Pa) (It is adjusted for determination of a reference configuration. In fact, as described by Lai et al. (1991), *"any configuration may serve a reference"*. As such, the reference configuration is defined here to establish easily the relationship between the displacements u and D only). The computed displacement u and experimentally measured displacement D are tabulated in Table 5.1, at time t=1, 2, 3, 4 and 5 (min), respectively. For construction of the relationship between the displacements u and D, the least square method is applied to both the displacements u and D at time t=1, 3 and 5 (min) with best-fitting, based on the data in Table 5.1, and thus the relationship between the displacements u and D is developed as

$$D = 1.58 + 0.93u + 0.47u^2 \tag{5.14}$$

Subsequently, substituting the displacements u and D at time t=2 and 4 (min) into Equation (5.14), the relative discrepancies are computed and then they are generally found to be smaller than 6%, which validates the relationship (5.14) between the displacements u and D acceptable.

Figure 5.1 shows the comparison of the experimental endpoint displacement with the corresponding simulated endpoint displacement computed by Equation (5.14), where a very good agreement is achieved due to the acceptable relative errors being 1.0%, 5.8%, 1.0%, 2.9% and 1.0% at time t=1, 2, 3, 4 and 5 (min), respectively. This confirms that the presently developed MECe model is suitable for the kinetic analysis of electric-stimulus responsive hydrogels.

5.3 Kinetic studies of parameters

In the previous steady-state analysis of the electric-sensitive hydrogels, the efforts are put into studying the influences of different physical parameters on the responsive steady-state behaviors of the hydrogels, including the distributions of diffusive ionic concentrations, electric potential and hydrogel displacement. In the present transient analysis, the variations of these parameter distributions with time are focused and discussed in detail. In the following numerical simulations, several parameters taken are $\phi_0^w = 0.8$, T=298(K), F_c=9.648×10^4(C/mol), R=8.314(J/mol·K), L=1.5×10^{-2}(m), $\varepsilon_0 = 8.854\times10^{-12}(\mathrm{C^2/Nm^2})$, $\varepsilon = 80$, $3\lambda + 2\mu = 1.2\times10^5$(Pa), z^f =–1, $h = 5\times10^{-3}$(m), f_{ws} = 7.0×10^{-16}(Ns/m^4) and D_k = 1.0×10^{-7}(m^2/s).

5.3.1 Variation of ionic concentration distributions with time

Figures 5.2 to 5.15 present the variations of ionic concentration distributions with time under different combinations of the electric fields, fixed-charge densities and bath solution concentrations. These figures depict the kinetics of the electric-stimulus responsive hydrogels and the kinetic performance of ionic diffusion and convection. It is observed that, at initial time t=0, the external electric field is not imposed and then the distributions of ionic concentrations in whole computational domain are symmetric, resulting from the steady-state simulations without the external electric field. Once the electric field is applied on

the system, the distributions of diffusive ionic concentrations are no longer symmetric. With the increase of time, the diffusive ions redistribute continuously in both the hydrogel and bath solution, and the ionic concentration differences near the hydrogel-solution interfaces become larger and larger. It is expected that the ionic diffusion and convection will reach the equilibrium state after a specific time, which is dependent on various parameters and conditions, including the electric field, fixed-charge density and bath solution concentration. In general, the kinetic trends of ionic concentration distributions in Figures 5.2 to 5.15 are in good agreement with the FEM results carried out by Wallmersperger et al. (2001).

It is also observed from Figures 5.2 to 5.4 and 5.9 to 5.11 that, if other parameters are fixed at a given time, the peak values of ionic concentrations on the hydrogel-solution interface near the cathode increase with the enlargement of the applied electric-field voltage, while those near the anode decrease. This means that, at a given time, the ionic concentration difference between the two hydrogel-solution interfaces increase with the applied electric field. The present transient simulations are consistent with those in steady-state studies, where the ionic concentration difference in equilibrium state becomes larger as well with the increment of the applied voltage.

Variations of ionic concentration distributions with time under different fixed-charge densities are shown in Figures 5.2, 5.5, 5.6, 5.9, 5.12 and 5.13. They have similar characteristics to the steady-state simulations, where, with the change of fixed-charge densities, the changes of the cation Na^+ distributions at a given

time are significant, while those of the anion Cl^- distributions are small. Probably this results from the negative valence of fixed-charge groups. By comparing Figures 5.2, 5.7 to 5.9, 5.14 and 5.15, it is obviously found that, as the bath solution concentration increases, the kinetic gradient of ion concentration within the hydrogels increases.

5.3.2 Variation of electric potential distributions with time

Figures 5.16 to 5.22 show the kinetic variations of electric potential distributions under different environmental conditions. It is presented that, generally the downward step of the electric potential distributions within hydrogels becomes larger with the increase of time. After time about 100(s), the step changes gradually. Furthermore, it is found from Figures 5.16 to 5.18 that, with the increase of externally applied electric voltage, the step of electric potential distributions on the hydrogel-solution interface near the cathode diminishes gradually, while that near the anode increases. It is also seen from Figures 5.16, 5.19 and 5.20 that, with the increase of fixed-charge density, the variation of electric potential distributions with time becomes small. Probably the reason is that a higher fixed-charge density attracts more mobile ions into hydrogels and thus makes the conductivity within hydrogels close to that of the surrounding bath solution.

5.3.3 Variation of hydrogel displacement distributions with time

Figures 5.23 to 5.29 present the variations of hydrogel displacement distributions with time. The trend of hydrogel displacement distributions is generally similar to that of electric potential distributions, namely, the displacement increases with time, in which the displacement initially increases rapidly, and then increases gradually. It is also note from these figures that the distributions of hydrogel displacement are nonlinear under externally applied electric field. The hydrogel displacement is linearly distributed along the x coordinate before the external electric field is applied. Once the electric field is loaded, there is the coupling effect of chemical and electric field in the considered system, where the hydrogel displacement immediately demonstrates the nonlinear distribution. It is evidently observed from Figures 5.23 to 5.29 that the curves are linear at t=0, and subsequently nonlinear.

5.3.4 Variation of average curvatures with time

As an important physical parameter measuring the extent of hydrogel deformation, the average curvature Ka defined by $Ka = 2(e_1 - e_2)/(h(2 + e_1 + e_2))$ in section 4.3 is also discussed in details. It is seen from Figure 5.30 that for a given voltage, the average curvature Ka initially increases rapidly with time and then approaches the stable value after a critical time, which varies with the change of applied voltages. The critical time decreases with the increase of voltage. It may be explained that, the higher is the electric-field voltage, the larger is the drag force applied on the diffusive ions, which leads to reaching the equilibrium state

shortly. Based on the discussion of Figure 5.30, it is concluded that at a given time, the high voltage makes a larger average curvature. It is reasonable because a strong electric field can result in a higher ionic concentration difference, which will induce the larger deformation of hydrogels.

Figure 5.31 shows the effect of fixed-charge density on the distributions of average curvature with time, in which a critical time is also observed in the variation of average curvature, and the critical time decreases with increasing the fixed-charge density. A possible reason is that the fixed-charge is another driving source for ionic diffusion besides the electric field. It is found that at a given time, the average curvature increases with the increase of fixed-charge density. This is consistent with the previous steady-state studies, where the increase of fixed-charge density makes a larger deformation of hydrogel.

Figure 5.32 demonstrates the influence of bath solution concentrations on the variation of average curvature with time. It is seen that the critical time changes slightly with the bath solution concentration, which implies that the influence of the bath solution concentrations on the critical time is not significant in comparison with the effects of electric field and fixed-charge density. It is also illustrated in Figure 5.32 that, at a given time, the average curvature decreases as the bath solution concentration increases. This is consistent with the previous studies in the section 4.4.3, namely, the variation of diffusive ionic concentrations because of the effect of fixed-charge groups is negligibly small if the bath solution concentration is much larger than the fixed-charge density.

By comparing Figures 5.30 to 5.32, it is observed that, in general, the average curvature *Ka* initially increases rapidly, and then increases gradually. It reveals that the electric-sensitive hydrogels have capability of responding very fast to the externally electric triggers, which is a very important feature of the hydrogels and makes them very suitable for BioMEMS application as biosensors/bioactuators.

Table 5.1 Measured displacement D and computed displacement u.

Time (min)	1	2	3	4	5
Displacement D† (mm)	2.1	3.1	4.1	5.0	6.1
Displacement u‡ (mm)	0.45	0.97	1.54	1.94	2.27

† Displacement D is measured experimentally at the endpoint of hydrogel strip, as shown in Figure 4.1.

‡ Displacement u is simulated numerically at the edge point a of the 1-D computational domain, as shown in Figure 4.1.

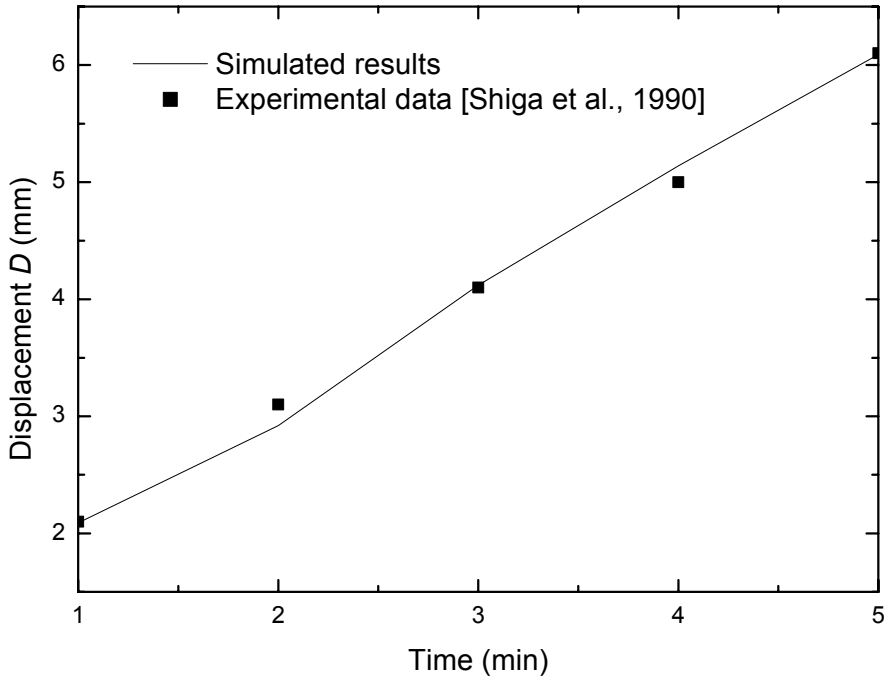

Figure 5.1 Comparison between the transient simulated results for hydrogel displacement and experimental data.

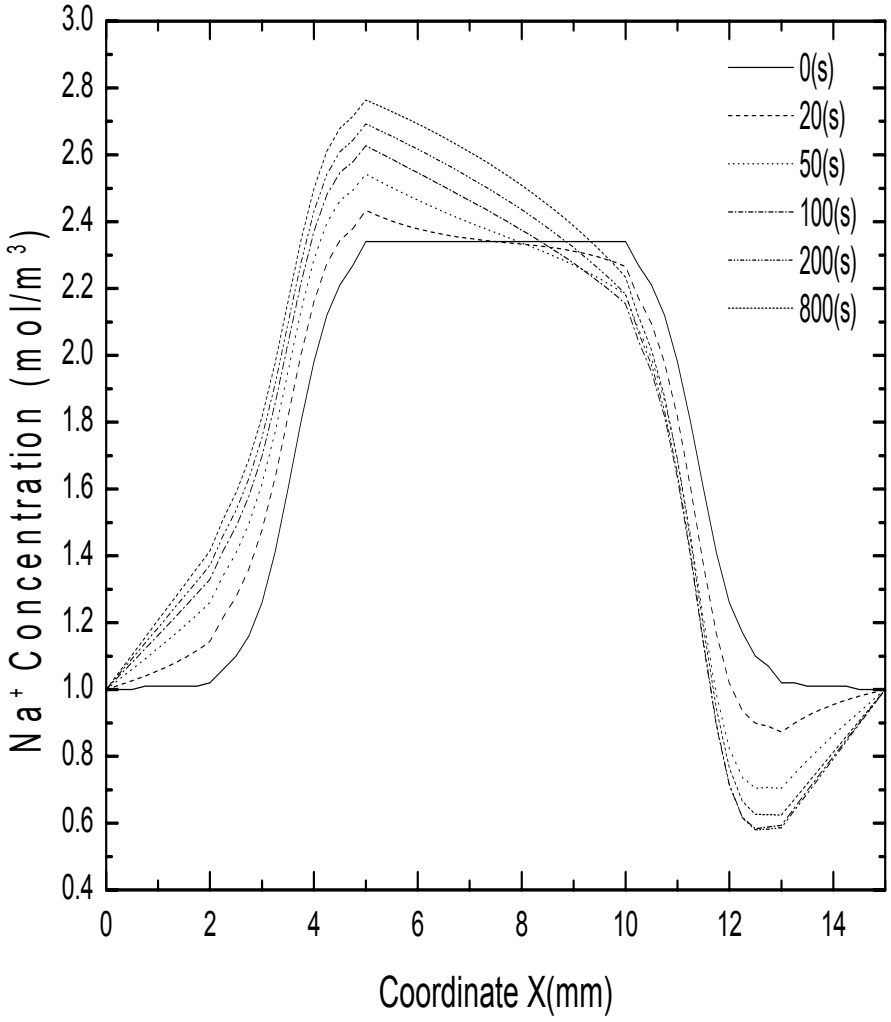

Figure 5.2 Variation of cation Na^+ concentration with time for V_e = 0.2(V), c_0^f = 2(mol/m^3) and c^* = 1(mol/m^3).

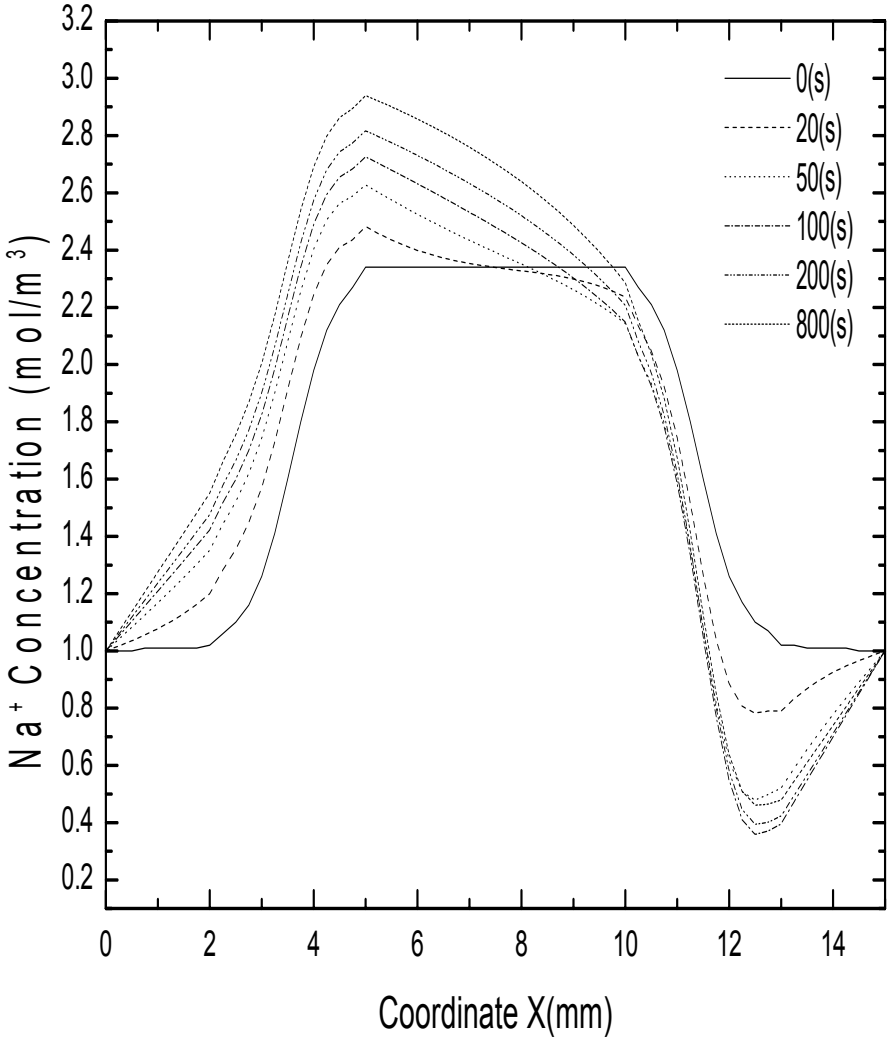

Figure 5.3 Variation of cation Na^+ concentration with time for $V_e = 0.3$(V), $c_0^f = 2(\text{mol/m}^3)$ and $c^* = 1(\text{mol/m}^3)$.

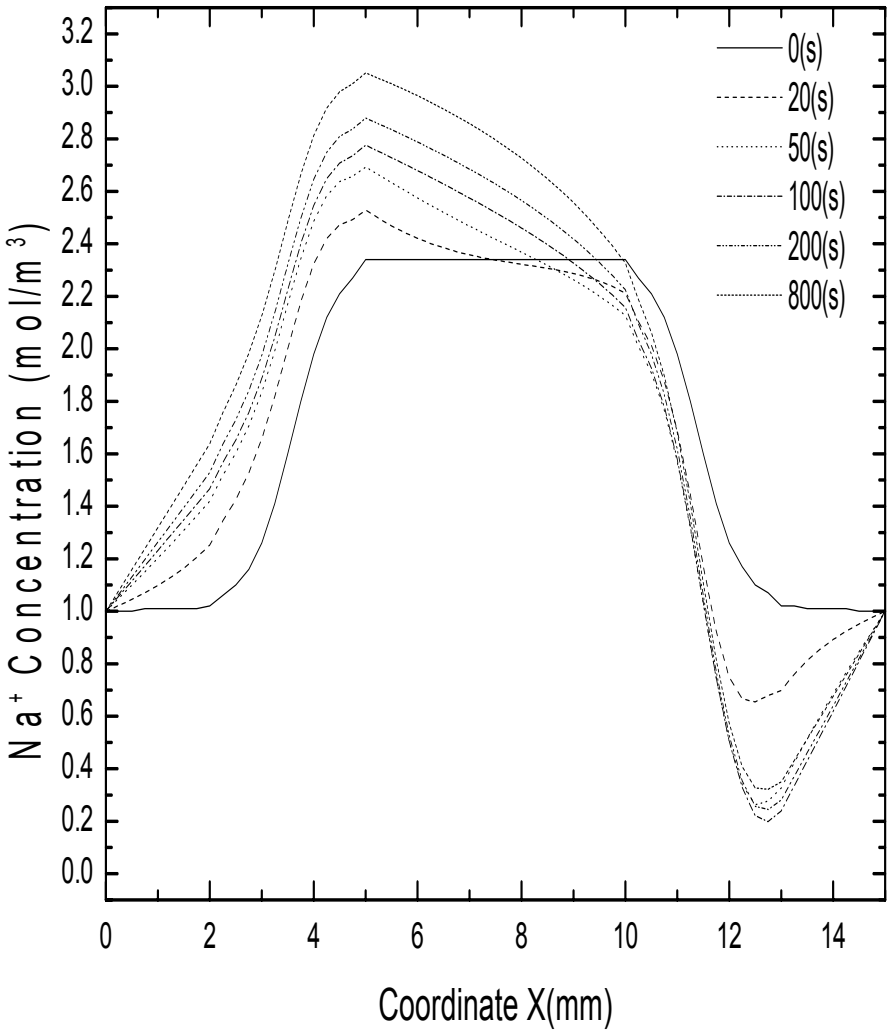

Figure 5.4 Variation of cation Na^+ concentration with time for $V_e = 0.4$(V), $c_0^f = 2(\text{mol/m}^3)$ and $c^* = 1(\text{mol/m}^3)$.

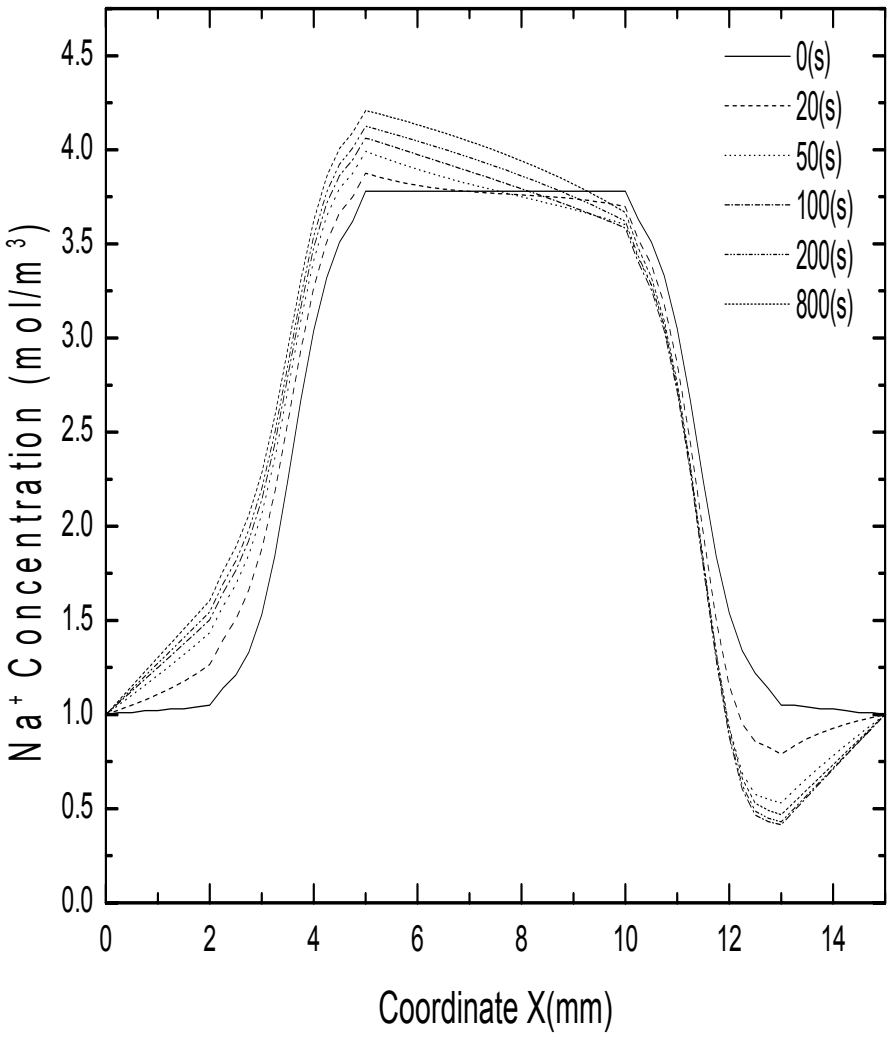

Figure 5.5 Variation of cation Na^+ concentration with time for $V_e = 0.2$(V), $c_0^f = 4(\text{mol/m}^3)$ and $c^* = 1(\text{mol/m}^3)$.

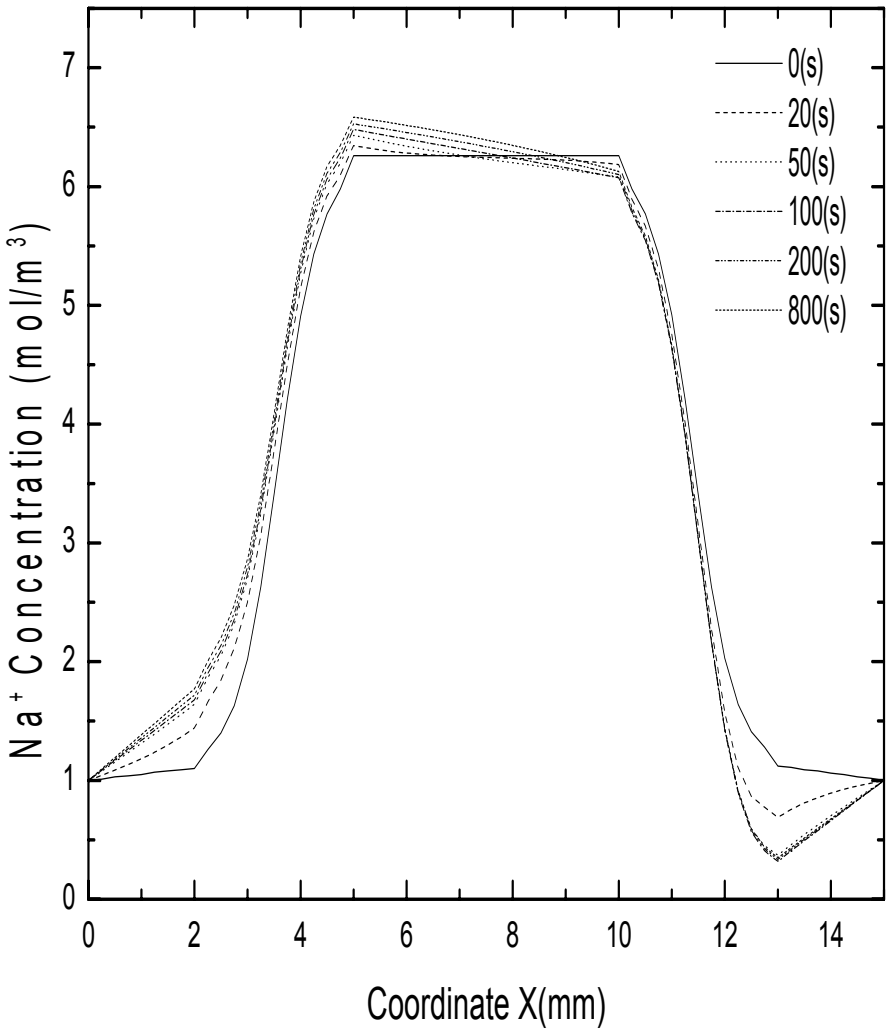

Figure 5.6 Variation of cation Na^+ concentration with time for $V_e = 0.2$(V), $c_0^f = 8(\text{mol/m}^3)$ and $c^* = 1(\text{mol/m}^3)$.

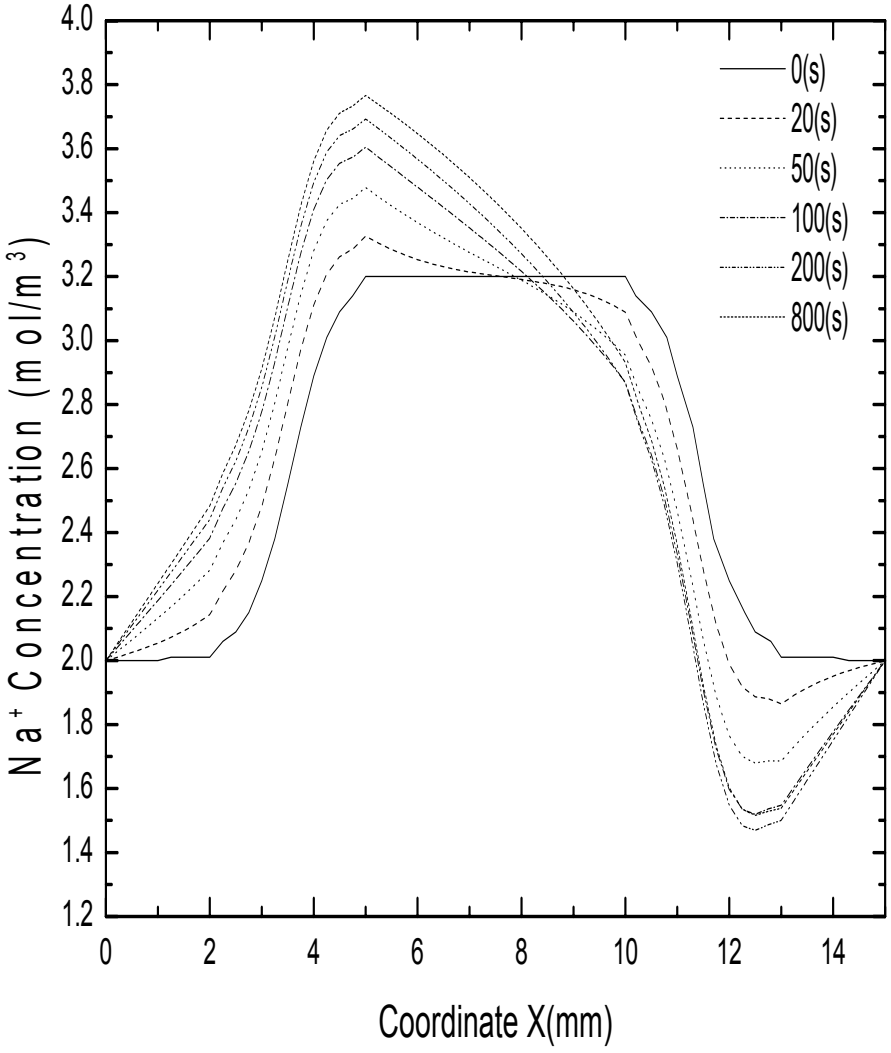

Figure 5.7 Variation of cation Na^+ concentration with time for $V_e = 0.2$(V), $c_0^f = 2(\text{mol/m}^3)$ and $c^* = 2(\text{mol/m}^3)$.

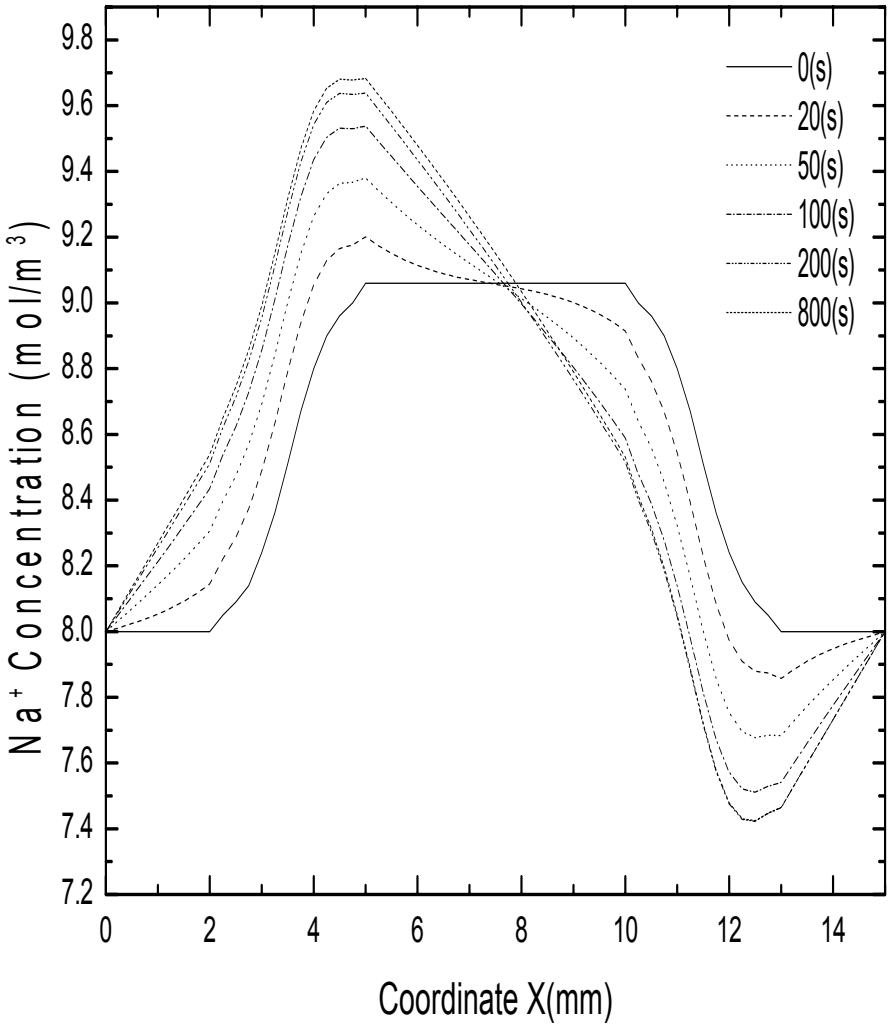

Figure 5.8 Variation of cation Na^+ concentration with time for $V_e = 0.2$(V), $c_0^f = 2(\text{mol/m}^3)$ and $c^* = 8(\text{mol/m}^3)$.

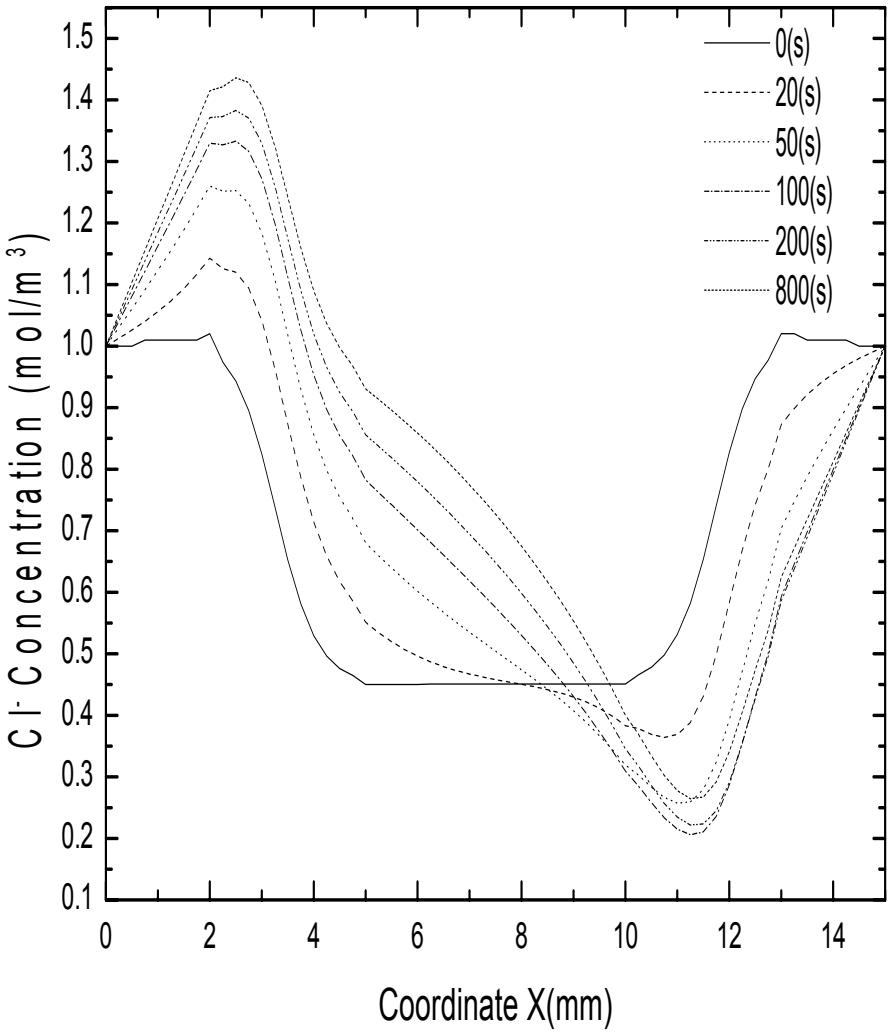

Figure 5.9 Variation of anion Cl^- concentration with time for $V_e = 0.2$(V), $c_0^f =$ $2(\text{mol/m}^3)$ and $c^* = 1(\text{mol/m}^3)$.

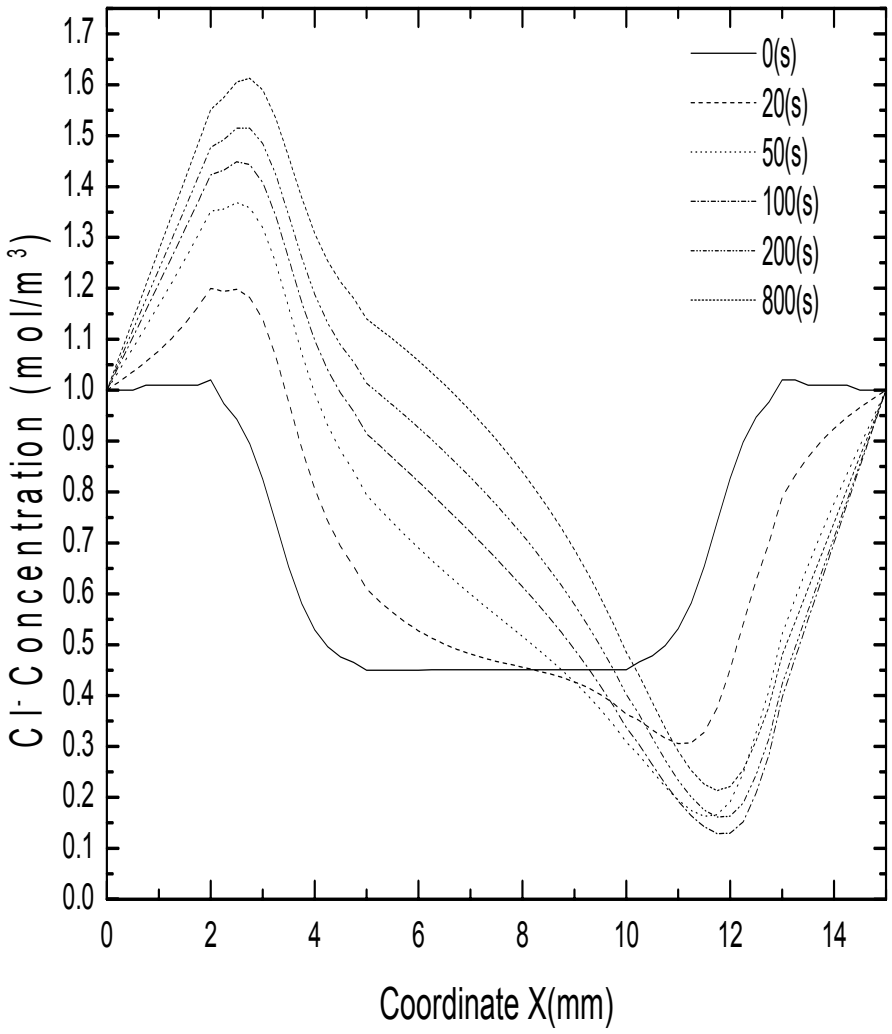

Figure 5.10 Variation of anion Cl^- concentration with time for $V_e = 0.3$(V), $c_0^f = 2(\text{mol/m}^3)$ and $c^* = 1(\text{mol/m}^3)$.

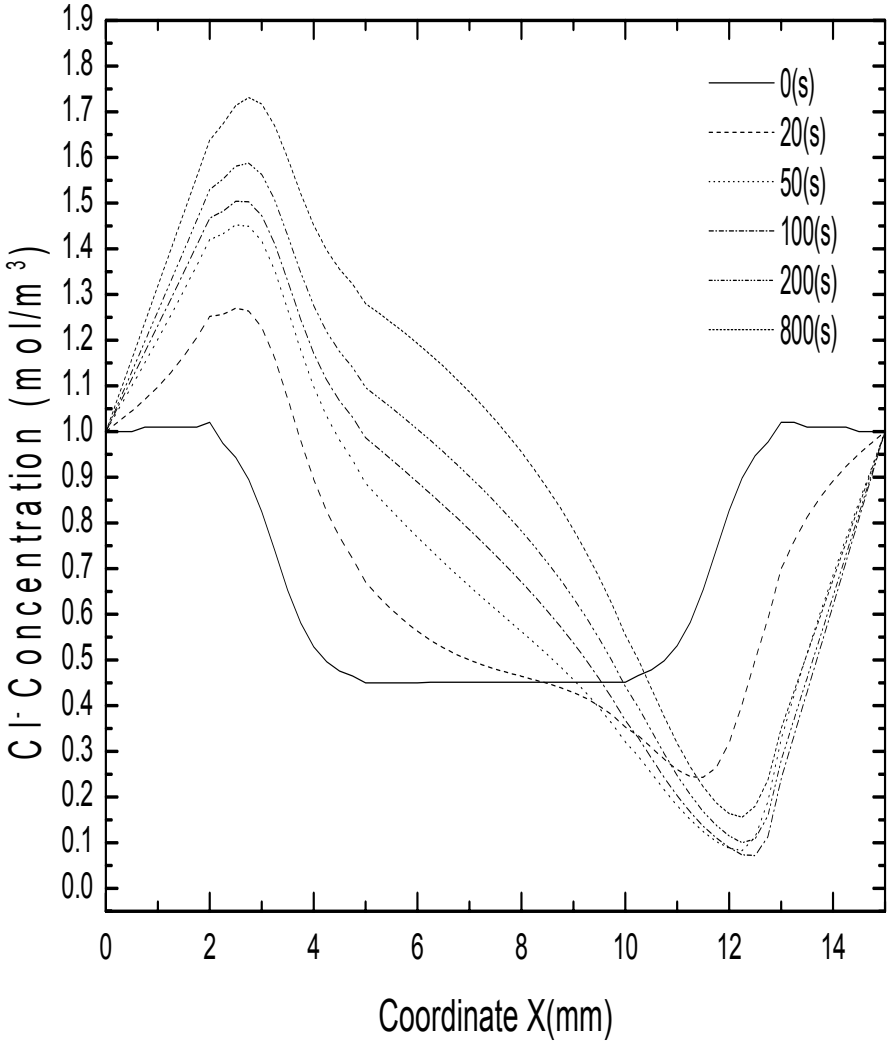

Figure 5.11 Variation of anion Cl^- concentration with time for $V_e = 0.4$(V), $c_0^f = 2(\text{mol/m}^3)$ and $c^* = 1(\text{mol/m}^3)$.

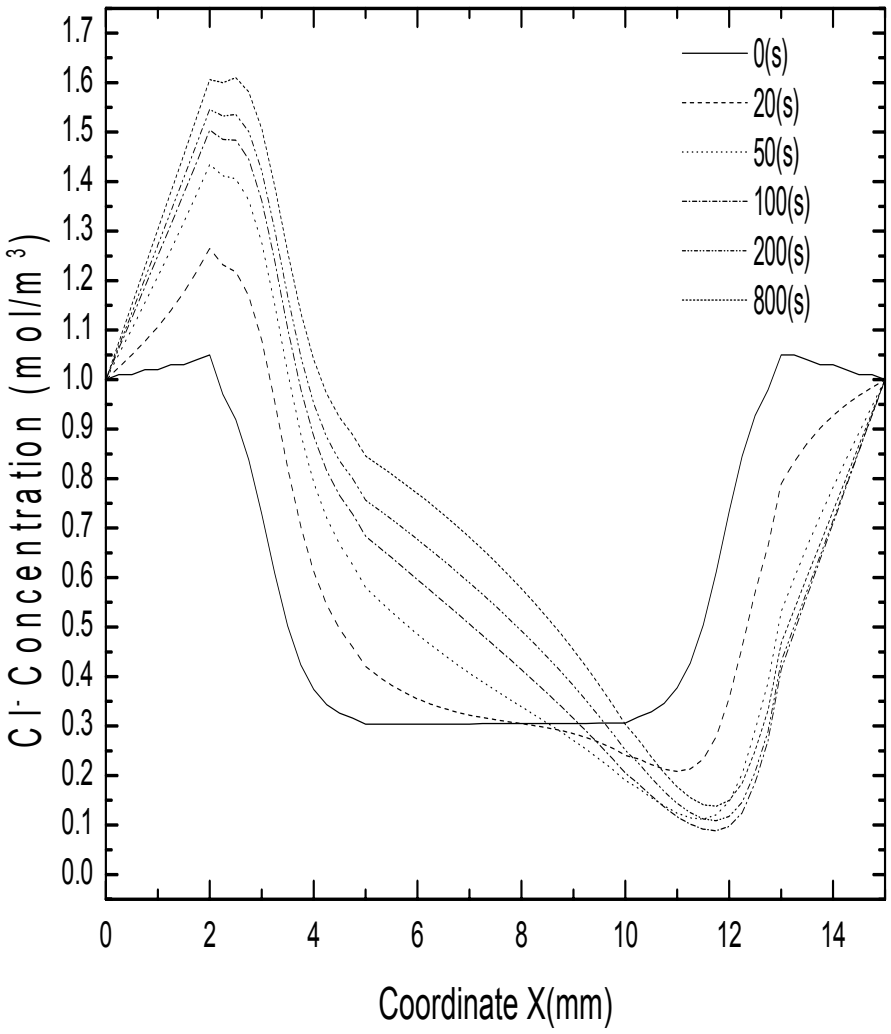

Figure 5.12 Variation of anion Cl^- concentration with time for $V_e = 0.2$(V), $c_0^f = 4(\text{mol/m}^3)$ and $c^* = 1(\text{mol/m}^3)$.

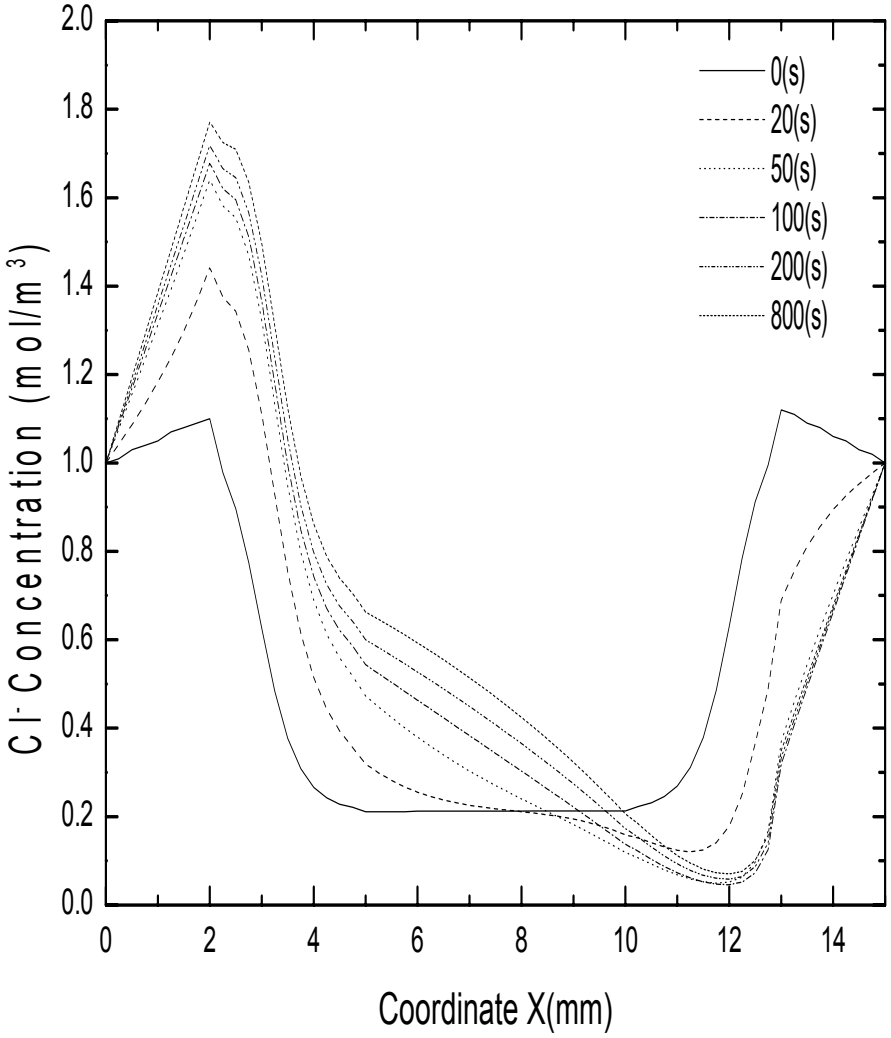

Figure 5.13 Variation of anion Cl^- concentration with time for $V_e = 0.2$(V), $c_0^f = 8(\text{mol/m}^3)$ and $c^* = 1(\text{mol/m}^3)$.

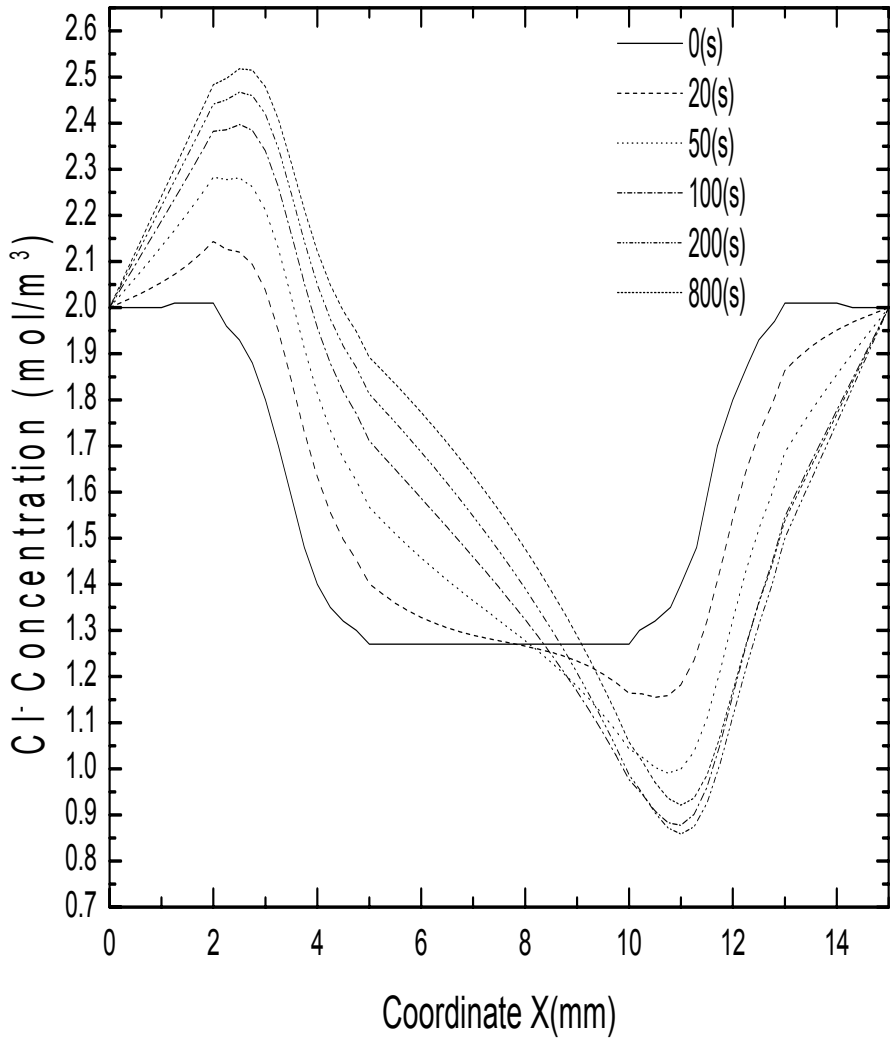

Figure 5.14 Variation of anion Cl^- concentration with time for $V_e = 0.2$(V), $c_0^f = 2$(mol/m^3) and $c^* = 2$(mol/m^3).

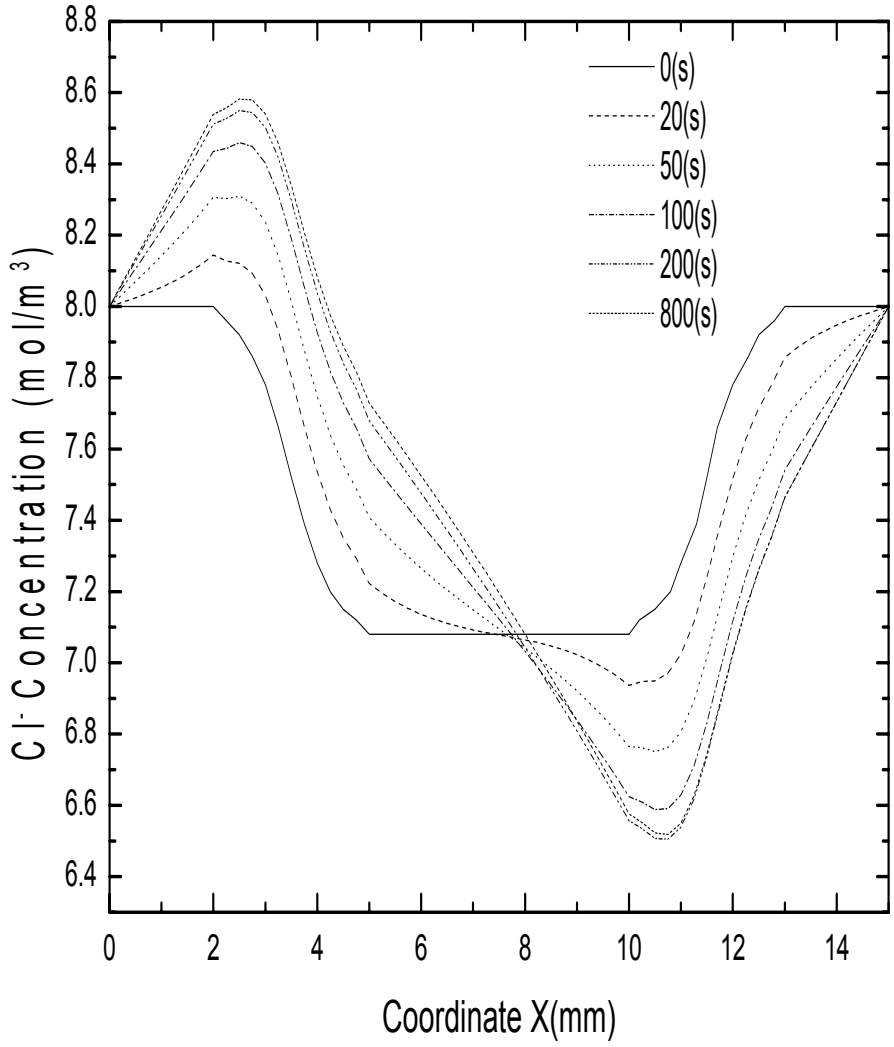

Figure 5.15 Variation of anion Cl^- concentration with time for $V_e = 0.2$(V), $c_0^f = 2(\text{mol/m}^3)$ and $c^* = 8(\text{mol/m}^3)$.

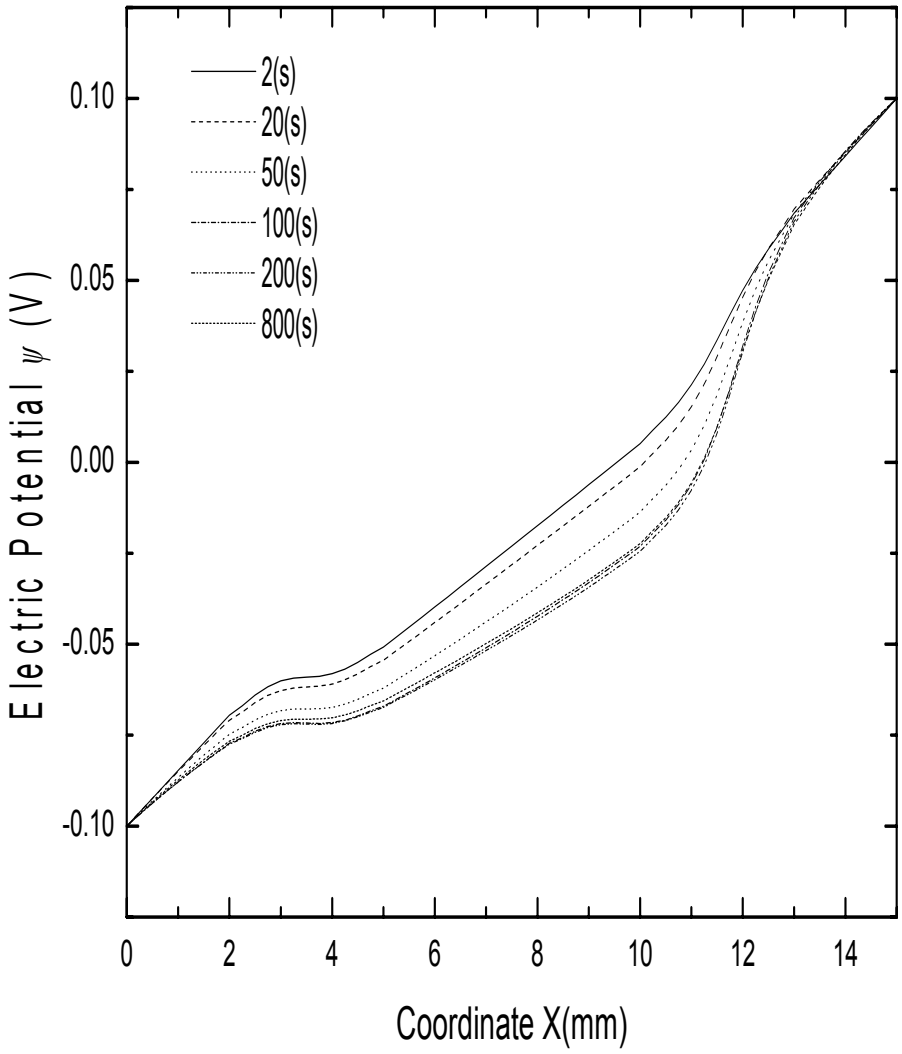

Figure 5.16 Variation of electric potential with time for V_e = 0.2(V), c_0^f = 2(mol/m^3) and c^* = 1(mol/m^3).

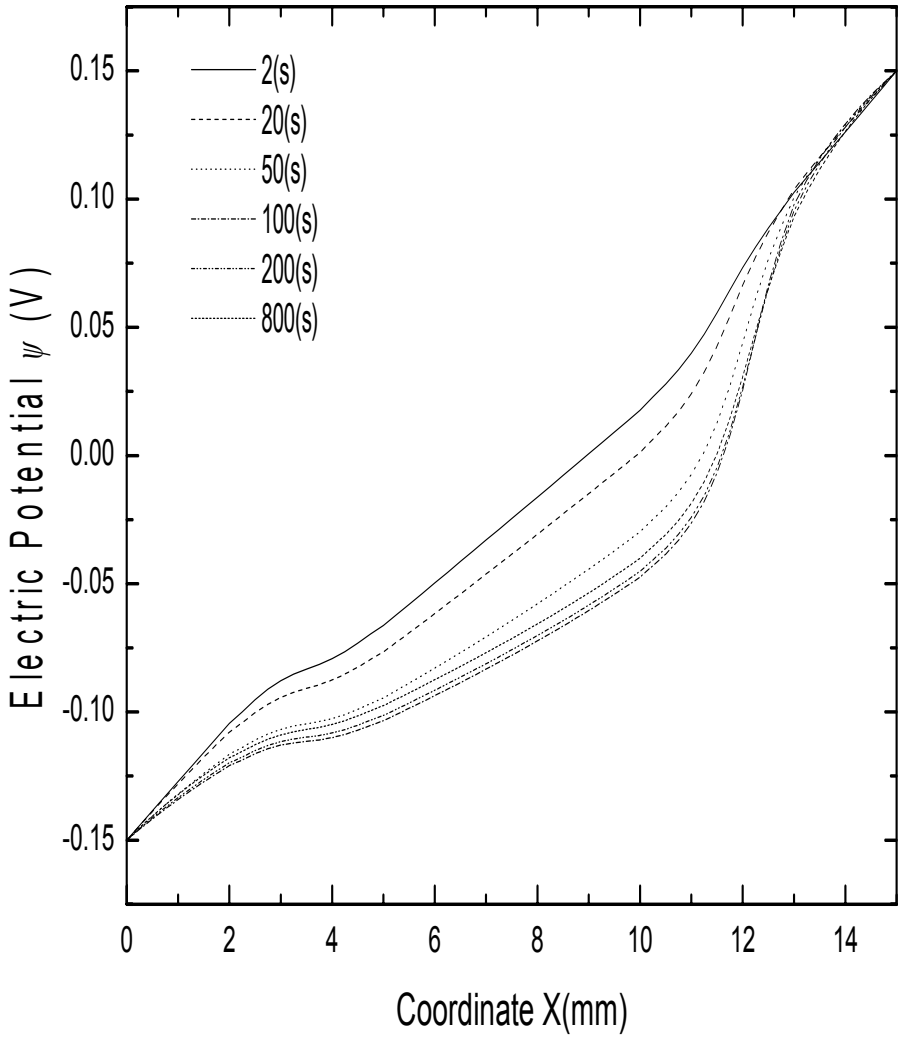

Figure 5.17 Variation of electric potential with time for V_e = 0.3(V), c_0^f = 2(mol/m^3) and c^* = 1(mol/m^3).

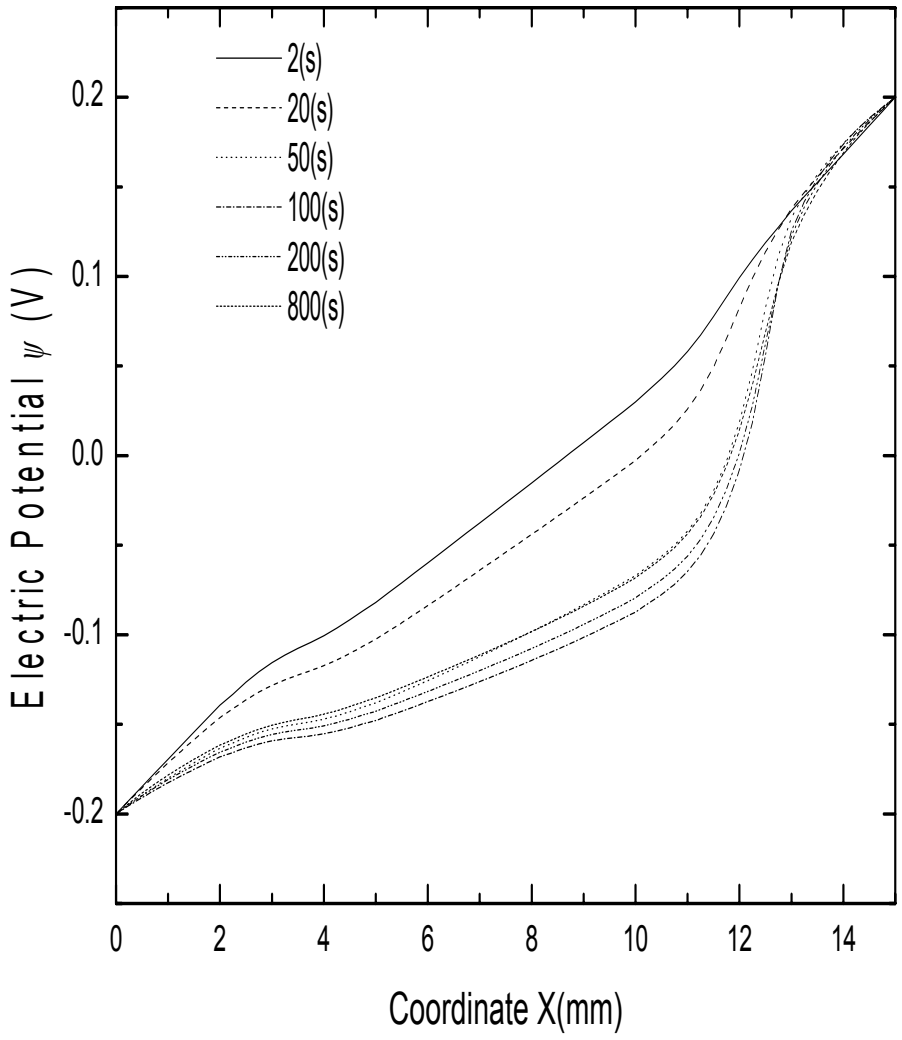

Figure 5.18 Variation of electric potential with time for V_e = 0.4(V), c_0^f = 2(mol/m^3) and c^* = 1(mol/m^3).

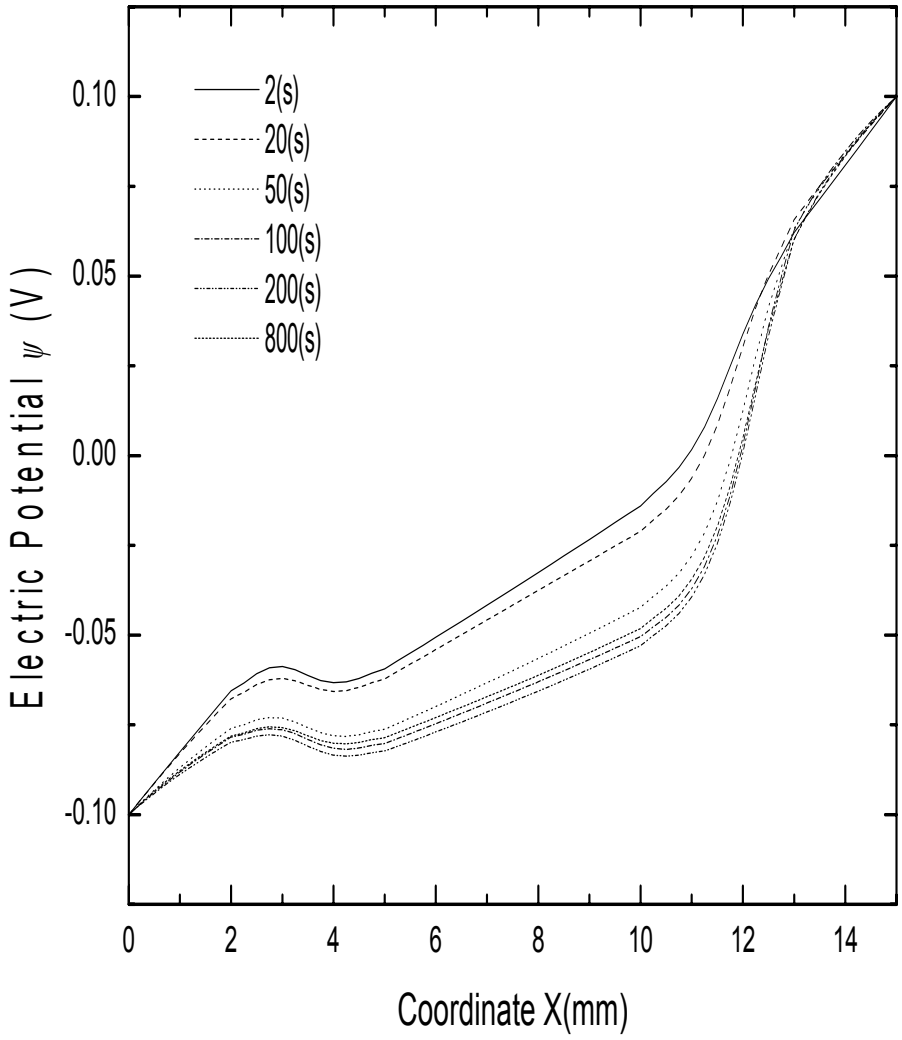

Figure 5.19 Variation of electric potential with time for V_e = 0.2(V), c_0^f = 4(mol/m^3) and c^* = 1(mol/m^3).

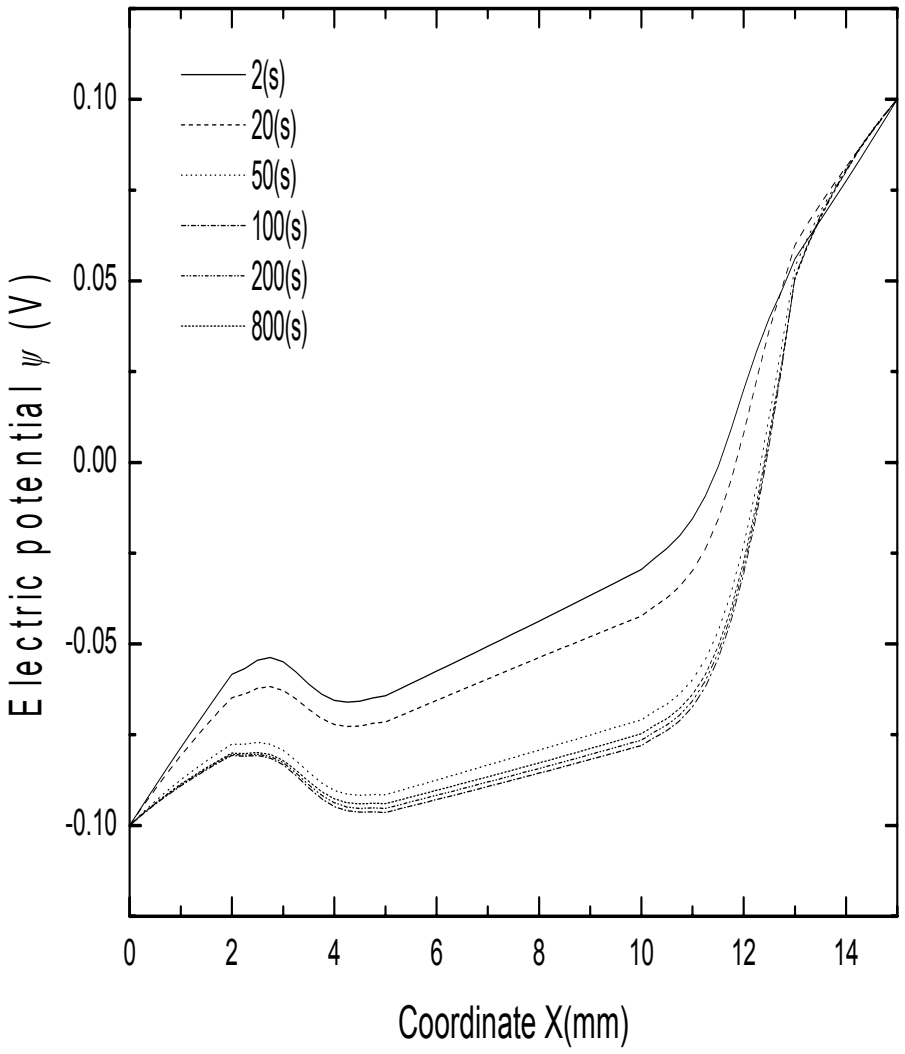

Figure 5.20 Variation of electric potential with time for V_e = 0.2(V), c_0^f = 8(mol/m^3) and c^* = 1(mol/m^3).

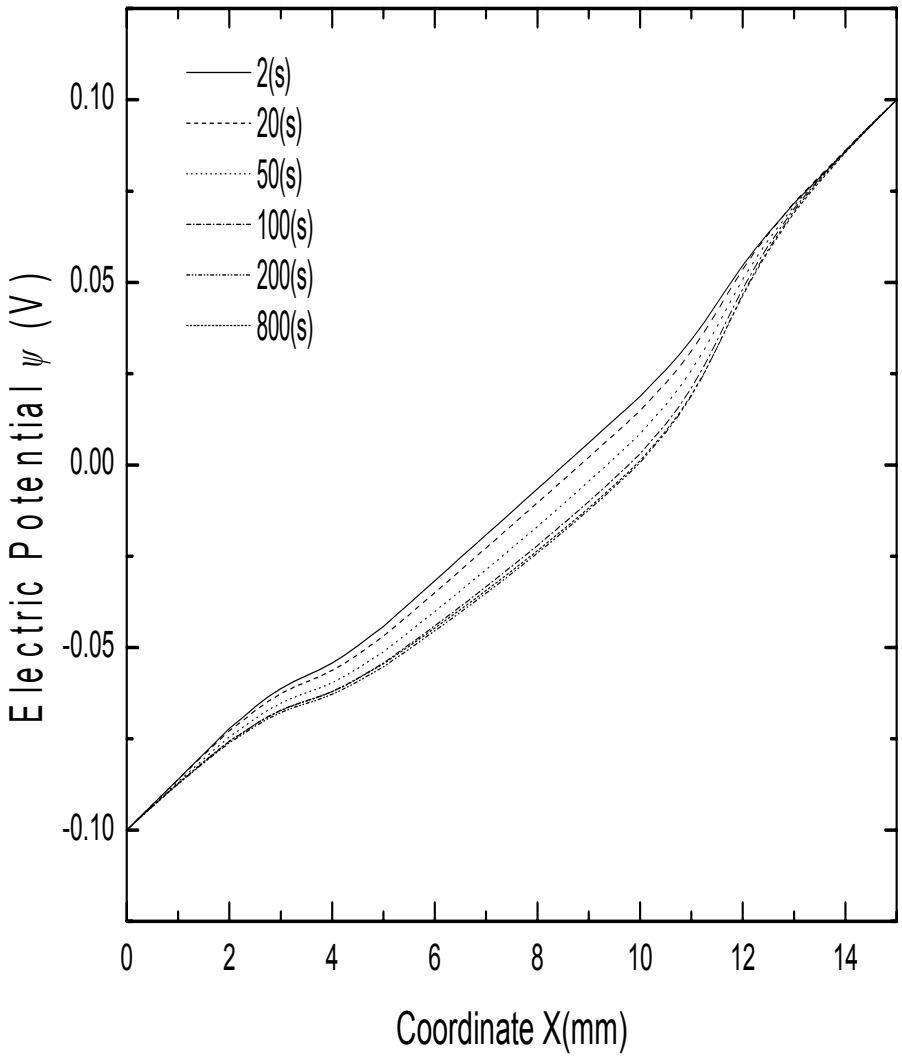

Figure 5.21 Variation of electric potential with time for V_e = 0.2(V), c_0^f = 2(mol/m^3) and c^* = 2(mol/m^3).

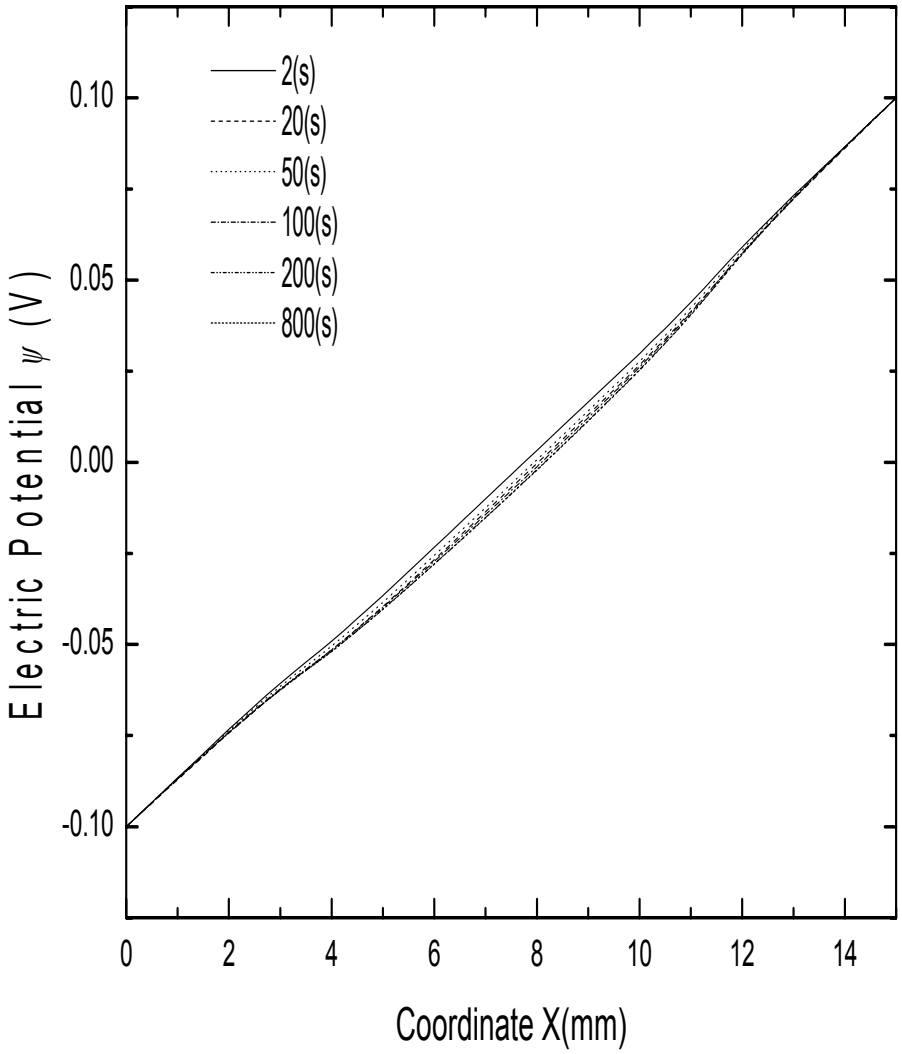

Figure 5.22 Variation of electric potential with time for V_e = 0.2(V), c_0^f = 2(mol/m^3) and c^* = 8(mol/m^3).

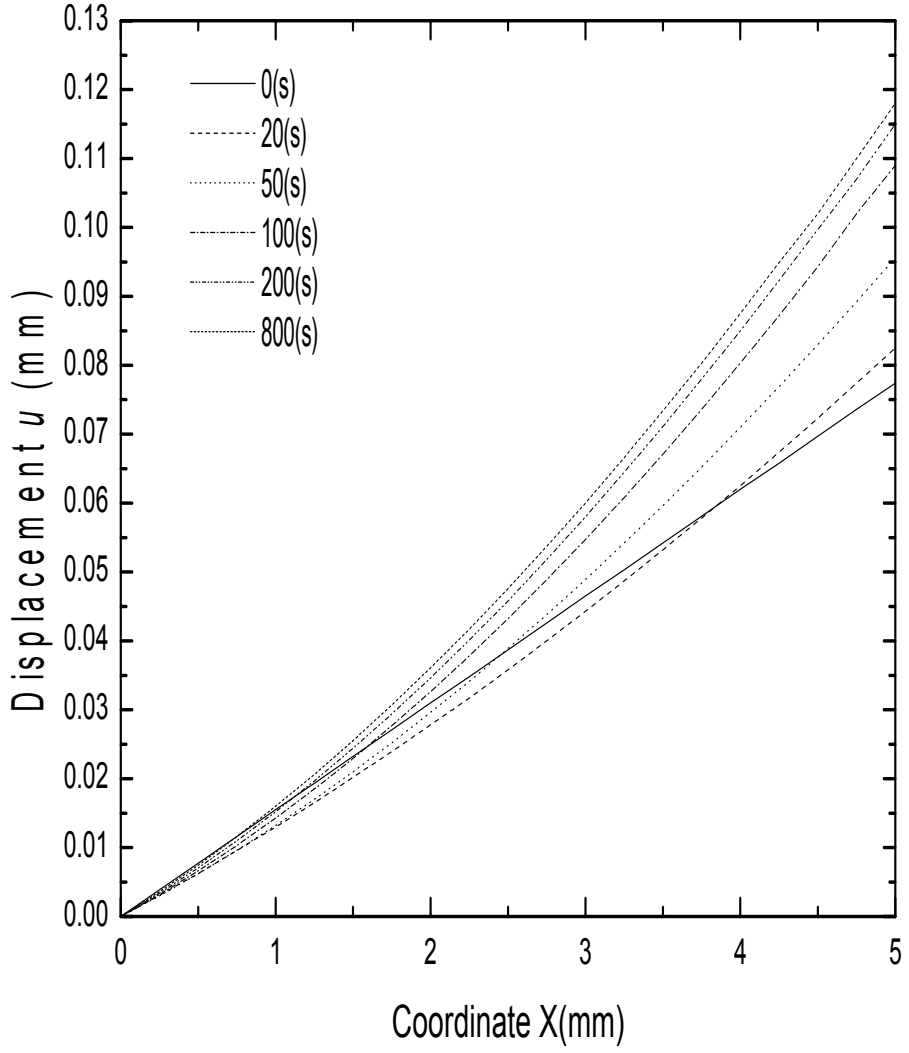

Figure 5.23 Variation of hydrogel displacement with time for V_e = 0.2(V), c_0^f = 2(mol/m^3) and c^* = 1(mol/m^3).

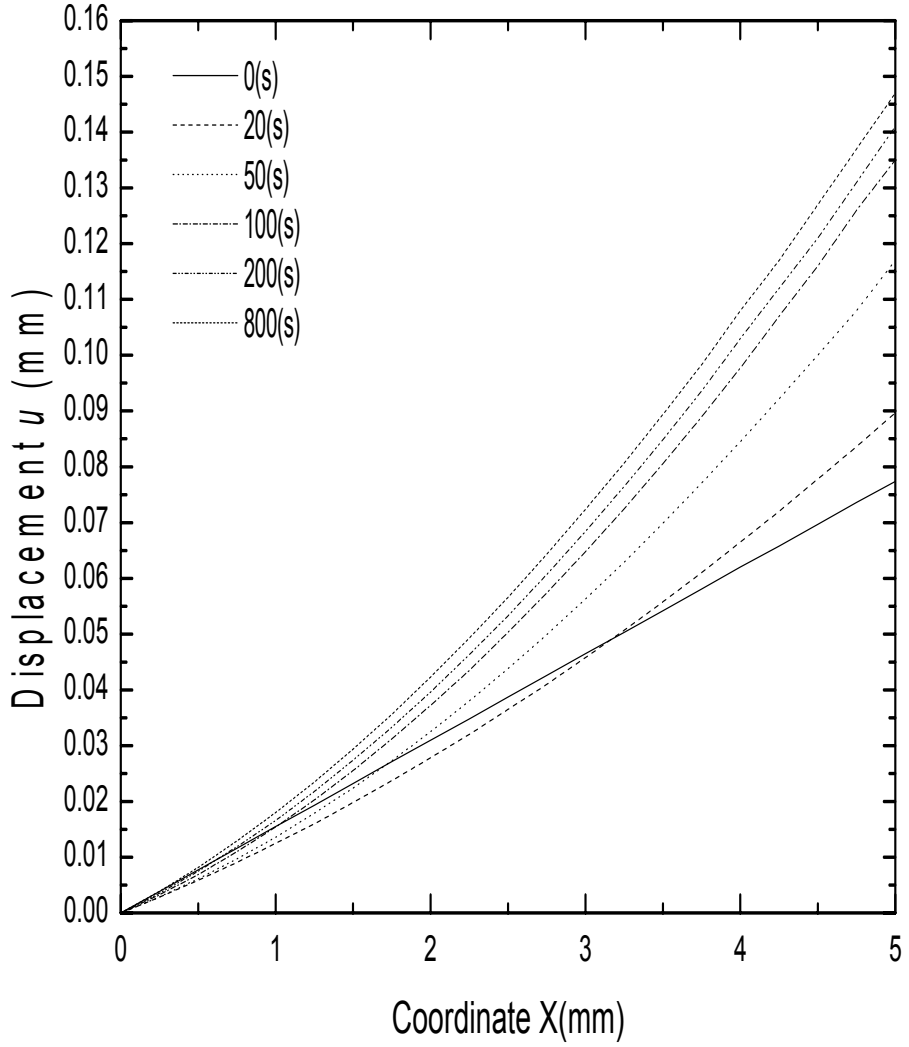

Figure 5.24 Variation of hydrogel displacement with time for $V_e = 0.3$(V), $c_0^f =$ 2(mol/m^3) and $c^* = 1$(mol/m^3).

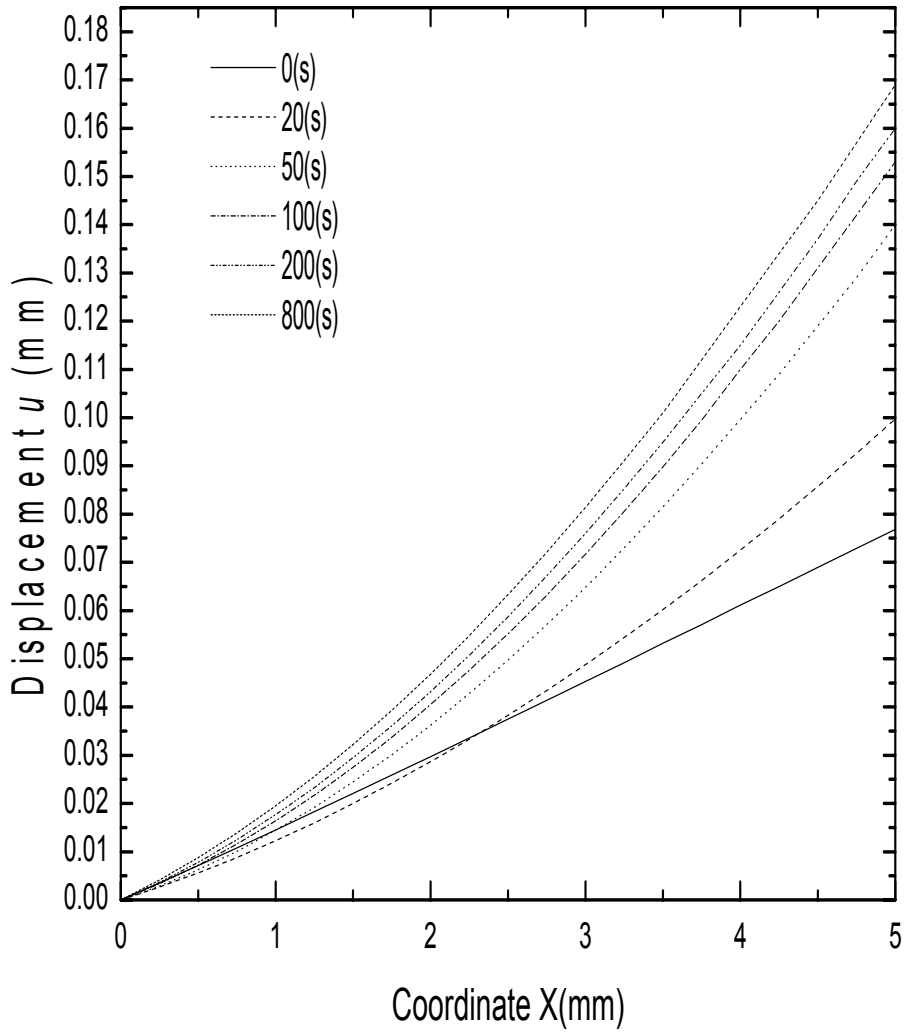

Figure 5.25 Variation of hydrogel displacement with time for $V_e = 0.4$(V), $c_0^f =$ 2(mol/m^3) and $c^* = 1$(mol/m^3).

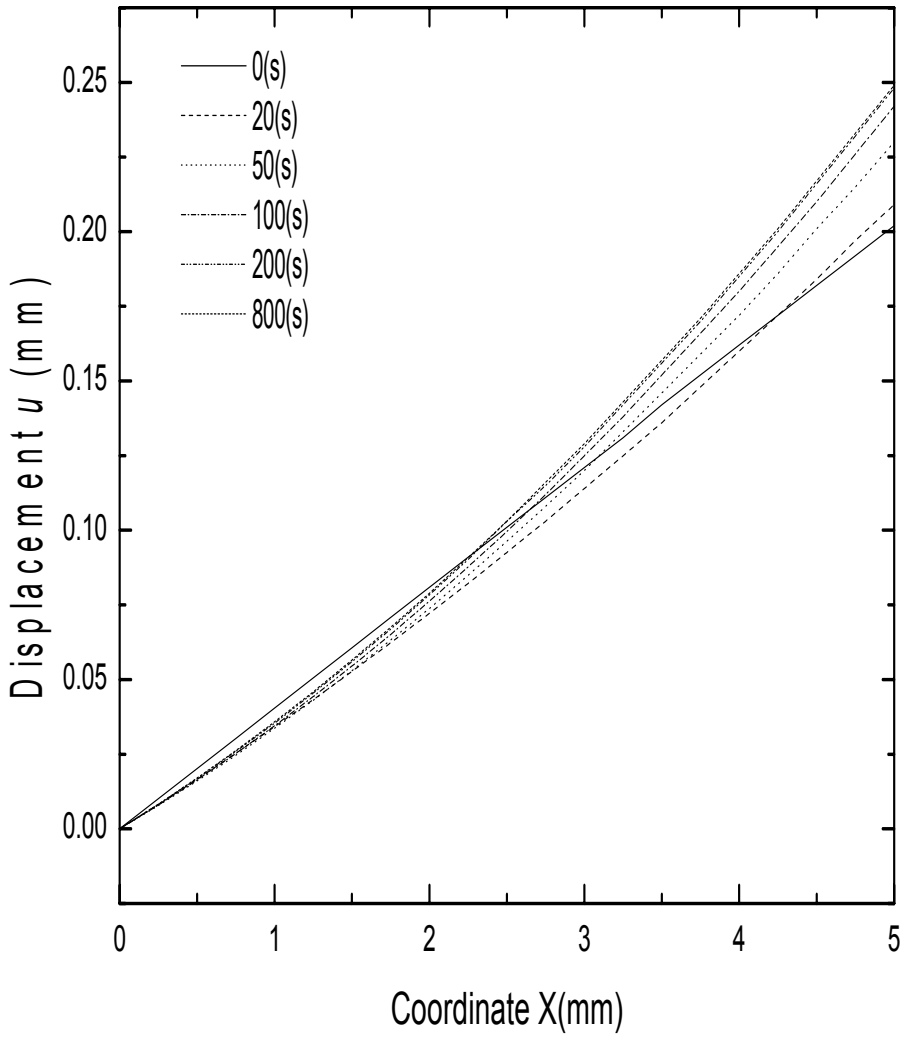

Figure 5.26 Variation of hydrogel displacement with time for V_e = 0.2(V), c_0^f = 4(mol/m^3) and c^* = 1(mol/m^3).

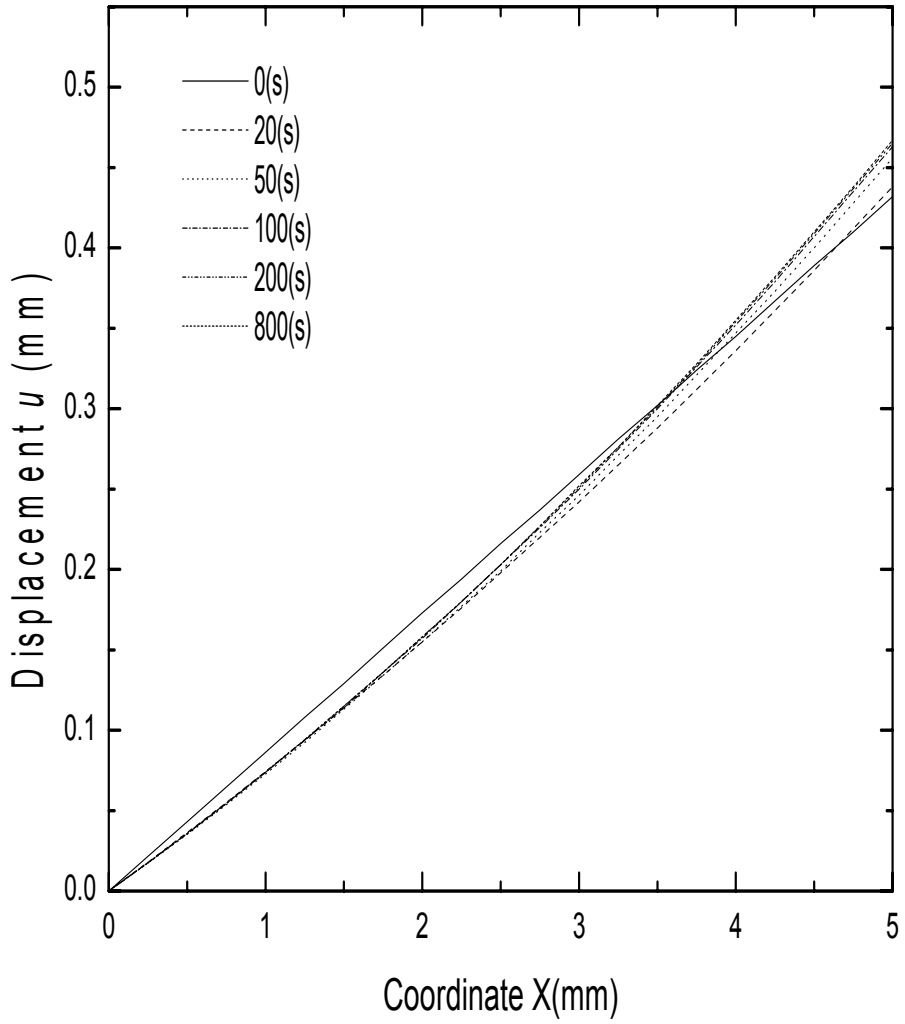

Figure 5.27 Variation of hydrogel displacement with time for $V_e = 0.2$(V), $c_0^f =$ 8(mol/m^3) and $c^* = 1$(mol/m^3).

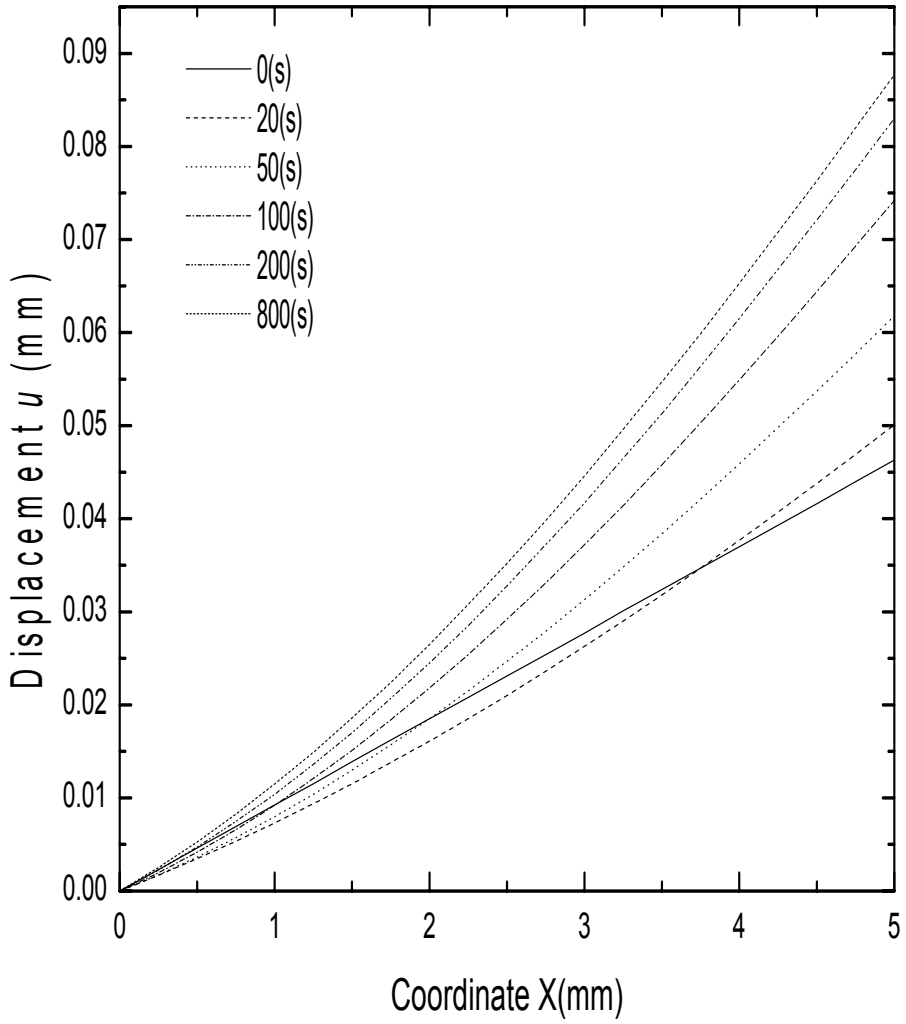

Figure 5.28 Variation of hydrogel displacement with time for V_e = 0.2(V), c_0^f = 2(mol/m^3) and c^* = 2(mol/m^3).

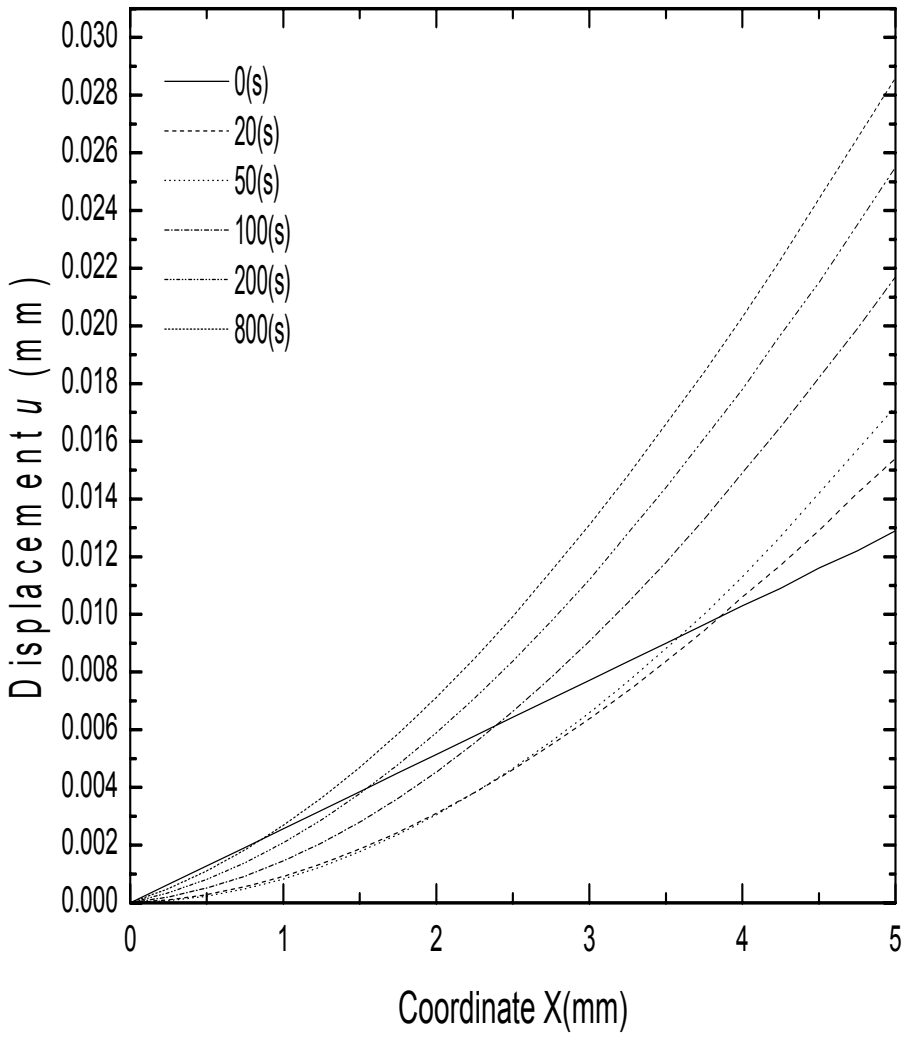

Figure 5.29 Variation of hydrogel displacement with time for V_e = 0.2(V), c_0^f = 2(mol/m^3) and c^* = 8(mol/m^3).

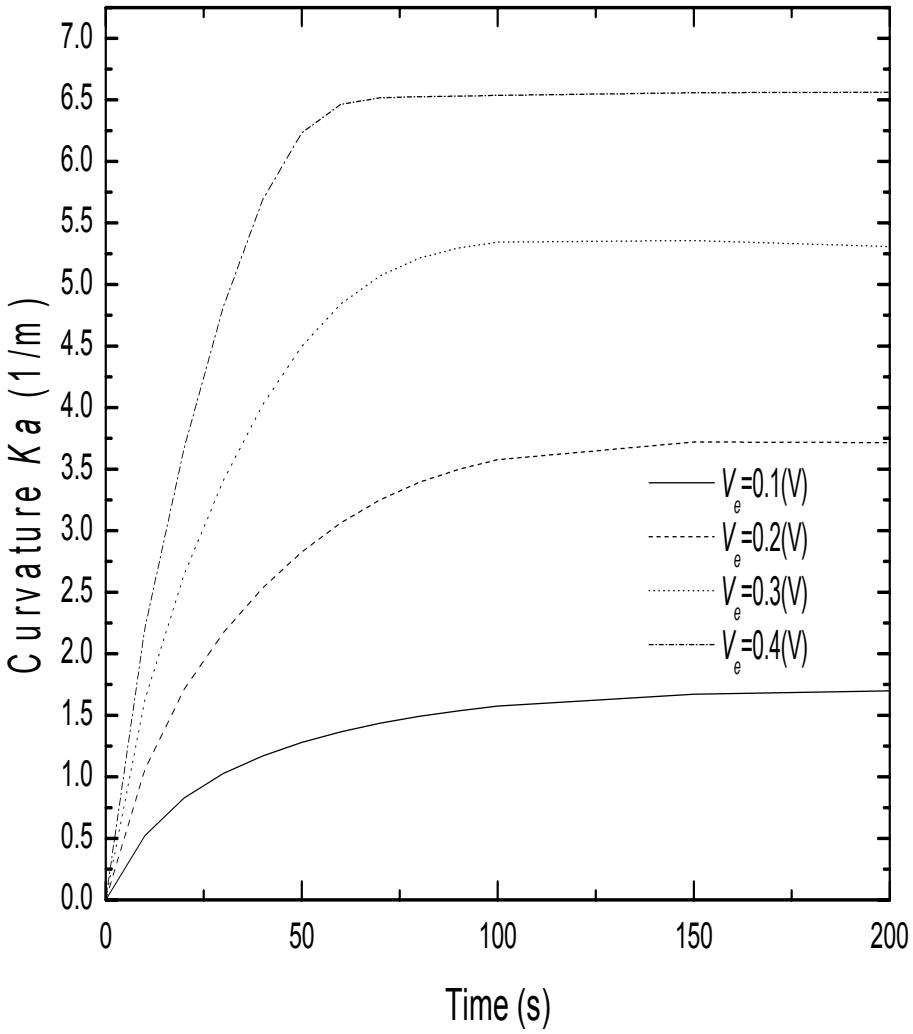

Figure 5.30 Effect of externally applied electric field V_e on the variation of average curvature *Ka* distributions with time.

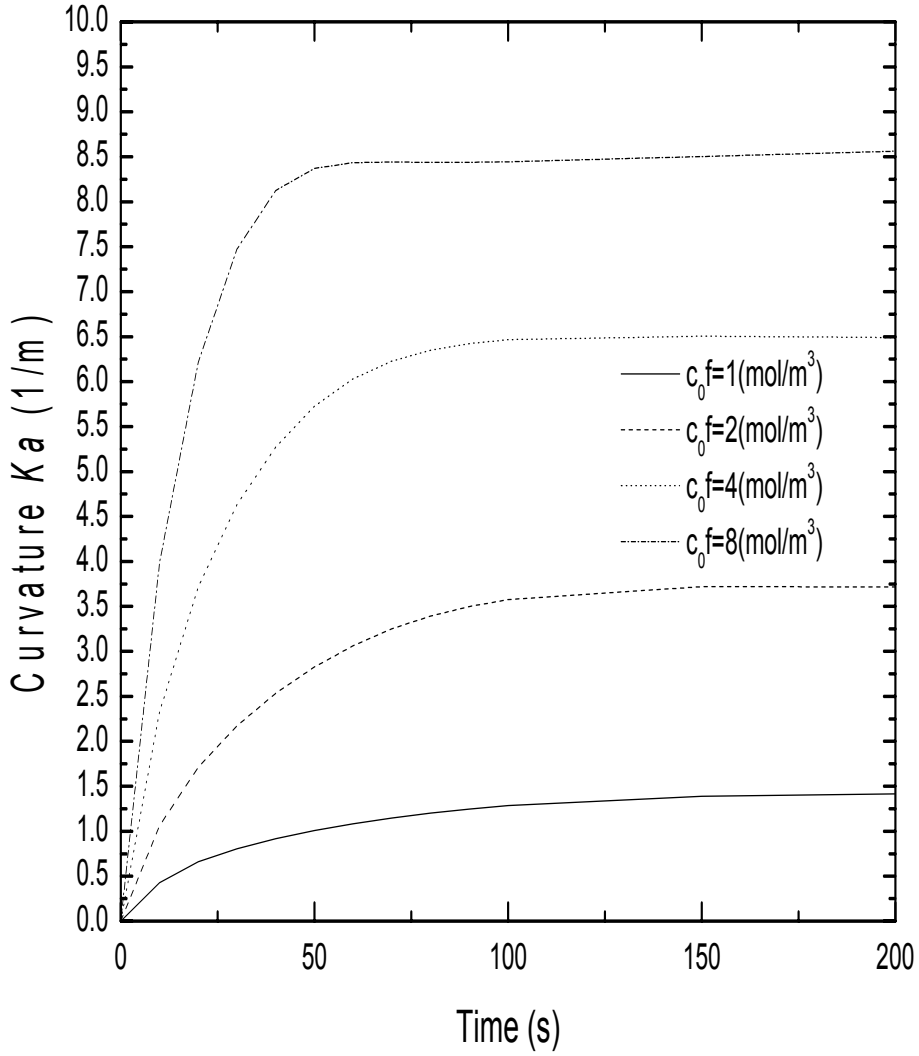

Figure 5.31 Effect of fixed-charged density c_0^f on the variation of average curvature *Ka* distributions with time.

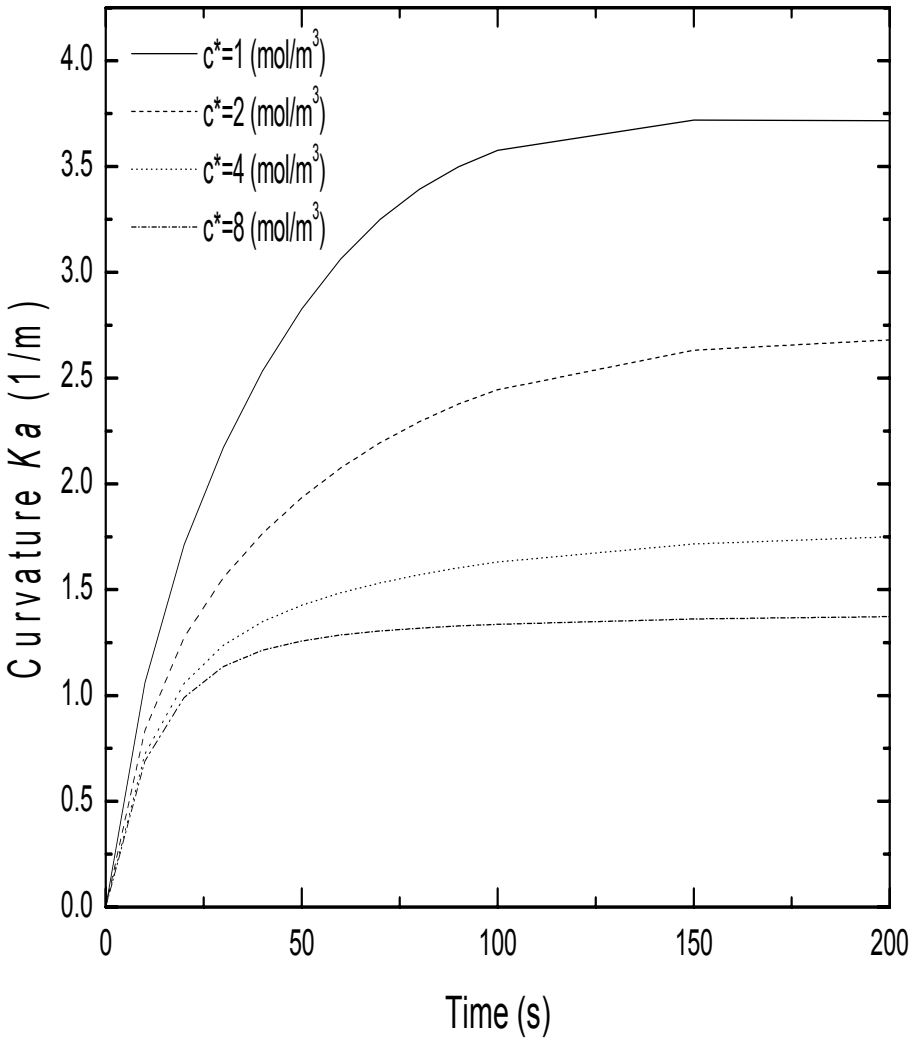

Figure 5.32 Effect of bath solution concentration c^* on the variation of average curvature *Ka* distributions with time.

Chapter 6

Conclusions and Future Works

Based on the previous studies and discussions, a few important conclusions are drawn in this chapter. This is followed by recommendation of several future works.

6.1 Conclusions

This dissertation focuses on the study of the responsive behaviors of electric-sensitive hydrogels immersed a bath solution under an externally applied electric field. A novel mathematical model, termed Multi-Effect-Coupling Electric-Stimulus (MECe) model, has been developed with considerations of chemo-electro-mechanical coupling effects. For numerical solution of the MECe model consisting of nonlinear partial differential governing equations, a newly developed meshless technique, called the Hermite-Cloud method, has been employed in the present computations and validated to improve computational accuracy of both unknown functions and corresponding first-order derivatives. After examination of MECe model through comparison with experimental data extracted from open literature, the numerical simulations are carried out for the swelling equilibrium and kinetics of electric-stimulus responsive hydrogels. Discussions are also made in detail for influence of several important physical

parameters on ionic diffusion, electric potential and hydrogel deformation.

As the key external stimulus to the electric-sensitive hydrogels, the externally applied electric field is found to play a critical role in the responses of hydrogels. Due to the drag force of electric field, the mobile ions in the bath solution diffuse into the hydrogels and thus produce an ionic concentration difference near the hydrogel-solution interfaces, which makes the hydrogel deform. When the applied voltage is fixed, the ionic concentration difference increases with time, and the hydrogel mixture finally reaches the equilibrium state after a sometime called critical time. It is also concluded that, as the applied voltage increases, the critical time decreases and the deformation of hydrogels becomes larger. This reveals a significant influence of externally applied electric field on the responsive behaviors of hydrogels.

The fixed-charge attached onto the chains of the polymeric matrix of hydrogels is another key parameter. The fixed-charge groups with negative valence will attract the mobile cations into the hydrogel mixture from the bath solution, resulting in a fluid pressure and inducing the hydrogel to deform. With the increase of fixed-charge density, the concentration of cations within the hydrogels has a dramatic variation while that of anions only changes slightly. The critical time of the kinetic response of hydrogels decreases with increasing fixed-charge density since the attracting effect of the fixed-charge on mobile ions is strengthened.

In addition, one should pay attention to the characteristics of the surrounding

bath solutions, including the concentration and composition of ionic species in the bath solutions. The effect of bath solution concentrations is chiefly revealed by the counteractive function to the fixed-charge density. With the increment of bath solution concentrations, the attracting effect of the fixed-charge groups on the diffusive mobile ions becomes more insignificant and the conductivity of bath solutions in the whole computational domain remains almost identical. This results in a quasi-linear distribution of the electric potential and a decrease in the critical time of the kinetic response of hydrogels. On the other hand, the valence of bath ions can also affect the hydrogel deformation. A bath solution with higher ionic valence will cause a larger difference of ion concentrations and larger displacement of the hydrogels.

Finally, it should be noted that, in general, the response time of the electric-sensitive hydrogels to the externally applied electric-field trigger is always very short, normally shorter than 4 minutes in the present simulations. The simulated results agree well with the experimental findings and validate the great promise of the electric-sensitive hydrogels in further applications of biotechnology and bioengineering.

6.2 Future Works

As mentioned previously, the numerical studies and discussions in this dissertation are based on the one-dimensional simulations. However the 3-D hydrogel strip actually deforms in all three directions. Therefore, in order to obtain

more accurate simulations and deeper understanding of the responsive behaviors of electric-sensitive hydrogels, it is necessary for the future work to make the two-dimensional or three-dimensional analyses.

In addition, due to the variety and complexity of environmental stimuli, the studies in this dissertation are limited only in the stimulus of externally applied electric field, excluding other stimuli, such as the solution pH, temperature and chemical reactions etc., which actually are important triggers for the responsive behaviors of bio-stimuli polymeric hydrogels. Therefore, incorporation of these environmental stimuli is recommended for the future work.

References

Aluru, N.R. and G. Li. Finite cloud method: a true meshless technique based on a fixed reproducing kernel approximation, International Journal for Numerical Methods in Engineering, *50*, pp. 2373-2410. 2001.

Beebe, D.J., Moore, J., Bauer, J.M., Yu, Q., Liu, R.H., Devadoss, C. and B-H. Jo. Functional structures for autonomous flow control inside micro-fluidic channels, Nature, *404*, pp. 588-590. 2000.

Belytschko, T., Lu, Y.Y. and L. Gu. Element free Galerkin methods, International Journal for Numerical Methods in Engineering, *37*, pp. 229-256. 1994.

Chen, G. and A.S. Hoffman. Graft copolymers that exhibit temperature-induced phase transitions over a wide range of pH, Nature, *373*, pp. 49-52. 1995.

Chu, Y., Varanasi, P.P., McGlade, M.J. and S. Varanasi. Ph-induced swelling kinetics of polyelectrolyte hydrogels, Journal of Applied Polymer Science, *58*, pp. 2161-2176. 1995.

Doi, M., Matsumoto, M. and Y. Hirose. Deformation of ionic polymer gels by electric fields, Macromolecules, *25*, pp. 5504-5511. 1992.

Eisenberg, S.R. and A.J. Grodzinsky. The kinetics of chemically induced nonequilibrium swelling of articular cartilage and corneal stroma, ASME Journal of Biomechanical Engineering, *109*, pp. 79-89. 1987.

Fei, J.Q., Zhang, Z.P. and L.X. Gu. Bending behavior of electroresponsive poly(vinyl alcohol) /poly(acrylic acid) semi-interpenetrating network hydrogel fibers under an electric stimulus, Polymer International, *51*, pp. 502-509. 2002.

Galaev, I.Y. and B. Mattiasson. ‘Smart’ polymers and what they could do in biotechnology and medicine, Trend in Biotechnology, *17*, pp, 335-340. 1999.

Grimshaw, P.E., Nussbaum, J.H. Grodzinsky, A.J. and M.L. Yarmush. Kinetics of electrically and chemically induced swelling in polyelectrolyte gels, Journal of Chemical Physics, *93*, pp. 4462-4472. 1990.

Gu, W.Y., Lai, W.M. and V.C. Mow. A mixture theory for charged-hydrated soft tissues containing multi-electrolytes: passive transport and swelling behaviors, Journal of Biomechanical Engineering, *120*, pp. 169-181. 1998.

Gu, W.Y., Lai, W.M. and V.C. Mow. Transport of multi-electrolytes in charged

hydrated biological soft tissues, Transport in Porous Media, *34*, pp. 143-157. 1999.

Homma, M., Seida, Y. and Y. Nakano. Evaluation of optimum condition for designing high performance electro-driven polymer hydrogel systems, Journal of Applied Polymer Science, *75*, pp. 111-118. 2000.

Homma, M., Seida, Y. and Y. Nakano. Effect of ions on the dynamic behavior of an electrodriven ionic polymer hydrogel membrane, Journal of Applied Polymer Science, *82*, pp. 76-80. 2001.

Hon, Y.C., Lu, M.W., Xue, W.M. and X. Zhou. A new formulation and computation of the triphasic model for mechano-electrochemical mixtures, Computational Mechanics, *24*(*3*), pp. 155-165. 1999.

Jeong, B. and A. Gutowska. Lessons from nature: stimuli-responsive polymers and their biomedical applications, Trends in Biotechnology, *20*(*7*), pp. 305-311. 2002.

Kataoka, K., Miyazaki, H., Bunya, M., Okano, T. and Y. Sakurai. Totally synthetic polymer gels responding to external glucose concentration: their preparation and application to on-off regulation of insulin release, Journal of American Chemical Society, *120*, pp. 12694-12695. 1998.

Kim, S.Y. and H.S. Shin. Properties of electroresponsive poly(vinglalcohol)/poly(acrylic acid) IPN hydrogels under an electric stimulus, Journal of Applied Polymer Science, *73*, pp. 1675–1683. 1999.

Kokufuta, E., Zhang, Y.Q. and T. Tanaka. Saccharide-sensitive phase transition of a lectin-loaded gel, Nature, *351*, pp. 302-304. 1991.

Kwon, I.C., Bae, Y.H. and S.W. Kim. Electrically erodible polymer gel for controlled release of drugs, Nature, *354*, pp. 291-293. 1991.

Lai, W.M., Hou, J.S. and V.C. Mow. A triphasic theory for the swelling and deformation behaviors of articular cartilage, ASME Journal of Biomechanical Engineering, *113*, pp. 245-258. 1991.

Lam, K.Y., Wang, Q.X. and Z. Zong. A nonlinear fluid-structure interaction analysis of a near-bed submarine pipeline in a current, Journal of Fluids and Structures, *16*, pp. 1177-1191. 2002.

Lanir, Y. Biorheology and fluid flux in swelling tissues. I. biocomponent theory for small deformations, including concentration effects, Biorheology, *23*, pp.

173-188. 1987.

Li, H., Chen, J. and K.Y. Lam. Multiphysic modeling and meshless simulation of electric-sensitive hydrogels, Journal of Polymer Science Part B: Polymer Physics, *42*, pp. 1514-1531. 2004.

Li, H., Cheng, J.Q., Ng, T.Y., Chen, J. and K.Y. Lam. A meshless Hermite-Cloud method for nonlinear fluid structure analysis of near-bed submarine pipelines under current, Engineering Structures, *26*, pp. 531-542. 2004.

Li, H., Ng, T. Y., Cheng, J. Q. and Lam, K.Y. Hermite-Cloud: a novel true meshless method, Computational Mechanics, *33*, pp. 30-41. 2003.

Li, H., Yuan, Z., Lam, K.Y., Lee, H.P., Chen, J., Hanes, J. and J. Fu. Model development and numerical simulation of electric-stimulus-responsive hydrogels subject to an externally applied electric field, Biosensors and Bioelectronics, *19*, pp. 1097-1107. 2004.

Liu, G.R. Mesh Free Methods: Moving beyond the Finite Element Method. pp. 9-27, Florida: CRC Press. 2003.

Liu, G.R. and Y.T. Gu. A point interpolation method for two-dimenional solids, International Journal for Numerical Methods in Engineering, *50*, pp. 937-951. 2001.

Liu, G.R. and Y.T. Gu. A local radial point interpolation method for stress analysis of two-dimensional solids, Structural Engineering and Mechanics, *11*(*2*), pp. 221-236. 2001.

Liu, G.R., Wu, Y.L. and Y.T. Gu. Application of meshless local Petrov-Galerkin (MLPG) approach to fluid flow problem. In Proc. First Asian-Pacific Congress on Computational Mechanics, November 2001, Sydney, Australia, pp. 20-23.

Liu, W.K., Chen, Y., Jun. S., Chen, J.S., Belytschko, T., Pan, C., Uras, R.A. and C.T. Chang. Overview and applications of the reproducing kernel particle methods, Archives of Computational Methods in Engineering: State of the Art Reviews, *3*, pp. 3-80. 1996.

Liu, W.K., Jun, S., Li, S., Adde, J. and T. Belytschko. Reproducing kernel particle methods for structural dynamics, International Journal for Numerical Methods in Fluids, *38*, pp. 1665-1679. 1995.

Liu, W.K., Jun, S. and Y.F. Zhang. Reproducing kernel particle methods, International Journal for Numerical Methods in Engineering, *20*, pp. 1081-1106.

1995.

Lucy, L. A numerical approach to testing the fission hypothesis, Astronomical Journal, *82*, pp. 1013-1024. 1977.

Mow, V.C., Kuei, S.C., Lai, W.M. and C.G. Armstrong. Biphasic creep and stress relaxation of articular cartilage in compression: theory and experiments, ASME Journal of Biomechanical Engineering, *102*, pp. 73-84. 1980.

Myers, E.R., Lai, W.M. and V.C. Mow. A continuum theory and an experiment for the ion-induced swelling behavior of articular cartilage, ASME Journal of Biomechanical Engineering, *106*, pp. 151-158. 1984.

Nayroles, B., Touzot, G. and P. Villon. Generalizing the finite element method: diffuse approximation and diffuse elements, Computational Mechanics, *10*, pp. 307-318. 1992.

Ng, T.Y., Li, H., Cheng, J.Q. and K.Y. Lam. A new hybrid meshless-differential order reduction (*h*M-DOR) method with applications to shape control of smart structures via distributed sensors/actuators, Engineering Structures, *25*, pp. 141-154. 2003.

Onate, E., Idelsohn, S., Zienkiewicz, O.C. and R.L. Taylor. A finite point method in computational mechanics. Applications to convective transport and fluid flow, International Journal for Numerical Methods in Engineering, *39*, pp. 3839-3866. 1996.

Osada, Y., Okuzaki, H. and H. Hori. A polymer gel with electrically driven motility, Nature, *355*, pp. 242-244. 1992.

Reddy, J.N. An introduction to the finite element method. pp. 177-187, New York: McGraw-Hill. 1993.

Shahiinpoor, M. Continuum electromechanics of ionic polymer gels as artificial muscles for robotic applications, Smart Materials and Structures, *3*, pp. 367-372. 1994.

Shahinpoor, M. Micro-electro-mechanics of ionic polymer gels as electrically controlled artificially muscles, Journal of Intelligent Material and Systems Structures, *6*, pp. 307-314. 1995.

Shiga, T and T. Karauchi. Deformation of polyelectrolyte gels under the influence of electric field, Journal of Applied Polymer Science, *39*, pp. 2305-2320. 1990.

Siegel, R.A. pH sensitive gels: swelling equilibria, kinetics and application for drug delivery. Pulsed and Self-Regulated Drug Delivery, pp. 129-155. Florida: CRC Press. 1990.

Siegel, R.A. and B.A. Firestone. pH-dependent equilibrium swelling properties of hydrophobic polyelectrolyte copolymer gels, Macromolecules, *21*, pp. 3254-3259. 1988.

Sun, S and A.F.T. Mak. The dynamical response of a hydrogel fiber to electrochemical stimulation, Journal of Polymer Science part B: Polymer Physics, *39*, pp. 236-246. 2001.

Tanaka, T. Collapse of gels and the critical endpoint, Physical Review Letters, *40*, pp. 820-823. 1978.

Tanaka, T., Fillmore, D., Sun, S-T., Nishio, I., Swislow, G. and A. Shah. Phase transitions in ionic gels, Physical Review Letters, *45*, pp. 1636-1639. 1980.

Tanaka, T., Nishio, I., Sun, S.T. and S. Ueno-Nishio. Collapse of gels in an electric field, Science, *218*, pp. 467-469. 1982.

Wallmersperger, T. and B. Kroeplin. Modeling and analysis of the chemistry and electromechanics. Electroactive Polymer Actuators as Artificial Muscles, ed by B-C. Yoseph, pp. 285-307. Washington: SPIE Press. 2001.

Wallmersperger, T., Kroplin, B., Holdenried, J. and R.W. Gulch. A coupled multi-field formulation for ionic gels in electric fields. In Proc. SPIE 8th Annual International Symposium on Smart Structure and Materials, March 2001, Newport Beach, CA, USA, *4329*, pp. 264-275. 2001.

Yoshida, R., Uchida, K., Kaneko, Y., Sakai, K., Kikuchi, A., Sakurai, Y. and T. Okano. Comb-type grafted hydrogels with rapid de-swelling response to temperature changes, Nature, *374*, pp. 240-242. 1995.

Zhou, X., Hon, Y.C., Sun, S. and A.F.T. Mak. Numerical simulation of the steady-state deformation of a smart hydrogel under an external electric field, Smart Materials and Structures, *11*, 459-467. 2002.

Publications Arising From Thesis

Li, H., Chen, J. and K.Y. Lam. Multiphysic modeling and meshless simulation of electric-sensitive hydrogels, Journal of Polymer Science Part B: Polymer Physics, *42*, pp. 1514-1531. 2004.

Li, H., Cheng, J.Q., Ng, T.Y., Chen, J. and K.Y. Lam. A meshless Hermite-Cloud method for nonlinear fluid structure analysis of near-bed submarine pipelines under current, Engineering Structures, *26*, pp. 531-542. 2004.

Li, H., Yuan, Z., Lam, K.Y., Lee, H.P., Chen, J., Hanes, J. and J. Fu. Model development and numerical simulation of electric-stimulus-responsive hydrogels subject to an externally applied electric field, Biosensors and Bioelectronics, *19*, pp. 1097-1107. 2004.

Chen, J., Li, H. and K.Y. Lam. Transient Simulation for Kinetic Responsive Behaviors of Electric-sensitive Hydrogels. In Proc. 2004 Europe Material Research Society Spring Meeting, 24-28 May 2004, Strasbourg, France.

Yuan, Z., Li, H., Ng, T.Y. and J. Chen. A Coupled Multi-Field Formulation for Stimuli-Responsive Hydrogel Subject to Electric Field. In Proc. International Conference on Scientific and Engineering Computation (IC-SEC 2002) 3-5 December 2002, Singapore, pp. 884-887.